



universität
wien

MASTERARBEIT

Titel der Masterarbeit

"Devitrification Of Co_3Ti
Studied By Electron Microscopy Methods"

verfasst von

Christian Ebner BSc

angestrebter akademischer Grad

Master Of Science (MSc)

Wien, 2014

Studienkennzahl lt. Studienblatt: A 066 876

Studienrichtung lt. Studienblatt: Masterstudium Physik

Betreuer: Ao. Univ.-Prof. Mag. Dr. Christian Rentenberger

Abstract

In this work amorphous Co_3Ti is produced from an initially polycrystalline L_{12} structured alloy. The alloy is molten using Cobalt and Titanium of high purity (99.995 % each) in an induction furnace, casted in a crystal growth furnace and annealed for ~ 100 h at 950°C . The homogenized Co_3Ti phase is rendered amorphous, performing a solid state transition by severe plastic deformation using the method of high pressure torsion (HPT). After deformation, the amorphous specimens are investigated by different electron microscopy methods and by nanoindentation. The thermal stability of the amorphous state is analyzed by in-situ heating in a transmission electron microscope (TEM) and ex-situ by differential scanning calorimetry (DSC). During the in-situ experiment the devitrification is studied by heating the specimen stepwise inside a heating holder, using bright-field, dark-field and diffraction imaging. The formation of small sized nanocrystals (5 nm to 50 nm) is observed, forming in a preferred way in thin specimen regions, where the surface to volume ratio is very high. The starting temperature of devitrification is around 400°C to 430°C , depending strongly on the local specimen thickness. The nanocrystals formed in-situ show mostly the Co-hcp structure, as deduced from the analysis of diffraction patterns. In addition to the Co-hcp nanocrystals, scanning transmission electron microscopy (STEM) revealed a high density of nanometer sized TiO_2 particles grown at the surface. This process changes the composition of the remaining matrix to a higher Co content and leads finally to the formation of Co-rich crystallites with the high temperature fcc structure, according to the phase diagram. By cooling the specimen after devitrification a polymorphic phase transformation occurs from the Co-fcc high-temperature phase to the Co-hcp low temperature phase as observed by electron diffraction. Due to the small size of the crystals, still fcc structured ones containing a high density of stacking faults are observed by high resolution TEM. In ex-situ experiments performed on bulk samples in the DSC the formation of fcc Co_3Ti crystallites is deduced by electron diffraction and atomic resolution STEM. The fcc crystals form out of the amorphous phase by a strong anisotropy growth, that results in a plate like form of the crystallites. The crystal orientation of different grains is randomly distributed, indicating that there is no influence on growth via the matrix between these grains. The ex-situ DSC measurements show a higher phase transition temperature ($\sim 460^\circ\text{C}$) as compared to the in-situ observations due to the reduced surface effects. The nanoindentation experiments revealed a difference in hardness and Young's modulus, depending on the thermal treatment after the HPT processing. The amorphous specimen shows the lowest E-modulus with (131.1 ± 3.8) GPa, whereas in the fully recrystallized material it recovers to (182.39 ± 3.98) GPa. The hardness increases from (6.48 ± 0.15) GPa for the amorphous state up to (7.68 ± 0.12) GPa by the thermal treatment.

Zusammenfassung

In dieser Arbeit wurde amorphes Co_3Ti aus einer ursprünglich polykristallinen, L1_2 geordneten Legierung erzeugt. Die Legierung wurde aus hochreinen Elementen (jeweils 99.995 %) in einem Induktionsofen eingeschmolzen, in einem Kristallzuchtoven in Form gegossen und schließlich für ~ 100 h bei 950°C ausgeheilt. Die so erhaltene homogene Co_3Ti Phase wurde amorphisiert, indem eine Phasenumwandlung im Festkörper durch Hochverformung mit Hilfe der Methode der Hochdrucktorsion erzielt wurde. Nach der Verformung wurden die amorphisierten Proben mit verschiedenen elektronenmikroskopischen Methoden und mit Nanoeindrucksmessungen untersucht. Die thermische Stabilität des amorphen Zustandes wurde durch in-situ Heizen im Transmissionselektronenmikroskop (TEM) sowie ex-situ mittels Differenzkalorimetrie (DSC) untersucht. Während des in-situ Experimentes wurde die Entglasung der Legierung durch Heizen in einem Heizhalter mittels Hellfeld- und Dunkelfeldaufnahmen, sowie mittels Beugungsbildern beobachtet. Die Entstehung von kleinen Nanokristallen (in der Größenordnung 5-50 nm) wurde beobachtet, wobei die Kristalle in Regionen mit großem Oberflächen zu Volumenverhältnis in bevorzugter Weise entstehen. Die Starttemperatur der Entglasung liegt bei etwa $400\text{--}430^\circ\text{C}$, in Abhängigkeit von der lokalen Probendicke. Die in-situ entstandenen Nanokristalle besitzen eine Co-hexagonal dichtestgepackte (hdp) Struktur wie aus der Auswertung von Beugungsbildern hervorgeht. Zusätzlich zu den Co-reichen Nanokristallen zeigt das Rastertransmissionselektronenmikroskop (STEM) auch eine hohe Dichte von Nanometer großen TiO_2 Teilchen, welche auf der Oberfläche aufgewachsen sind. Die Oxidation bewirkt eine Konzentrationsänderung der Matrix in Richtung eines höheren Co-Gehalts und bewirkt schließlich die Entstehung von Co-reichen Kristallen mit der Hochtemperaturphase (kubisch flächenzentriert, kfz), in Übereinstimmung mit dem Phasendiagramm. Durch Abkühlen der Probe nach erfolgter Entglasung wird eine polymorphe Phasentransformation von der Hochtemperatur Co-kfz zur Niedertemperatur Co-hdp Phase ausgelöst, was mittels Elektronenbeugung beobachtet wurde. Aufgrund der kleinen Größe der Kristallite wurden viele kfz-strukturierte Teilchen mit einer hohen Stapelfehlerdichte in Hochauflösungsbildern beobachtet. Die ex-situ Experimente, welche an massiven Proben mittels DSC durchgeführt wurden, zeigten die Entstehung von kfz Co_3Ti Kristallen. Dies wurde durch Elektronenbeugung und atomar aufgelöster STEM-Aufnahmen festgestellt. Die Kristalle zeigen ein stark anisotropes Wachstum was sich in einer Plattenform der Kristallite manifestiert. Die Orientierung verschiedener Körner ist statistisch verteilt, was darauf hindeutet dass es keinen Einfluss der einzelnen Körner auf deren Wachstum über die Matrix hinweg gibt. Die ex-situ DSC Messungen ergaben eine im Vergleich zu den in-situ Beobachtungen höhere Phasenübergangstemperatur ($\sim 460^\circ\text{C}$), aufgrund der reduzierten Oberflächeneffekte. Die Nanoeindrucksmessungen ergaben einen Unterschied in Härte und Elastizitätsmodul in Abhängigkeit von der thermischen Behandlung nach der Verformung. Der E-Modul der amorphen Probe ergab den niedrigsten Wert von (131.1 ± 3.8) GPa, während die vollständig entgaste Probe einen Wert von (182.39 ± 3.98) GPa aufweist. Die Härte steigt ebenfalls von (6.48 ± 0.15) GPa des amorphen Zustandes auf (7.68 ± 0.12) GPa der thermisch behandelten Probe an.

Contents

1	Introduction	1
1.1	Aim of This Work	1
2	Theory of Electron Diffraction	3
2.1	Single Atom Scattering	3
2.2	Lattice Scattering	4
2.2.1	Bragg's Law	4
2.2.2	Laue Equation	5
2.2.3	Ewald Sphere	6
2.2.4	Structure Factor	7
3	Specimen Preparation Methods	9
3.1	Introduction to the Intermetallic Co_3Ti	9
3.2	Setting Up the Alloy of Composition: 77at.%Co-23at.%Ti	9
3.3	Melting of the Alloy	11
3.4	Casting Into a Rod Form	12
3.5	Thermal Homogenization and Cutting of the Specimen	12
3.6	High Pressure Torsion Deformation	13
3.7	Electropolishing	15
3.7.1	Electropolishing of Co_3Ti	15
4	Methods of Specimen Analysis	17
4.1	Transmission Electron Microscopy	17
4.1.1	Introduction	17
4.1.2	Image Formation	19
4.1.3	High Resolution TEM	19
4.2	Scanning Electron Microscopy	20
4.2.1	Image Formation	21
4.3	Nanoindentation	22
4.3.1	Introduction	22

Contents

4.3.2	Theoretical Background	24
4.3.3	Possible Errors and Their Compensation	25
4.4	Differential Scanning Calorimetry	26
4.4.1	Introduction	26
4.4.2	Function of a Power Compensated DSC	26
4.4.3	Thermodynamics	27
4.5	Listing of Instruments	28
5	Experimental Results and Discussion	29
5.1	SEM Analysis of the As Cast Alloy	29
5.1.1	State After the Melting and Mixing	29
5.1.2	State of the Alloy After the Casting Into Rod-Form	33
5.1.3	State of the Alloy After Homogenization	35
5.2	High Pressure Torsion Deformation	36
5.3	TEM of the Specimen Deformed With 4 GPa	43
5.3.1	20 Turns at 4 GPa	43
5.3.2	80 Turns at 4 GPa	43
5.4	TEM of the Specimen Deformed With 8 GPa	46
5.4.1	20 Turns at 8 GPa	46
5.5	DSC Measurement Results	48
5.6	Nanoindentation	50
5.6.1	Experimental Setup	50
5.6.2	Results of the Nanoindentation	52
5.7	In-situ Heating Experiment	53
5.7.1	Setup and Preparation	53
5.7.2	Devitrification Observation During Heating	54
5.7.3	Structure Investigation	59
5.8	High Resolution Imaging of the In-situ Devitrified Specimen	62
5.9	Chemical Analysis in the STEM	64
5.10	Ex-situ Bulk Heated Specimens	66
5.10.1	STEM of the Ex-situ Bulk Heated Specimen	69
6	Summary and Conclusions	71
6.1	High Pressure Torsion Deformation and SEM	71
6.2	In-situ Heating Experiment in the TEM	71
6.3	Ex-situ Heating Experiment	72
6.4	Nanoindentation	72

1 Introduction

Amorphous metallic alloys show very promising physical properties and have therefore gained in interest over the last 50 years. They show different electronic [1], magnetic [2] and mechanical [3][4] properties, as compared to their corresponding crystalline phases and are of special interest because of possible technical applications [5]. Unfortunately they also have some disadvantages and limitations, such as their intrinsic brittleness [6], which have to be overcome before these materials will be technically applicable. To modify these properties in the desired way, it is essential to fully understand their mechanisms on a macroscopic, but especially on a microscopic and further also atomic scale [7]. Only by understanding the arrangements and movement of the atoms, the properties can be tuned as wished.

The method of transmission electron microscopy (TEM) has proven in the past to be very suitable for investigation of metallic specimen down to the atomic scale [8][9]. It allows to obtain different signals and imaging contrasts by the use of a variety of imaging techniques, resulting in a fairly complete investigation of the structure of the specimen.

1.1 Aim of This Work

In this work the focus is set onto a intermetallic alloy, composed of Cobalt and Titanium with a 3 to 1 atomic ratio (Co_3Ti). This alloy has interesting characteristics such as a high ordering tendency and might be used as high temperature structural material [10]. It is the aim of this work to study the amorphization and devitrification behaviour of this alloy by electron microscopy methods, nanoindentation and calorimetric methods.

High purity Cobalt and Titanium were used for the setting up of the alloy, which was mechanically processed by severe plastic deformation (SPD) using the method of high pressure torsion (HPT) to obtain a solid state transformation to the amorphous phase. In an in-situ experiment the thermal stability and the devitrification behaviour of the amorphous structure is investigated. High resolution TEM (HRTEM) as well as scanning electron microscope (SEM) methods and scanning transmission electron microscope (STEM) methods are further used to obtain a complete view of the specimen. Also differential scanning calorimetry (DSC) on bulk samples and nanoindentation measurements are carried out to clarify thin foil effects and obtain mechanical properties, respectively.

2 Theory of Electron Diffraction

This section will give a quick introduction to the theory of electron diffraction. For the following it is important to understand the interaction of the high energy electrons and the specimen, as well as to understand what information one can obtain from this.

Electrons are negative charged particles, which by the electromagnetic forces interact with the electrons or the positive charged nuclei of the specimens atoms. The interactions can be categorized in elastic and inelastic scattering, which refers to a non-energy loss or an energy loss interaction. Since elastic scattered electrons are mostly coherent scattered, which means their phase relation is constant, they show interference effects due to their wave nature according to the wave-particle-duality principle. Inelastic scattered electrons on the other hand are in mostly scattered in an incoherent way and therefore behave more like classical particles.

In this introduction we will focus on the coherent elastic scattering and neglect other effects contributing to the finally obtained signal. The phenomenon of elastic scattering will be described in an intuitive way by Bragg's law and we will also see the relation of the periodic structure and what information we can get from it.

2.1 Single Atom Scattering

First we have a look at the interaction of an electron and a single atom. The elastic scattering of the electron by the atom is described using the so called atomic form factor. This is directly connected to the differential elastic cross section for the scattering process, which has to be derived in a quantum mechanical way to take into account the wave nature of the system.

Without any further detail we will write the formula as in [11]. This equation states that the measured angular distribution of the intensity $|f(\Theta)|^2$ is equal to the differential cross section of the atom.

$$|f(\Theta)|^2 = \frac{d\sigma(\Theta)}{d\Omega} \quad (2.1)$$

As already mentioned the electron wave is scattered by the charges from both, the nucleus and the electron orbital. This total charge density of the atom can be described as in Equ. 2.2, where ρ_{nucleus} is the charge distribution of the nucleus and ρ_{orbital} the charge distribution of the electron orbitals [12].

$$\rho(\vec{r}) = |e| (\rho_{\text{nucleus}}(\vec{r}) - \rho_{\text{orbital}}(\vec{r})) \quad (2.2)$$

The electrostatic potential of the atom can be calculated directly by solving the Poisson's equation for the given charge distribution as in Equ. 2.3, where ΔU is the Laplacian of the electrostatic potential.

$$\Delta U(\vec{r}) = \frac{|e|}{\epsilon_0} (\rho_{\text{nucleus}}(\vec{r}) - \rho_{\text{orbital}}(\vec{r})) \quad (2.3)$$

Under the assumption this potential is known, one can now calculate the transition probability from a plane wave of the form $|\Psi\rangle = |e^{2\pi i \vec{k} \cdot \vec{r}}\rangle$ to a scattered wave of the form $|\Psi'\rangle = |e^{2\pi i \vec{k}' \cdot \vec{r}}\rangle$ by using quantum mechanic formalism and defining this probability equal to the atomic form factor as function of the scattering vector $\Delta \vec{k} = \vec{k}' - \vec{k}$, which is the momentum transfer of the elastic scattering process. This leads us to

$$f(\Delta \vec{k}) = \langle \Psi' | U | \Psi \rangle = \int_V U e^{-2\pi i \Delta \vec{k} \cdot \vec{r}} d\vec{r} \quad (2.4)$$

where it is important to note that the atomic form factor can be seen from this as the Fourier transform of the atomic potential.

Transformation using the inverse Fourier transform leads therefore to the potential U . By inserting this into the left hand side of the Poisson's equation Equ. 2.3 and taking the inverse Fourier transform of the right hand side, an equation as function of $\Delta \vec{k}$ is obtained. For this the contribution of the electron orbitals has to be described by the X-ray scattering factor $f_x(\Delta \vec{k})$ and the nucleus by a delta function with its proton number Z . The result is Equ. 2.5.

$$f(\Delta \vec{k}) = \frac{|e|}{4\pi^2 \epsilon_0 |\Delta \vec{k}|^2} (Z - f_x(\Delta \vec{k})) \quad (2.5)$$

This is a very important result, since it shows us that the most of the elastic scattered electrons get scattered in the forward direction, showing a strong decay for momentum transfers with higher $\Delta \vec{k}$. Of course this result only describes the scattering of a single atom, but what we want is to see the scattering from specimen which show a periodic arrangement of a lot of such atoms.

2.2 Lattice Scattering

Before we derive a formula for the scattering of a periodic structure including the result from the single atom scattering, we will see a very intuitive way to describe the phenomenon of diffraction by lattice planes. Even if it's not describing the full physical phenomenon of the scattering process, this model is applicable to describe quite a lot of the experimental results.

2.2.1 Bragg's Law

We assume that we can describe the periodic structure of the crystal by a set of planes parallel to each other with a constant spacing d in-between them (cf. Fig. 2.1). Also we assume the planes scatter the incident beam under the same angle Θ if measured between the plane and

the incident beam propagation direction \vec{k} . Bragg assumed that diffracted plane waves will only show constructive interference if the path difference between the two waves is a multiple of the wavelength λ . If we describe the difference in path δ , a plane wave sees between the two lattice planes, as functions of inter planar distance d and incident angle Θ we obtain $2\delta = 2d \sin(\Theta)$. Since this has to be a multiple of the wavelength λ we finally get the well known Bragg's law Equ. 2.6, with n being a natural number [13].

$$2d \sin(\Theta) = n\lambda \quad (2.6)$$

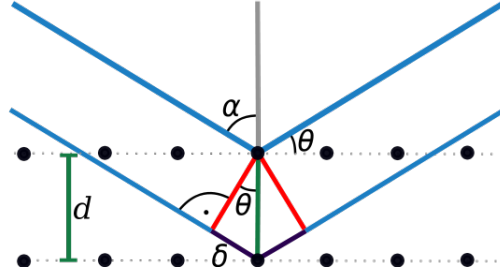


Figure 2.1: Schematic illustration of the scattering of a plane wave on parallel lattice planes with spacing d . [14]

2.2.2 Laue Equation

A similar result is obtained if we start with a plane wave which gets scattered by a Bravais lattice. Two points of the lattice spaced by \vec{R} give again a path difference for the scattered waves, what leads to destructive interference if the path difference is not a multiple of the wavelength λ . Also the angle between the incident wave vector \vec{k} and \vec{R} creates a path difference (cf. Fig. 2.2).

By summing them up we get

$$\vec{R} \cdot \frac{\vec{k}}{k} - \vec{R} \cdot \frac{\vec{k}'}{k'} = n\lambda \quad (2.7)$$

and with $k = k' = 2\pi/\lambda$

$$\vec{R} \cdot (\vec{k} - \vec{k}') = 2\pi n. \quad (2.8)$$

Multiplying both sides of the equation with the imaginary number i and taking them to the exponential, finally results in

$$e^{i\vec{R} \cdot (\vec{k} - \vec{k}')} = e^{2\pi i n} = 1 \quad (2.9)$$

which is equivalent to the definition of the reciprocal space, where we can say that a plane wave with initially unconstrained \vec{k} fits onto to the lattice if $e^{i\vec{R} \cdot \vec{k}} = 1$ is satisfied. The wave vectors \vec{k}

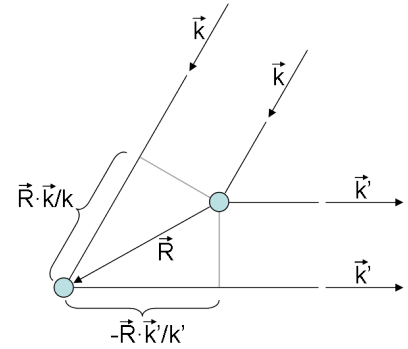


Figure 2.2: Schematic representation of the interference as described by Laue. [15]

for which this is true then get denoted as \vec{G} or \vec{g} . By this relation we obtain the Laue equations in the form

$$\Delta\vec{k} = \vec{g}. \quad (2.10)$$

Here it is important to note that there are two different types of definitions for the \vec{k} -vectors. One incorporates the factor 2π and therefore gives $|\vec{k}| = \frac{2\pi}{\lambda}$ whereas the other one doesn't and therefore is $|\vec{k}| = \frac{1}{\lambda}$. In electron microscopy the later one is more commonly used and we will stick to that definition from here on. The other one is more often found in solid state physic calculations.

2.2.3 Ewald Sphere

The result from the Laue equations can be interpreted in a graphical way by the so called Ewald sphere in the reciprocal space. First of all the reciprocal lattice is constructed using the reciprocal basis vectors \vec{b}_j , that are obtained from the real space vectors \vec{a}_i by the definition $\vec{a}_i \cdot \vec{b}_j = \delta_{ij}$. Then the incident wave is drawn into the reciprocal lattice, represented by its wave vector \vec{k} . The magnitude corresponds to the inverse wavelength and the direction to the incident direction relative to the lattice. The point of the wave vector is drawn so that it finishes on one of the lattice points. From this point a sphere with radius $|\vec{k}|$ is drawn around the starting point of the \vec{k} -vectors, indicating all points in reciprocal space for which the energy is conserved for each scattered wave vector. From Equ. 2.10 we see that the waves only interfere constructively for wave vectors which correspond to reciprocal lattice vectors. So by combining this with the energy conservation we see that the interference is only constructive for lattice points laying on the surface of the Ewald sphere.

In theory, this would lead to only very few constructive interfering waves, since there are not that many points laying on the Ewald sphere. Under experimental conditions this is not true because of the finite size of the specimen, which leads to a deviation \vec{s} from the strict mathematical form of Equ. 2.10.

$$\Delta\vec{k} = \vec{g} + \vec{s} \quad (2.11)$$

The graphical representation of this deviation corresponds to a finite size of the reciprocal lattice "points". Especially in TEM larger deviations are allowed since the specimen thickness is very small in one direction. This means the reciprocal lattice points have the form of one dimensional elongated ellipsoids. Also, since the electrons have a high kinetic energy and therefore a long wave vector, the radius of the Ewald sphere is large and the curvature low. This means that if a lattice point satisfies the Laue equation, a variety of neighboring points will satisfy the equation with a small \vec{s} -value too. Because of this under most operation conditions in the TEM, only spots of the same so called Laue zone will be excited.

2.2.4 Structure Factor

With Equ. 2.5 we derived the scattering behaviour of a single atom. But the specimens we are looking at in the microscope are composed of an incredible huge number (in the order of 10^{23} atoms) and the scattering behaviour is dependent on all of them. The good thing about crystalline specimen is that they have a periodic structure with a elementary unit cell, which in most cases consists only of a few atoms. This allows us to describe the problem in a easier way by taking advantage of this.

The scattering of the specimen can be described by integrating the density distribution of the scattering objects, in electron diffraction the electron density $\rho(\vec{r})$ over the whole unit cell V_e by taking into account the phase shifts between scattering centers $\varphi(\vec{r})$. This gives the following formula [16]

$$\int_{V_e} \rho(\vec{r}) e^{2\pi i \varphi(\vec{r})} d\vec{r}. \quad (2.12)$$

From the Laue equation (cf. Equ. 2.10) we already know that the wave interference is only constructive for scattering vectors which are equal to a reciprocal lattice vector, which by putting into Equ. 2.8 gives a phase shift of $\varphi(\vec{r}) = \vec{g} \cdot \vec{r}$, giving us [16]

$$F_{\vec{g}} = \int_{V_e} \rho(\vec{r}) e^{2\pi i \vec{g} \cdot \vec{r}} d\vec{r}. \quad (2.13)$$

So the structure factor $F_{\vec{g}}$ is defined as the Fourier transform of the scattering charge distribution $\rho(\vec{r})$ (in analogy to Equ. 2.4). This result can be transformed into a more suitable form for direct calculations of the structure factor by splitting $\vec{r} = \vec{r}_i + \vec{r}'$, where \vec{r}_i is the i -th atom in the unit cell and \vec{r}' is the vector from the atom to the integration position \vec{r} .

This leads to

$$F_{\vec{g}} = \sum_i \int_{V_e} \rho_i(\vec{r}') e^{2\pi i \vec{g} \cdot \vec{r}_i} e^{2\pi i \vec{g} \cdot \vec{r}'} d\vec{r}' = \sum_i e^{2\pi i \vec{g} \cdot \vec{r}_i} \int_{V_e} \rho_i(\vec{r}') e^{2\pi i \vec{g} \cdot \vec{r}'} d\vec{r}' \quad (2.14)$$

and if we recall Equ. 2.4 the last factor in Equ. 2.14 is the atomic form factor (denoted f_i) for the i -th atom.

By this the final form for the structure factor is as follows.

$$F_{\vec{g}} = \sum_i e^{2\pi i \vec{g} \cdot \vec{r}_i} f_i = \sum_i f_i e^{2\pi i [h r_{i,1} + k r_{i,2} + l r_{i,3}]} \quad (2.15)$$

Here the definition $\vec{a}_i \cdot \vec{b}_j = \delta_{ij}$ for the reciprocal lattice is used and the j -th component of the i -th atom is denoted as $r_{i,j}$. This formula finally allows to calculate the diffraction intensity $I \propto |F_{\vec{g}}|^2$ of a certain set of lattice planes for a known structure by calculation the sum over all lattice positions with the corresponding atomic form factor at each position.

3 Specimen Preparation Methods

3.1 Introduction to the Intermetallic Co_3Ti

Co_3Ti is an intermetallic alloy with an L_{12} structure, which consists of 4 primitive cubic cells sitting in the positions of the fcc basis. In the so obtained superstructure the Ti-atoms sit on the corners of the cube while the Co-atoms sit on the centers of the faces (cf. Fig. 3.1). This leads to an atomic composition of 75at.%Co and 25at.%Ti.

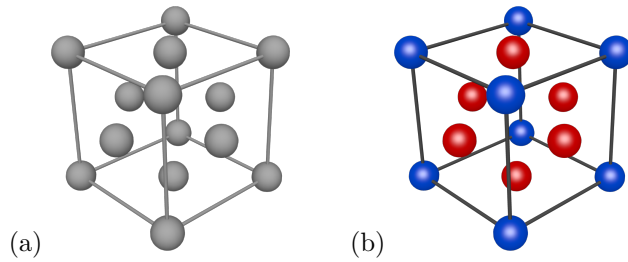


Figure 3.1: In the face centered cubic unit cell all lattice points are equivalent, as shown in (a). In (b) we see the L_{12} unit cell corresponding to an intermetallic Co_3Ti alloy, where the atoms sit in an ordered way on the lattice points. On the corners there sit the Ti-atoms (blue) and in the face centers there sit the Co-atoms (red).

This means the primitive cubic sub lattices of the Co-atoms are shifted by $\vec{r}_1 = \frac{1}{2}(1, 1, 0)$, $\vec{r}_2 = \frac{1}{2}(1, 0, 1)$ and $\vec{r}_3 = \frac{1}{2}(0, 1, 1)$ relative to the also primitive cubic Ti-lattice. Since the structure shows this ordered positions of the atoms in the unit cell, the structure factor as derived in Equ. 2.15 will be different as compared with a statistical distribution of the atoms on the lattice positions. For the disordered case, the mean atomic form factor f per lattice position is the same, leading to a scattering behaviour as a monoatomic fcc

lattice. In this case the structure factor is $4f$ for all h, k, l even or all odd, and 0 in the other cases. For the ordered structure this doesn't hold since the atomic form factors on the lattice positions are not the same, therefore allowing more combinations of the h, k, l sets. This additionally allowed reflections in a diffraction pattern are so-called superlattice reflections. How strong they are depends on the difference of the atomic form factors.

3.2 Setting Up the Alloy of Composition: 77at.%Co-23at.%Ti

The first production step is to get the alloy with the desired chemical composition and structure, which in this case is Co_3Ti in the ordered L_{12} structure. According to the phase diagram (cf. Fig. 3.2), this phase is formed in a preferred way at a nominal 23at.%-Ti concentration (over the

whole temperature range, shown by the line in the figure) [17]. Since it is easier to measure the weight of the material, first the mass percentage corresponding to the atomic number percentage is calculated. For this lets assume we have 23 atoms of Ti and 77 atoms of Co, and therefore a total of 100 atoms. We call u_{Ti} the mass of a Ti-atom and u_{Co} the mass of a Co-atom. Then simple calculations as in Equ. 3.1 and Equ. 3.2 gives the mass percent for each element. For the calculation $u_{\text{Ti}} \approx 47.947 \text{ u}$ and $u_{\text{Co}} \approx 58.933 \text{ u}$ where used [18].

$$m_{\%,\text{Ti}} = \frac{m_{\text{Ti}}}{m_{\text{Ti}} + m_{\text{Co}}} = \frac{23 \cdot u_{\text{Ti}}}{23 \cdot u_{\text{Ti}} + 77 \cdot u_{\text{Co}}} \approx 19.5 \% \quad (3.1)$$

$$m_{\%,\text{Co}} = 1 - m_{\%,\text{Ti}} \approx 80.5 \% \quad (3.2)$$

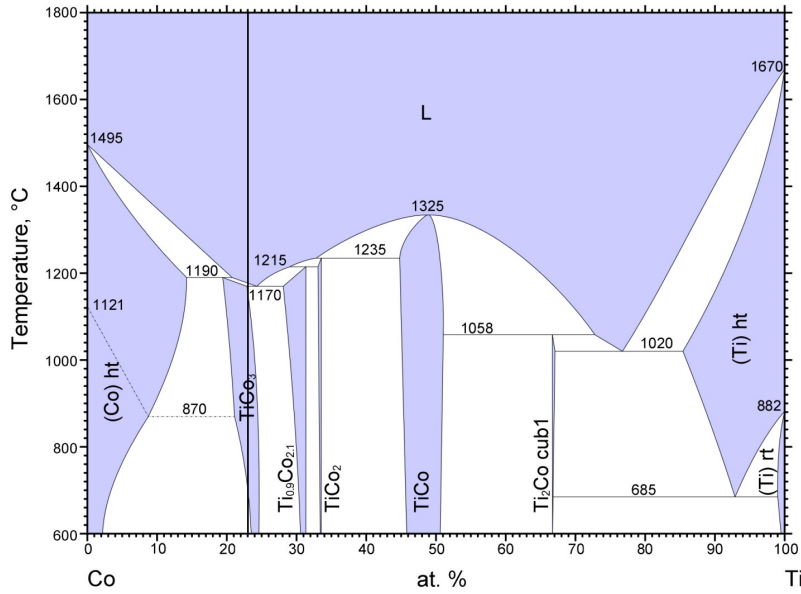


Figure 3.2: Phase diagram for Co-Ti alloys with a line showing the desired concentration and the corresponding phase. [17]

To see how many material is needed for a rod with desired dimensions, the density of Co_3Ti using the lattice constant $a = 0.3628 \text{ nm}$ [19] is calculated and multiplied with the volume. Finally the mass of the pure metals is calculated using Equ. 3.1 and Equ. 3.2. Tab. 3.1 gives the masses used in this alloying set.

Other samples made out of a piece bought from the company “Hauner Metallische Werkstoffe” showed several TiO_2 particles as analysed by TEM. Therefore the goal is to produce very pure sample material with a low concentration of TiO_2 . For this Co and Ti with a purity of 99.995 %

m_{Co}	8.89 g
m_{Ti}	2.15 g
m_{total}	11.04 g

Table 3.1: Mass of material needed for the production of a rod (6 mm diameter, 50 mm long)

are ordered from the company Alfa Aesar on their homepage www.alfa.com. Also on all further preparation steps minimization of the O_2 contamination of the alloy is tried.

The pure metals are delivered as slugs, which then are weighed on a scale with 0.0001 g precision and mixed according to the right mass percentage. Since not the full 11.04 g of material could be melt together in one step (see Sec. 3.3), because of the size limit of the levitation furnace, three sets with approximately the desired mass ratio are weighed (see Tab. 3.2).

Number of set	m_{Co} [g]	m_{Ti} [g]
1	3.5319	0.8592
2	3.5875	0.8666
3	1.7490	0.4310
total	8.8684	2.1568

Table 3.2: Mass of the 3 sets used for the inductive melting

3.3 Melting of the Alloy

To melt and mix the specimen material an induction furnace is used, heating the Co and Ti pieces with the high induction currents under an argon atmosphere over their melting point and mixing them because of the circular currents in the metals. The argon atmosphere in addition to reduce contamination assures that no alloying material gets lost because of evaporation. Also both metals fortunately have a similar vapor pressure.

Prior the melting the Co and Ti pieces are cleaned in ethanol with ultrasound vibrations to get rid of contamination on the surface. Then they are placed in the copper furrow of the furnace, which is sealed inside a quartz glass cylinder. As oxygen getter material an extra piece of Ti is put in a separated furrow of the furnace right near the entrance valve of the Ar gas. The cylinder is evacuated using a rotation pump to a pressure lower then 10^{-3} mbar (limit of the display) and refilled with Ar of 6n purity at a pressure of ~ 30 mbar. Evacuation and refilling of the tube is repeated 4 times, to reduce the O_2 concentration in the cylinder. In the end a static argon pressure of ~ 30 mbar is set up and the specimen are heated up to the melting point.

Due to the inductive levitation only the cold metals touch the copper furrow, whereas the hot and the molten materials never touch it and therefore no contamination is caused by the furrow. To assure the materials mix very well after cooling down of the slugs, the glass cylinder is opened and the slugs turned around.

The whole cycle is repeated 3 times as described.

3.4 Casting Into a Rod Form

For further processing a rod formed specimen is desired, therefore a crystal growth furnace is used to cast the alloy into a crucible. An Al_2O_3 tube surrounded by a furnace is evacuated and the furnace is heated up to the melting temperature of the alloy ($\sim 1190^\circ\text{C}$, see Fig. 3.2) without any material in the tube for degassing it. During degassing tube is evacuated continuously with the vacuum pump system consisting of a rotary pump and an oil diffusion pump, until a final pressure of about 1.5×10^{-5} mbar is reached.

After this first run, the sample material is put in the crucible (a one end closed tube of Al_2O_3 of 1 cm diameter and about 10 cm length), which is positioned inside the tube of the furnace. After the tube is evacuated again, the casting process is started; first slowly to make sure that the contamination caused by the opening of the furnace is reduced to a minimum. A value of 1300°C is set on the control unit to reach the final temperature of 1220°C inside, as measured by a thermal element right under the crucible. At this time the vacuum reached pressure values of 8×10^{-6} mbar to 1×10^{-5} mbar. Finally the furnace is moved with a speed of $6.5 \frac{\text{cm}}{\text{h}}$ away from the fixed crucible to produce the polycrystalline Co_3Ti rod.

After the furnace cooled down, the rod is taken out of the crucible, unfortunately leading to destruction of the crucible, because of the alloy sticking to the wall.

3.5 Thermal Homogenization and Cutting of the Specimen

To obtain a homogeneous structure in all the areas of the rod, the alloy is annealed in the furnace for ~ 100 h at a temperature of 950°C . For this purpose an other furnace is used, which again first had to be cleaned by evacuation of the quartz glass tube and by heating up to the desired temperature. The sample material is put in the horizontal lying glass tube into a holder and the pressure is reduced to a level of 10^{-5} mbar with the vacuum pumps system (rotary pump and oil diffusion pump). Then the tube is flooded with argon gas until a small overpressure is build up. Now the heating is started with the desired temperature of 950°C , logging the temperature during the entire process.

The material is cut by spark erosion in small discs of 8 mm diameter and 0.55 mm thickness for high pressure torsion deformation. The spark erosion machine removes sample material by building up

a high tension between the sample and a specifically formed tool (i.e. a running wire) over a RC - circuit, which leads to the formation of a spark. The surface of the material is molten locally and taken away. By this also more complex forms can be obtained. The metal and the processing tool are submerged into an oil which works as dielectric medium and also flushes away the dirt. For this cutting process the material has to be glued with a conducting glue to a sample holder.

3.6 High Pressure Torsion Deformation

The severe plastic deformation (SPD) of materials to produce ultrafine and nano grained materials is at the moment a very active field in materials science (cf. [20] and [21]). There are different techniques under development to produce bulk specimens with a homogeneous grain size in the range of 100 nm to 1000 nm (referred to as ultra fine grained materials) and grain sizes of under 100 nm, called nanocrystalline materials. These materials show significant differences in their properties as compared to the unprocessed materials, with the processing especially affecting their mechanical properties.

One of the already well investigated and widely used techniques is the high pressure torsion deformation (HPT) [22]. In HPT the deformation is carried out by applying a quasi-hydrostatic pressure onto a disk-shaped specimen and acting with a torsional force by rotating the upper or bottom anvil with respect to the other, fixed one (cf. Fig. 3.3). In the past different experimental setups have been developed, from which today mostly the Fig. 3.3c geometry is used, because it constrains the specimen with little specimen shape change and allows the use of higher pressures as compared to the other geometries.

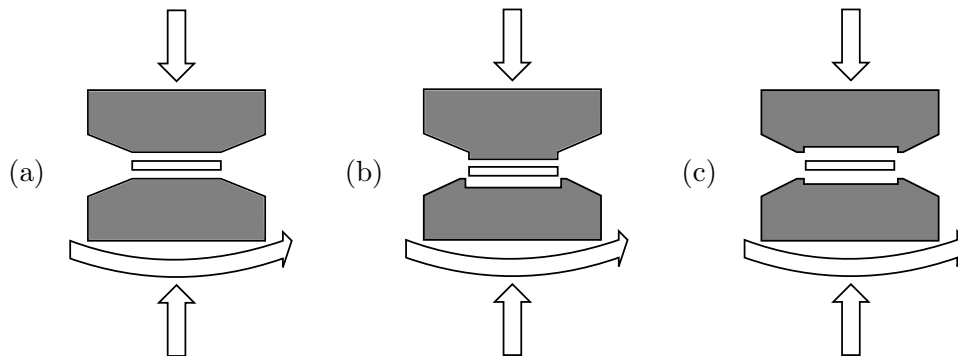


Figure 3.3: The figure shows three different geometries used for HPT deformation of specimen. (a) unconstrained geometry (b,c) constrained geometry. [22]

The severe deformation is achieved by placing the disk shaped specimen between the two anvils, having cavities each. The specimen is slightly higher than the sum of the two cavity depths, avoiding the touching of the anvils during the processing. By applying pressure onto the anvils,

the specimen gets compressed, confined by the anvils which allow plastic flow only in the region between the small spacing of the anvils. By this a quasi-hydrostatic pressure is obtained. The actual deformation is then carried out by rotation one anvil against the other, introducing high shear stress leading to activation of dislocation slip and other deformation processes, such as mechanical twinning and the formation of shear bands. The specimen surfaces are held fixed by the high friction between specimen and anvil, achieved by the high pressure acting on them. To increase the friction even more and therefore avoid slipping during the deformation, the anvil and specimen surfaces can be sandblasted before processing.

Assuming ideal conditions, the degree of deformation is proportional to the number of revolutions N of the rotating anvil and the radial distance from the rotation center r . In Fig. 3.4 a schematic representation of the specimen is given, showing in addition the displacement dl obtained by infinitesimal rotation of the angle $d\Theta$, for which $dl = rd\Theta$ holds. At a given distance r from the center the infinitesimal torsional strain $d\gamma$ is therefore given by Equ. 3.3, where h is the fixed height of the disc.

$$d\gamma = \frac{dl}{h} = \frac{rd\Theta}{h} \quad (3.3)$$

Finally integration over the full angle gives the desired relation between torsional strain and number of rotations (Equ. 3.4).

$$\gamma = \int_0^{2\pi N} \frac{r}{h} d\Theta = \frac{2\pi Nr}{h} \quad (3.4)$$

The von Mises strain can be calculated for comparison of the true strain with other SPD methods using Equ. 3.5 [22].

$$\epsilon = \gamma/\sqrt{3} \quad (3.5)$$

This only holds for small strains, for higher straining with $(2\pi Nr)/h \gg 1$ Equ. 3.6 is more precise, as discussed in [23].

$$\epsilon = \ln \left(\frac{2\pi Nr}{h} \right) = \ln(\gamma) \quad (3.6)$$

Under real conditions there is always some plastic specimen reduction and the deformation itself is not radial symmetric. If the thickness reduction during deformation is also taken into account, a more precise calculation of the true strain can be done using Equ. 3.7 [22][23].

$$\epsilon = \ln \left(\frac{2\pi Nr h_0}{h^2} \right) \quad (3.7)$$

One has to be careful when calculating the true strain values from a HPT deformed sample, as the deformation can not only be inhomogeneous in the radial direction, but also in the axial direction

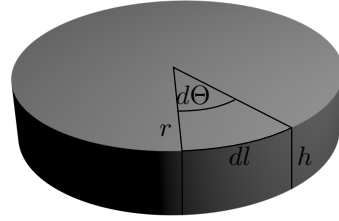


Figure 3.4: The figure shows a schematic representation of the specimen geometry. The torsional strain is not the same over the whole specimen, but has a radial dependency. [22]

due to work softening as shown by D. Geist [24]. The deformation is in this case carried out almost entirely on localized nanocrystalline regions, softer than their neighboring coarse grained regions. This leads to a large strain gradient and huge deviations of the actual local shear stress from the calculated value.

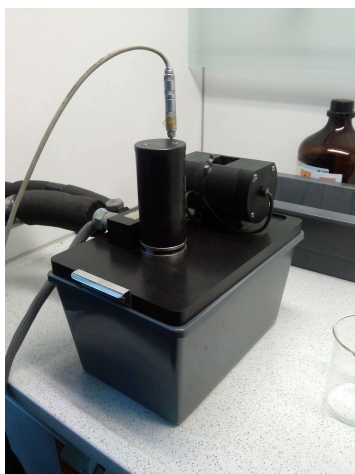
3.7 Electropolishing

One of the most widely used final thinning techniques for TEM specimen is the electropolishing process. As well described in the book of P.J. Goodhew [25], electropolishing is similar to chemical etching but with an additional electrical potential applied between a cathode and the specimen, which makes the process more controllable. During the process two layers are formed on the specimen surface, one thicker which is smoothing the macroscopic irregularities and a thinner one which polishes on a finer scale. The formation of this layers is essential for obtaining a thin and smooth surface which can be penetrated by the electron beam. The results obtained with this method are mostly very good if one can find the right parameters for the electrochemical process, which can be quite difficult, as you can control the applied voltage, the composition and the temperature of the electrolyte, the flow rate and the initial specimen dimensions. Therefore the sharing of good working parameters if found is desired in the community.

3.7.1 Electropolishing of Co_3Ti

As mentioned, electropolishing reduces the sample thickness electrochemically, to a thickness which allows the electron beam to penetrate the sample ($<200\text{ nm}$). To polish Co_3Ti an electrolyte solution consisting of 1/3 nitric acid and 2/3 methanol was produced by slowly filling the 250 mL of nitric acid in the 500 mL methanol, to avoid heating up during mixing. This solution was put in the twin jet electropolishing machine (Struers Tenupol-3, cf. Fig. 3.5a and Fig. 3.5b) and cooled down to -25°C to reduce the reaction speed (with a Lauda RK 8 CS, cf. Fig. 3.5c). Then a disc was put into the holder (cf. Fig. 3.5b), connecting it to a potential via an electrode of platinum. A voltage of 4 V and a flow rate of 4.5 were used for electropolishing. Before beginning with the thinning process, we prepared 4 methanol baths to clean the sample and to stop etching by diluting the acid after taking the specimen out of the machine. The machine stops polishing immediately when a hole is formed and light shines from a source on one side of the specimen through this hole onto a photodiode on the other side. Then the holder has to be pulled out fast from the machine and put in the first cleaning-bath for 4-5 seconds, keeping the methanol flowing around it by carefully moving the holder up and down. In the second bath the holder is opened and the specimen falls onto a mesh, with which it is transferred into the next bath. Finally the specimen is transferred with tweezers into the "pro-analysis" pure methanol, also carefully moving it around in the liquid to neutralize any residual acid. With this technique we can get a hole with a very thin

rim, thin enough (in a region up to 5 μm from the hole) to be penetrated by the electron beam in the TEM, using an acceleration voltage of 200 kV.



(a) Struers Tenupol-3 twin-jet electropolishing machine.



(b) Struers Tenupol-3 specimen holder.



(c) Lauda RK 8 CS cooling regulator for the electrolyte.

Figure 3.5: The pictures show the twin-jet electropolishing equipment used for the TEM-specimen preparation.

4 Methods of Specimen Analysis

4.1 Transmission Electron Microscopy

4.1.1 Introduction

A transmission electron microscope (TEM) is a powerful tool when it comes to specimen analysis. The huge advantage over classical light microscopes is clearly the higher resolution, which is obtained by using the electron wave with smaller wavelength rather than light which is limited in resolution by the theorem of Abbe according to Equ. 4.1.

$$d = 0.61 \frac{\lambda}{n \sin \alpha} \quad (4.1)$$

In this equation d is the distance which is still possible to resolve when using light of a wavelength λ , n is the index of refraction and therefore given by the medium in which the optics are used (normally air) and α is half the collection angle of the objective lens. The TEM improves the spacial resolution by accelerating electrons in an electrostatic potential to high energies, leading to a reduction of their wavelength according to the theorem of de Broglie $\lambda = \frac{h}{p}$ which by respecting the effects of special relativity leads to Equ. 4.2 (cf. [12]).

$$\lambda = \frac{h}{\sqrt{2m_0E \left(1 + \frac{e}{2m_0c^2} E\right)}} \quad (4.2)$$

Since moving charges interact with magnetic fields, electromagnetic lenses are used to focus the electrons, which gives flexibility by controlling the focal length via the currents, but unfortunately also introduces aberrations reducing the resolution and image quality.

The other advantage of electron microscopes is the number of signals obtained by different effects of electron specimen interaction, which can be used for investigations regarding different aspects of the specimens properties.

In the following a short overview and explanation of the signals and the information obtained by them is given.

- **Diffraction contrast:** A contrast is generated on the fluorescent screen of the microscope by selecting electrons which were diffracted by the specimen elastically under certain angles. This contrast is sensible to defects as dislocations and other effects which change locally the diffraction properties of the specimen (grain orientation, bending of the specimen,...).

- **Phase contrast:** The contrast in the image is obtained by an interference phenomenon, generated by phase shifts in different regions of the specimen. This contrast is mostly used in high resolution TEM.
- **Amplitude contrast:** Variations in the intensity of the forward scattered beam due to differences in mass and thickness.
- **X-ray detection:** By the inelastic interaction of the electrons with the specimen a characteristic X-ray radiation is generated, which can be used to obtain information of the chemical composition of the specimen.
- **Electron energy loss spectroscopy (EELS):** EELS is a technique which analyses the energy losses in the forward scattered electrons by collecting the energy spectrum using a magnetic prism. In the spectrum a variety of physical properties such as plasmon excitations, chemical element information and bondings is present.

In Fig. 4.1 a schematic drawing of a typical TEM is illustrated. The electrons get emitted by an electron source (typical sources are: field emission gun, LaB_6 , Tungsten) by heating, pass the small aperture of the Wehnelt cylinder and get accelerated by a high voltage to energies in the range from 60 keV to 300 keV by the high tension between source and anode. The second stage is a condenser system which is used to create a parallel beam and a homogeneous illumination of the specimen. The specimen sits in a special holder inserted into the goniometer which allows the mechanical movement of the specimen relative to the electron beam. Right under the specimen sits the objective lens, which is the most important lens for imaging and magnifies the object wave with additional projector lenses onto the fluorescent screen or a CCD (charge-coupled device) camera for recording. Additional deflector lenses allow the positioning and deflection of the beam.

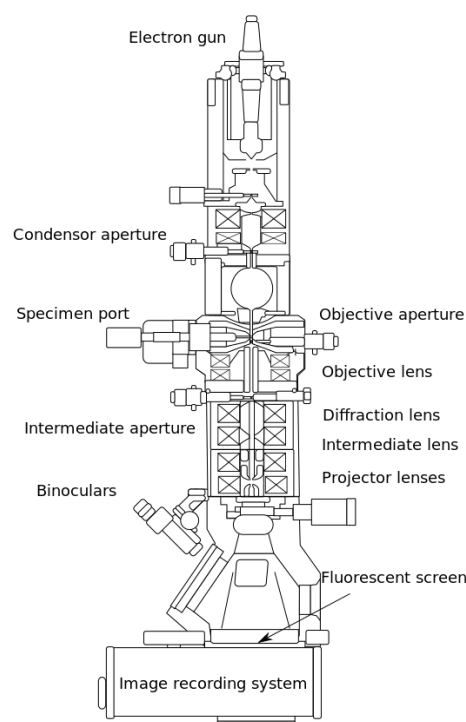


Figure 4.1: In the figure a schematic representation of a typical transmission electron microscope setup is shown. [26]

4.1.2 Image Formation

The variety of signals and the flexibility by being easily able to change the focal lengths of the magnetic lenses, allows to use different imaging modi in a TEM. In material science the image formation by selecting different by the specimen deflected beams is often used. By placing an aperture in the back focal plane of the objective lens around the beam, blocking all the information from the otherwise scattered electrons, the image is formed. This is called **bright-field** or **dark-field** imaging, depending on the beam selected by the aperture. In bright-field imaging the forward scattered beam is selected by the aperture, creating an image of the forward scattered exit wave of the specimen. The same is used in dark-field imaging, this time using a deflected exit wave. As mentioned before the contrast generated by the deflection is sensible to orientation changes and defects, which locally destroy the specimens periodicity and therefore also influence the elastic scattering behavior of the electron wave.

Another very important imaging mode is the so called **diffraction mode**. The tunable magnetic lenses allow us to change the magnetic field in them so, that an image of the back focal plane of the objective lens is obtained. The information in the so obtained image is equivalent to the mathematical Fourier transformation of the exit wave and therefore all the information about spacial frequencies of the specimen is contained in it. This is a powerful imaging technique as it allows a quantification of the structural properties as lattice parameters, lattice type, atomic ordering and grain orientation down to the nanometer scale. This is similar to the diffraction patterns obtained by X-ray diffraction, but using the stronger probe-specimen interaction forces of the electrons. This leads also to effects which in X-ray scattering can be neglected such as dynamical scattering. A short introduction to electron scattering of periodic structures such as crystals and the relation between structure factor and electron intensity as a function of scattering angle is given in Chap. 2.

4.1.3 High Resolution TEM

High resolution TEM (HRTEM) uses mostly a phase contrast to form the image. By looking at Equ. 4.1 one is tempted to say the limiting factor for the resolution is giving by the wavelength and therefore by the kinetic energy of the incident electrons. In reality we are quite strongly limited by the aberrations introduced by the magnetic lenses of the TEM, described mathematically by the microscopes point spread function. Denoting the exit wave of the electrons from the specimen with $\Psi(\vec{r})$ and the point spread function by $T(\vec{r})$ the image plane wave $\Psi_i(\vec{r})$ can be described as the convolution of the two functions as Equ. 4.3 (cf. [12]), assuming linear image formation.

$$\Psi_i(\vec{r}) = \Psi(\vec{r}) \otimes T(\vec{r}) \quad (4.3)$$

By applying the convolution theorem to Equ. 4.3, the relation in form of functions in reciprocal

space is obtained (cf. Equ. 4.4).

$$\tilde{\Psi}_i(\vec{k}) = \tilde{\Psi}(\vec{k}) \cdot \tilde{T}(\vec{k}) \quad (4.4)$$

So in the case of (idealized) linear image formation the image is formed by multiplication of the reciprocal representation of the exit wave and the so called contrast transfer function. This contrast transfer function can in this form easily be described as product of functions introducing the point spread in real space. So we can describe the influence of the microscope on the final image as in [11]

$$\tilde{T}(\vec{k}) = A(\vec{k}) \cdot E(\vec{k}) \cdot B(\vec{k}) \quad (4.5)$$

In Equ. 4.5 $A(\vec{k})$ describes the limitation of spatial frequencies by apertures, $E(\vec{k})$ describes the spacial frequency limitation by the finite size and chromatic effects of the source whereas with $B(\vec{k})$ we will denote the aberrations introduced by the lens system. As described in more detail in [12] and [11] this function can be described as $B(\vec{k}) = \exp(i\chi(\vec{k}))$, where $\chi(\vec{k})$ (cf. Equ. 4.6) describes the phase shift introduced by defocus and spherical aberration, leading to the contrast variations in the obtained image.

$$\chi(\vec{k}) = \pi \Delta f \lambda k^2 + \frac{\pi}{2} C_s \lambda^3 k^4 \quad (4.6)$$

In Equ. 4.6 Δf is the defocus of the objective lens and C_s describes the spherical aberration, which strongly affects especially the high spacial frequencies and by this limits the resolution of the microscope.

So by $\tilde{T}(\vec{k})$ we can describe the contrast of the obtained image as a function of spacial frequency \vec{k} , defocus Δf and C_s . This allows the microscopist to directly influence the contrast with the knowledge that by changing the defocus he changes the phase shift as described before. $\tilde{T}(\vec{k})$ has multiple zero crossings when plotted as a function of reciprocal space vectors \vec{k} , meaning that this frequencies are not transferred to the image and their contribution therefore is lost. Therefore one can try to optimize $\tilde{T}(\vec{k})$ by balancing the effect of spherical aberration against Δf as described by Scherzer in 1949. The Scherzer defocus can be derived as Equ. 4.7 (cf. [11]).

$$\Delta f = -1.2(C_s \lambda)^{1/2} \quad (4.7)$$

Using this parameter gives the best resolution which is directly interpretable and doesn't uses techniques as bandpass image formation, where only the information of a spacial frequency band is used.

4.2 Scanning Electron Microscopy

In contrast to TEM imaging, in the Scanning Electron Microscope (SEM) the specimen is analyzed by scanning an electron probe with finite but small size over its surface, collecting information

from the electron specimen interaction for each point. By this an image of the specimen can be obtained by scanning over a rectangular shaped region, where each analyzed point of the surface is then represented by a digital pixel value. This allows to form different images by using different interaction information as we will see in the next section. Also it is possible to get multiple information from different detectors at the same time.

The different imaging approach also leads to a totally different design of the microscope (cf. Fig. 4.2). Using this approach the main focus is onto obtaining a fine probe to analyze small local regions of the specimen surface. Since the interaction volume is always larger then the actual probe size, this gives finally the resolution limit of the image. There is practically no imaging lens system needed, since the electrons and photons obtained from interactions can be collected directly by detectors which transform the information into an electrical signal, used for the digital image formation.

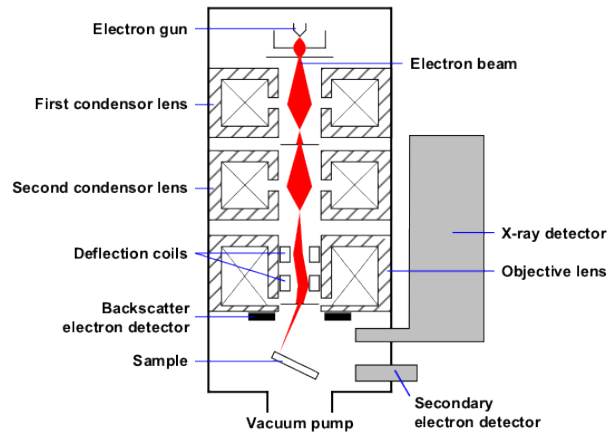


Figure 4.2: In the figure a schematic representation of a scanning electron microscope setup is shown. [27]

4.2.1 Image Formation

The possible signal for image formation in the SEM are the following (cf. Fig. 4.3):

- **Backscattered electrons:** The by Rutherford scattering backscattered electrons can be collected for each point of the specimen.
- **Secondary electrons:** The secondary electrons arise from inelastic scattering of the incident electrons, which transfer energy and momentum to the specimen. This energy and momentum is transferred to other atoms in a chain reaction, resulting finally in the emission of the electron from the specimen surface. These electrons have lower energy than the backscattered ones and can by this be collected independently by applying an attractive potential to the detector window. Auger electrons are emitted when the energy for the filling of a inner shell electron state vacancy results in the emission of a electron otherwise than X-ray radiation.
- **X-ray radiation:** Also by inelastic scattering of the incident electrons lower orbital electrons of the specimen are knocked out of their orbital resulting in an excited state atom,

which reduces its energy by relaxation of a higher orbital electron to the unoccupied state and the emission of a photon with the corresponding energy. Knowing the characteristic transitions and their probability for each element, quantitative information about the chemical composition of the specimen can be made by using the collected intensities for calculations, assuming a mathematical model.

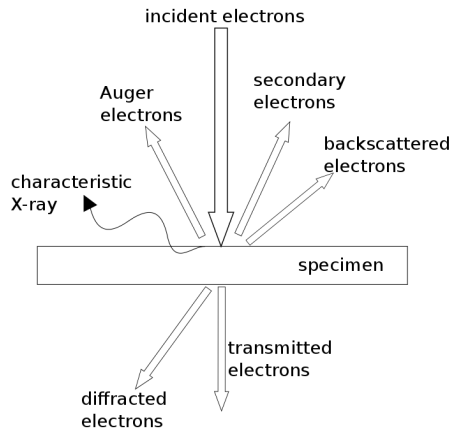


Figure 4.3: Schematic representation of different signals obtained by electron-specimen interactions in different operation modes of an electron microscope.

4.3 Nanoindentation

In the following the method of nanoindentation for measuring the hardness and the elastic modulus of a specimen will be introduced. Further and more detailed information can be found in the article by Oliver and Pharr [32].

4.3.1 Introduction

Within the terminology with hardness one means the resistance of a specimen to plastic deformation of any kind. Since that is a quiet general expression, depending on a lot of experimental parameters, one has to define a special setup with given conditions under which the measurements have to be carried out. Under these conditions, it is then possible to derive quantitative values, which are comparable with each other and therefore have a scientific significance.

Such a standardization of the experimental setup has been carried out in the past, focusing especially on the measurement by indentation of a “harder” probe into the surface of a “softer” specimen. According to a quick web search the first widely used standard indentation hardness measurement was proposed by the Swedish engineer Johan August Brinell in 1900 [28]. In his test

a steel ball with standard size is pressed by a known force into the specimen surface and the hardness value is derived mathematically by measuring the diameter of indentation. In 1921, Robert L. Smith and George E. Sandland developed an alternative test at Vickers Ltd to overcome the problems of the Brinell-test, where the indenter size has to be known for calculating the hardness value and cannot be used on all specimen. They proposed the use of a indenter geometry where the hardness value is proportional to the load necessary to produce a constant sized impression [29]. To achieve this they used a square-based pyramidal shaped indenter geometry, which produces self-similar impressions independent of the size of the actual impression.

By reducing the load to a smaller value as compared to the classical tests, the hardness measurement on a micrometer and nanometer scale is possible. But with this also the deviations of the tip from the ideal shape have to be taken into account. E.S. Berkovich suggested a three-side pyramid with angles of 142.3° between the sites to obtain the same projected area to depth ratio as by using the Vickers geometry [30].

In the classical setup the hardness H is calculated as the ratio between maximal load P_{\max} and contact area A_c between indenter and specimen (cf. Equ. 4.8).

$$H = \frac{P_{\max}}{A_c} \quad (4.8)$$

In this case the contact area is ideally the projected surface of the imprint. In case of uncontrolled plastic deformation like sink-in or pile-up the actual contact area is not easy to obtain.

Because of the fixed geometry the hardness value is calculated in a quiet easy way. For the Vickers geometry the following equation holds:

$$HV = 0.1891 \cdot \frac{P_{\max}}{d^2} \quad (4.9)$$

where d in this case is the diagonal of the projected area and the factor takes into account the geometry and the change from newton to kilo pounds.

In the same way for the Berkovich geometry the following equation holds:

$$H = 1.4597 \cdot \frac{P_{\max}}{a_b^2} \quad (4.10)$$

where a_b is the length of the triangle site.

In 1992 finally Oliver and Pharr introduced a method to measure hardness and elastic modulus of specimen on a small scale [31]. Using this method the mechanical properties of the specimen are investigated by continuously recording the load and displacement of the indenter during a cycle of loading and unloading. From this so measured load-displacement data curves, quantitative values for the hardness and the elastic constants can be obtained by processing them with a theoretical model describing the elastic-plastic contact between indenter and specimen surface. In contrast to indentation techniques where the surface impression has to be imaged and measured, in this case all the information is obtained from the recorded data. Also, because of the small size and small

indentation depth, the method allows to measure the mechanical properties of thin film and small differences in structure [32].

4.3.2 Theoretical Background

For the measurement of elastic modulus and hardness the data of the unloading process is essential. Both P_{\max} and h_{\max} are obtained from the starting point of the unloading process. In this part it is assumed that only the elastically unloading is recorded and no plastic deformation is taking place. Also plastic sink-in or pile-up of the specimen near the indenter is not taken into account. But the elastic sink-in is taken into account and therefore the measured maximal depth corresponds to a sum of depth obtained by elastic and plastic deformation. So the depth over which the indenter actually is in contact with the specimen, here referred to as h_c , can be obtained by subtracting the elastic sink-in depth h_s from the measured total depth h_{\max} . This elastic sink-in has to be calculated under the assumption that the contact area sinks in in a way that it can be described by models for rigid punches of simple geometry into a flat elastic half space (for further references see once more [32]), resulting in Equ. 4.11.

$$h_s = \epsilon \frac{P_{\max}}{S} \quad (4.11)$$

In this equation $\epsilon = 0.75$ is a geometry factor obtained from the modeling and $S = \frac{dP}{dh}$ is the specimen stiffness as obtained from the slope of the elastic unloading data (cf. Fig. 4.4a).

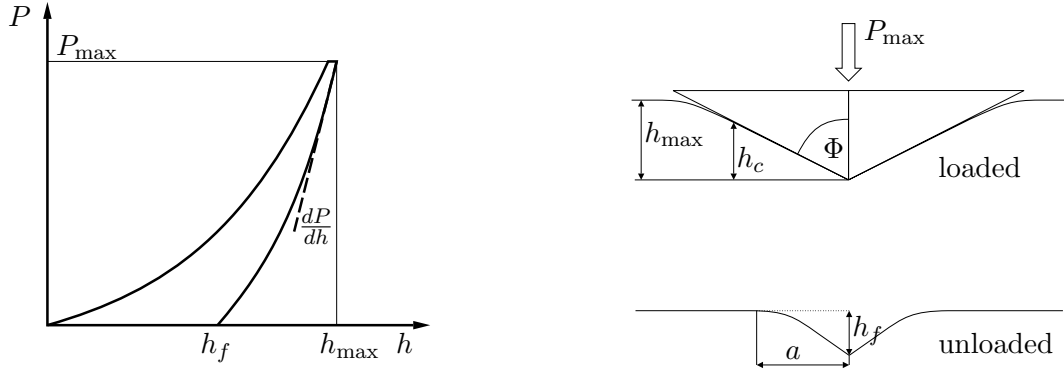
The hardness of the specimen is calculated as

$$H = \frac{P_{\max}}{A} \quad (4.12)$$

where P_{\max} is the maximal load as obtained from the load-displacement curve and A is the contact area of the indenter tip. Depending on the geometry of the tip the contact area can be calculated as a function $A = f(h_c)$ of the contact depth h_c , sometimes referred to as indenter shape function. It is very important to note here, that because of the calculation of the contact area under load the hardness value might be different as compared to a value obtained by a measurement without load.

With the so obtained values finally also the elastic modulus E of the specimen can be derived using Equ. 4.13 and Equ. 4.14. The factor β in Equ. 4.13 is a dimensionless value, which corrects for the deviation of the axial symmetry of the indenter and any other physical effect leading to a slightly deviation. It is concluded from finite element simulations that for a Berkovich tip a value of $\beta = 1.05$ is a good choice leading to a potential error of about ± 0.05 (further details once again can be found in the article of Oliver and Pharr [32]).

$$S = 2\beta \sqrt{\frac{A}{\pi}} E_{\text{eff}} \quad (4.13)$$



(a) Schematic representation of a typical dataset of the recorded load-displacement curve during a single loading and unloading cycle. From the slope of the linear part of the unloading curve the stiffness of the elastic contact is calculated. The creep is measured by holding P_{\max} constant for a time interval and record the depth change.

(b) Schematic representation of a nanoindentation in cross-section showing the surface when loaded and after unloading.

Figure 4.4: Schematic representation of the nanoindentation process

By Equ. 4.14 the E -modulus of the specimen is derived by taking into account the elastic modulus E_i and the Poisson value ν_i for the indenter tip. This is important since only E_{eff} is obtained directly from the data.

$$\frac{1}{E_{\text{eff}}} = \frac{1 - \nu^2}{E} + \frac{1 - \nu_i^2}{E_i} \quad (4.14)$$

4.3.3 Possible Errors and Their Compensation

By reducing the indenter size, the systematic errors of the measurement gain in significance and are not always negligible anymore. One of this errors is the zero approach of the tip. Before measuring the software approaches the tip slowly to the surface, until a significant load can be measured. Because of the relative precision of the instrument, this will lead to a distribution of the zero point around the real one. This is why the zero point is found by fitting a curve to the loading data. For this the first unreliable measurement points are neglected and then fitted with the following function:

$$P(h) = c \cdot (h - h_0)^{1.5} \quad (4.15)$$

where c is the fitting parameter.

The next possible error is the roundness of the tip, which has to be corrected for nano hardness measurements. To correct for this, the exact surface function of the tip has to be known, which

can be achieved or by measurement with for example a AFM or indirect by calibrating with a reference specimen, from which the Young's modulus is well known.

Another possible error is thermal drift and creeping. Thermal drift is due to small thermal expansions caused by small temperature fluctuations, especially manifesting itself when there is a temperature difference between tip and specimen. Creeping is caused by the velocity dependence of the plastic deformation, which means over time it comes to a relaxation in the material. Both errors can be corrected by correction curves obtained by isochronal recording of the indentation depth under a fixed load (cf. Fig. 4.4a).

All this corrections are automatically carried out by the instrument software, reducing the complexity of the process for the user.

4.4 Differential Scanning Calorimetry

4.4.1 Introduction

By the term differential scanning calorimeter or in short form DSC an instrument to measure heat flow is meant. This is done by measuring the heat needed to keep the specimen at the same temperature as a reference sample as a function of time or temperature. There exist two different types of DSCs:

- the heat flux DSC
- the power compensation DSC

Since all experiments were carried out on a power compensation DSC (Perkin Elmers), only this type will be presented in the following. For further details one can see the textbook "Differential Scanning Calorimetry" by Höhne, Hemminger and Flammersheim [33] for further details. Also most of the information in the following are obtained from that book.

4.4.2 Function of a Power Compensated DSC

The power compensated DSC measure a heat flow by compensation for the heat with electrical energy, increasing or decreasing the power of an electrical heat source. The instrument in practice consists of two furnaces made of the same alloy, containing each a temperature sensor and a heating resistor. Both furnaces are thermally decoupled and positioned in an aluminum block of constant temperature. During heating a temperature control circuit applies power to both furnaces to heat them up with the set heating rate. If the furnaces are totally thermally symmetric, the temperature will change the same way in the two furnaces. By introducing the specimen we create an asymmetry in this temperature change which is measured as the difference to the reference furnace and compensated by a second control circuit applying more or less power to

an independent heat source. The power for compensation is proportional to the temperature difference because of the proportional controller, which integrated over time is proportional to the heat Q needed to maintain the samples temperature equal to the reference, and therefore given by the thermodynamical process in the specimen. The heat flow rate is also proportional to the temperature difference, the proportional factor is obtained by calibration of the instrument [33]. The heat flow rate of the thermodynamical process in the specimen is not exactly proportional to the heat flow rate of the furnace because there is a conduction way between them and therefore the measured signal is distorted by a time constant. Also the power compensation never completely eliminates the temperature difference, leading to an error in the measurement.

The specimen is placed in the designated crucible inside the furnace and the reference sample is placed in the other one, if a reference is used. It is also possible to use the DSC without reference specimen, which introduces an asymmetry with heat losses which can not be compensated.

To obtain the real heat flow rate into the specimen a baseline subtraction has to be performed. This baseline comes from the asymmetry of the instrument and can be obtained by running a second measurement with the same parameters but without the specimen. By subtracting the so obtained curve the instruments influence to the obtained signal can be minimized.

4.4.3 Thermodynamics

The difference in enthalpy ΔH is the value describing the phase transition at constant temperature T . In the DSC the heat Q needed for the phase transition is measured by integration over time of the power compensation. From the first law of thermodynamics and the total differential of the free enthalpy follows [33]:

$$dQ_m = \left[\left(\frac{\partial H}{\partial p} \right) - V \right]_{T,\xi} dp + \left(\frac{\partial H}{\partial T} \right)_{p,\xi} dT + \left(\frac{\partial H}{\partial \xi} \right)_{p,T} d\xi - \sum_i dE_i \quad (4.16)$$

In Equ. 4.16 the first term can be neglected in most cases since $dp = 0$, the second term corresponds to the heat capacity $C_{p,\xi}(T)$. The third term is the interesting one since it is the isothermal and isobaric enthalpy change due to phase transition, mixing effects or a reaction. This is equal to the measured dQ_m if the $\sum_i dE_i = 0$, which is a change in energy by surface creation as by wetting. Derivation of Equ. 4.16 in time using the simplifications described before leads to the Equ. 4.17 forming the basis for kinetic evaluation of DSC curves.

$$\frac{dQ_m}{dt} = C_{p,\xi}(T) \frac{dT}{dt} + \left(\frac{\partial H}{\partial \xi} \right)_{p,T} \frac{d\xi}{dt} \quad (4.17)$$



(a) Instrumental setup of the Perkin Elmer DSC 8500 with liquid nitrogen tank for the cooling and nitrogen as purge gas.



(b) Crucibles inside the furnaces of the Perkin Elmer DSC 8500, the left is the specimen chamber, the right one the reference chamber.

Figure 4.5: The pictures show the Perkin Elmer DSC 8500 used for the thermal treatment of the specimen.

4.5 Listing of Instruments

The following instruments were used for the specimen preparation and analysis:

- TEM studies are performed using a Siemens CM200 operating at 200 kV.
- The HRTEM investigations are done using a CM30 operating at 290 kV.
- STEM analysis are carried out using a Nion UltraSTEM 100 operating at 100 kV and a FEI Titan operating at 300 kV.
- The SEM measurements are done on a Zeiss Supra 55VP operating at 20 kV.
- For the TEM specimen preparation a Struers Tenupol-3 twin jet electropolishing machine is used.
- For the DSC measurements a Perkin Elmer DSC 8500 is used.
- Nanoindentation imprint measurements are carried out using the ASMEC Unat with QCSM module for depth dependent measurements.
- For HPT deformations a High Pressure Torsion press type WAK-01 Mark 1 is used.

5 Experimental Results and Discussion

5.1 SEM Analysis of the As Cast Alloy

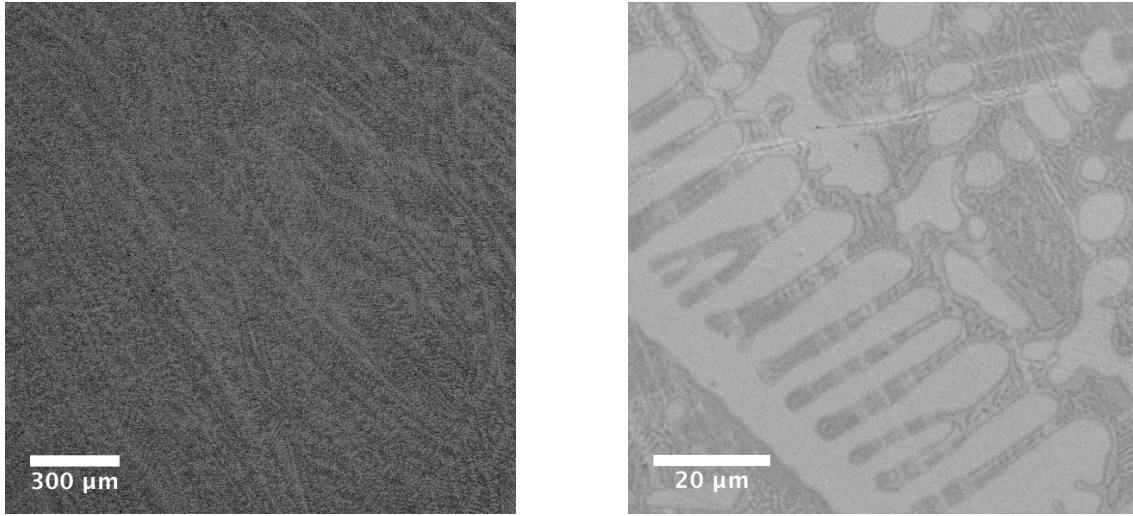
5.1.1 State After the Melting and Mixing

A very first SEM analysis using the Zeiss Supra 55VP is carried out right after the melting and mixing of the alloy in the induction furnace. Already with the naked eye one can clearly see some surface contamination, manifesting itself by a shining red-brown color.

The colored surface indicates that the thickness of this contaminated layer may only be thin, leading to an interference phenomena of light, manifesting itself by this for the alloy untypical color (Co_3Ti has normally a silver metallic shining surface). The SEM analysis is carried out without previous treatment of the specimen, right on the surface after cooling down. Data about relative concentrations are obtained by EDX, confirming the surface contamination by oxidation, showing a relative concentration of oxygen of about 16at.%. This results in a superficial composition variation of the alloy between 23at.% to 36at.% of Ti and 44at.% to 77at.% of Co, depending on the region. Because of the very uneven surface, these measured values are only of qualitative character, knowing that the surface roughness may affect the quantitative values.

To make sure that the nominal concentration (23at.%Ti-77at.%Co) corresponds to the actual concentration of the alloy, one of the three metal slugs is cut into two halves and one of the cross-section surfaces is polished for further SEM analysis.

SEM images showing the polished cross-section are presented in Fig. 5.1, showing a huge number of dendrites, which all grew in a preferred direction out of the molten metal. The higher magnification image of Fig. 5.1 shows an even finer phase separation in the matrix, in between the dendrites. This indicates that this phase separation in the melt occurs after the formation of the large scale dendrites. The formation of dendrites results from the low nucleation rate, indicating a low concentration of nucleation centers (which normally are impurities), meaning the contamination during the melting was reduced to a minimum as wished. The formation of dendrites is caused by a temperature and a concentration gradient in the undercooled melt and in front of the solid-liquid interface. The first is arising from the latent heat obtained by the crystallization process, the second by the formation of the phase with a concentration different to that of the liquid. Normally the nucleation starts at impurities because of the lower surface to volume ratio of



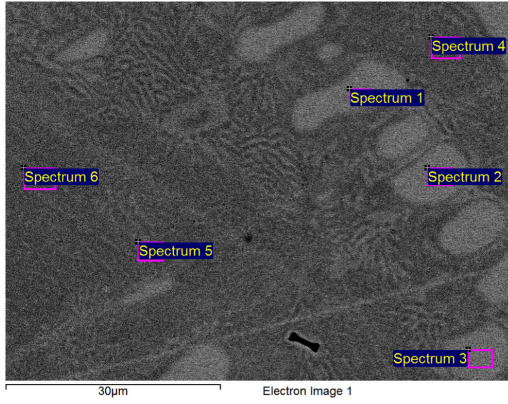
(a) Overview SEM image of a large area of the slug cross-section.

(b) More detailed view of the dendrites which have formed during the cooling.

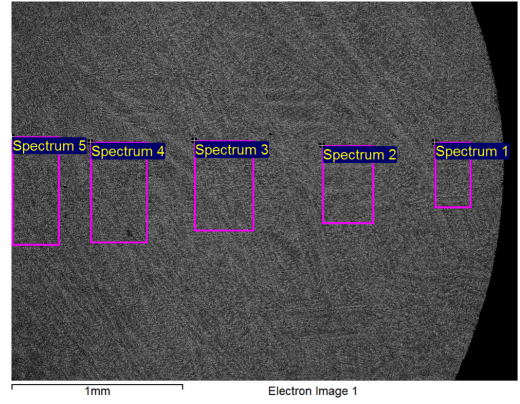
Figure 5.1: SEM images of the “as molten” specimen cross-section taking with the backscattered detector. The images reveal that there are two phases present, one formed by dendritic growth out of the melt, which indicates low nucleation and therefore a undercooling of the melt.

the already present particles as compared to homogeneous nucleation and therefore energy gain by growth. For small nuclei the surface energy needed to form the nucleus is higher than the energy gain by the crystallization. Only if the undercooling of the melt is high enough, the crystalline phase is stable enough to overcome this barrier. In other words the critical radius for nucleation is a function of the temperature. In high purity alloys the highest impurity is the crucible surface, acting therefore as nucleation center.

The data obtained by EDX-analysis are presented in Tab. 5.1 and Tab. 5.2. The corresponding figures with the marked rectangular regions indicating the spectra recording area, are shown in Fig. 5.2a and Fig. 5.2b. The regions 1, 2 and 3 in Fig. 5.2a show a bright contrast whereas the other three regions show a darker contrast. Because the images are obtained by using the backscattered detector, the Co-richer phase are expected to have a brighter contrast. One could expect this, since the backscattered detector collects all the by the specimen backscattered electrons, which should be more in regions with higher mean Z-value, and therefore the Co-rich regions. In this images this is clearly not the case. According to Tab. 5.1 the brighter regions show a Ti concentration of about 29at.% and 71at.% Co, whereas the darker regions correspond with about 22at.% Ti and 78at.% Co to the regions with higher mean Z-value. This shows clearly how sensitive the backscattering of electrons is to orientation changes which influence therefore the contrast in a contra-intuitive way.



(a) Measuring the concentration in the two different phases.



(b) Measuring the overall concentration as a radial function.

Figure 5.2: EDX measurements of the alloyed Co_3Ti in the cross-section of a slug.

Spectrum	at.%Ti	at.%Co
1	28.70	71.30
2	29.14	70.86
3	28.71	71.29
4	21.62	78.38
5	21.62	78.38
6	21.67	78.33
mean	25.24	74.76
std. dev.	3.95	3.95
max.	29.14	78.38
min.	21.62	70.86

Table 5.1: EDX results of the 6 different regions corresponding to the rectangular areas marked in Fig. 5.2a.

Spectrum	at.%Ti	at.%Co
1	24.26	75.74
2	24.48	75.52
3	24.15	75.85
4	24.33	75.67
5	23.82	76.18
mean	24.21	75.79
std. dev.	0.25	0.25
max.	24.48	76.18
min.	23.82	75.52

Table 5.2: EDX results of the 5 different regions corresponding to the rectangular areas marked in Fig. 5.2b.

The two phases have concentrations of about 29at.%Ti-71at.%Co and 22at.%Ti-78at.%Co with a mean of 25.24at.%Ti-74.76at.%Co which is quite significantly off from the nominal concentration. To check the overall concentration, spectra of larger regions on the mm-scale were recorded, looking at the same time for variations in radial direction from the center. This is shown in Fig. 5.2b and Tab. 5.2. The quantification of the spectra confirmed indeed the slightly higher Ti concentration of about 24at.% as compared to the nominal concentration of 23at.%. This can be explained by the concentration variation between the three different sets used for alloying, which because of the finite size of the initial metal pieces are not exactly of the right composition. By casting all three together, the nominal concentration should be achieved. This is verified by analyzing the homogenized alloy later.

There is no significant variation of the composition over the radial direction, indicating that the metals mixed very well during the melting in the induction furnace. Also no lost of material by evaporation is measured, which means a high purity alloy of the desired nominal concentration is obtained. The strong oxidation of the surface can not be avoided and this surface is removed by mechanical polishing before the further processing of the alloy.

5.1.2 State of the Alloy After the Casting Into Rod-Form

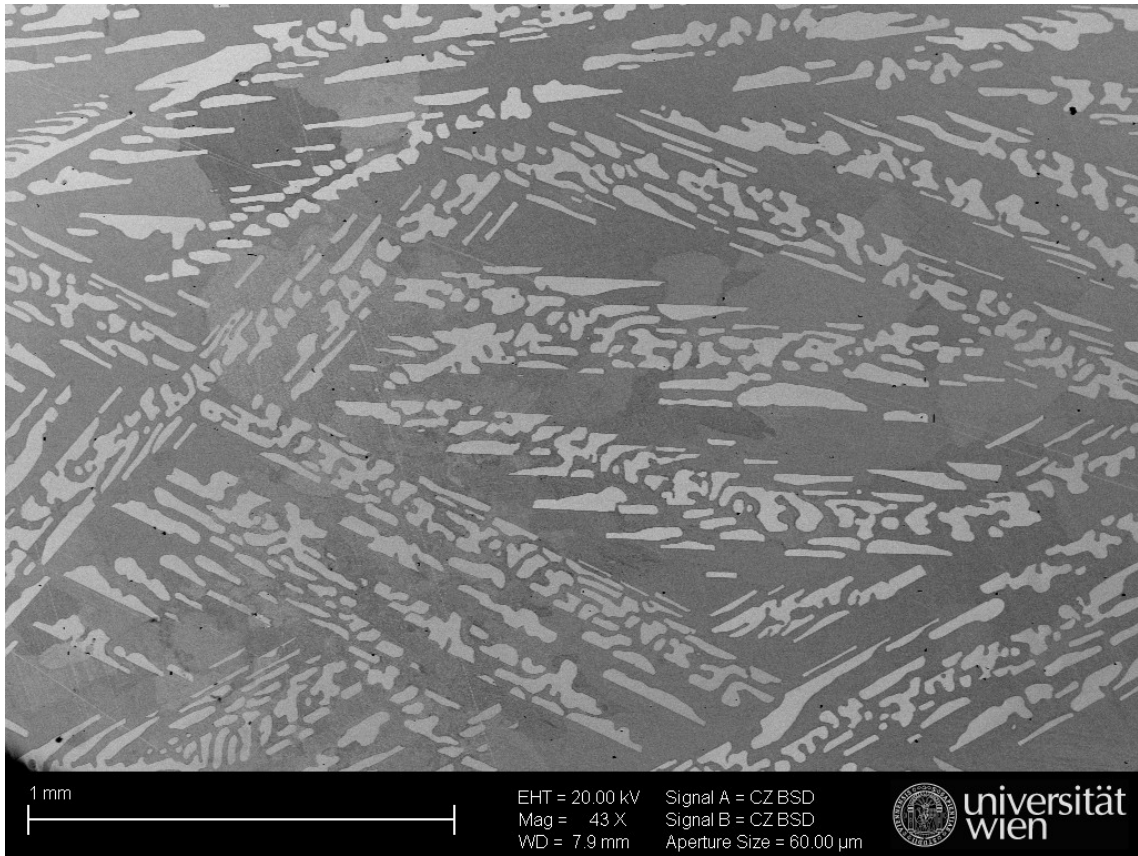
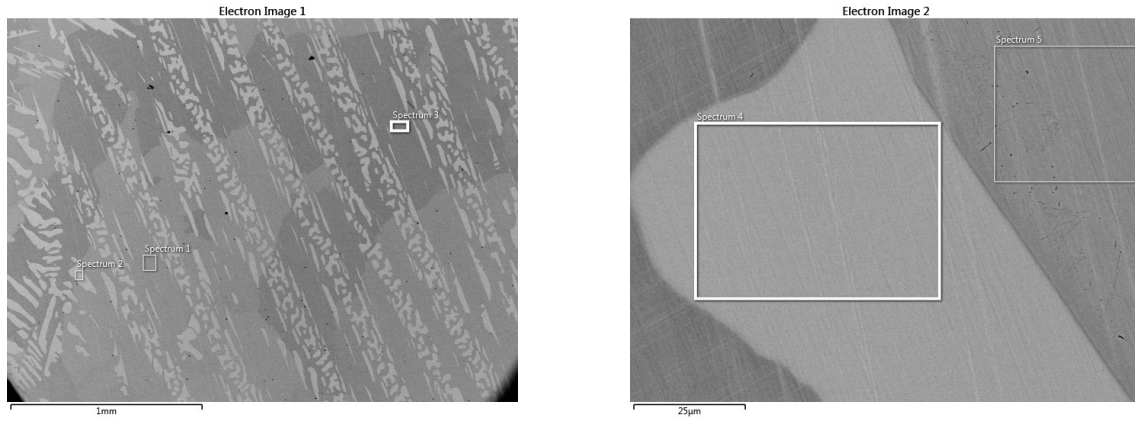


Figure 5.3: Phases present in the alloy after the rod production as seen on the surface of a cut normal to the cylinder axis.

After the casting of the alloy into the rod formed crucible a further SEM analysis is carried out. At this stage all the slugs are already molten together in the crystal growth furnace, so the overall concentration should correspond to the nominal concentration. For the analysis a piece of the upper part is cut from the rod by spark erosion and polished for SEM analysis. In Fig. 5.3 a backscattered detector image of the specimen is shown. Again there are two phases present in the material, this time the phases are larger as compared to the previous state. This is expected, since the crystal growth furnace with a sharp temperature gradient is moved very slowly along the specimen, allowing the melt to cool down in a very controlled way. This is also the reason why in the darker phase clearly large grains with sizes up to the mm-range can be identified. Again there is a strong directional growth in different directions, leading to a very nice pattern in the figures. Identification of the two phases by EDX-measurements (cf. Fig. 5.4) are performed once again. The analysis shows that with about 71at.%Co-28at.%Ti obtained in spectrum 2 and 4 and 78at.%Co-22at.%Ti obtained from spectrum 1, 3 and 5 (cf. Tab. 5.3), the concentrations in the different



(a) In the image the rectangular regions corresponding to three of the 5 spectra are shown, 4 and 5 can be found in Fig. 5.4b.

(b) Higher magnification of an area with two phases on which EDX analysis were performed. The spectra of the two regions marked with the rectangles were measured.

Figure 5.4: SEM image of Co_3Ti - Phases in the material before the annealing are characterized by EDX. The quantitative results are given in Tab. 5.3.

Spectrum	Ti	Co
1	22.09	77.91
2	28.76	71.24
3	22.29	77.71
4	28.45	71.55
5	21.89	78.11
mean	24.70	75.30
std. dev.	3.57	3.57

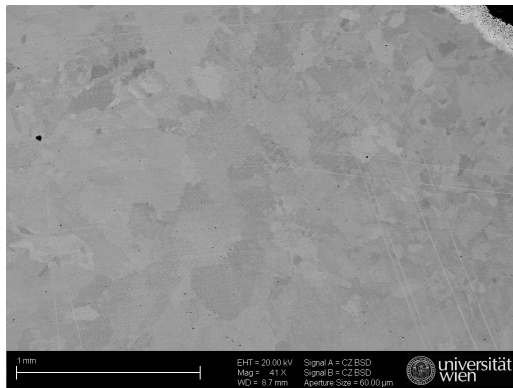
Table 5.3: EDX Concentration measurements of the as cast specimen showing the atomic percent of elements found by the software.

phases are almost the same as before the casting into the rod formed crucible. This means the brighter areas in Fig. 5.3 correspond to a Ti rich phase whereas the darker regions are Co rich areas, showing slight contrast variations because of different orientations of the grains in this polycrystalline phase. This reveals the fact that the intensity is a function of both, concentration and orientation.

5.1.3 State of the Alloy After Homogenization

A final SEM analysis is also done on the annealed specimen. The alloy gets annealed for about 100 h at 950 °C as whole rod to obtain a homogeneous material with only the L_{12} phase. For the analysis the round tip of the rod is used by cutting it off and polishing it for the SEM imaging. The image shows that the material is indeed homogeneous, only one phase is present. The grain size shows a variation with the distance to the rim, probably because of the temperature gradient during casting of the alloy, allowing the regions in the center to form larger grains than at the rim. The EDX data Tab. 5.4, obtained from three large grains, one of the center, one at the rim and one in between, show that now the specimen concentration and the nominal concentration are the same over the specimen.

This state of the alloy is the initial state for all further HPT deformation experiments.



(a) Backscattered electron image - After the annealing at 950 °C for 97 h the material is single phase L_{12} . The differences in contrast are caused by grains of different orientation.



(b) Secondary electron detector SEM image of Co_3Ti - The regions show the areas from which the spectra are recorded.

Figure 5.5: SEM image of Co_3Ti - After annealing only one phase is present in the alloy.

Spectrum	Ti	Co
1	22.96	77.04
2	23.31	76.69
3	23.52	76.48
mean	23.26	76.73
std. dev.	0.28	0.28

Table 5.4: Concentration measurements of the as annealed specimen show a single phase with the desired composition. The spectra correspond to the marked regions in Fig. 5.5b.

5.2 High Pressure Torsion Deformation

The goal of the HPT deformation is to obtain a solid state transition from the $L1_2$ ordered crystalline phase to the metastable amorphous phase. Therefore the annealed specimens have to be shaped in a geometry needed for the deformation process. The HPT deformation as described in 3.6 requires a disc shaped geometry of the specimen, which is then placed between the two anvils. The two used anvils are made of a high performance stainless steel which were processed mechanically in a turning lathe to obtain smooth cavities with a depth of 0.12 mm and a diameter of 8 mm. To avoid touching of the anvils when load is applied and therefore the specimen thickness is reduced, a thickness of 0.55 mm is found to be best for the discs. In a first step the discs are cut from the rod-formed and homogenized specimen by spark erosion. For this cutting process the rod is glued onto a piece of metal using a mixture of glue with conductive silver and on the "Charmilles" spark erosion the following settings are chosen:

- Microfin
- 1 μF additional capacitor
- 1 mm forward steps between each cut to obtain a suitable disc thickness

By this specimen with thicknesses of 0.6 mm to 0.8 mm are obtained. These discs are then glued in the same manner onto a metal piece as holder and 8 mm discs are punched out by using a tube shaped tool in the spark erosion machine. The additional 1 μF capacitor is not used during punching. To get to the final thickness and to exclude the influence on the HPT deformation by the damaged layers which have formed on the surface by spark erosion cutting, the samples are finally mechanically polished. For this, a polishing machine using papers with P320 roughness is used. The polishing is done using a holder to obtain even and parallel sample surfaces and the disc thickness of 0.55 mm.

Before putting the samples in the machine, the inner surface of the anvils and the surface of the sample are sandblasted to avoid slipping of the sample during deformation. To avoid heating up

of the specimen during the high straining deformation process, the rotation speed is set to only 1 turn in 5 min. Samples are deformed with **20 turns at 4 GPa**, **80 turns at 4 GPa** and **20 turns at 8 GPa** at room temperature. In addition also a deformation under liquid nitrogen is carried out to study the performance of the phase transition with respect to the temperature.

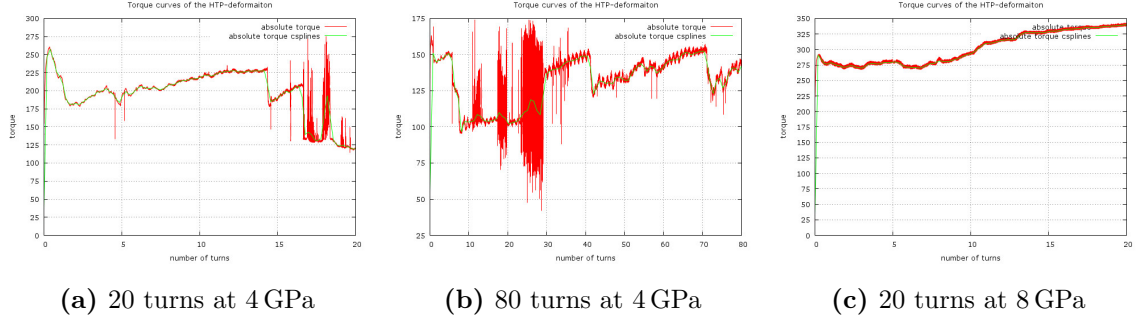


Figure 5.6: The graphs show torque curves as a function of turns recorded during HPT deformation of the specimen with different settings. During the deformations with the smaller pressure of 4 GPa, the torque curve shows many instabilities which indicate possible slip and cracking of the sample. The green curves overlaid over the red ones are smoothed data sets to better see the trends.

During the deformation process, the torque is recorded as a function of time. These curves are shown in Fig. 5.6a for the 20 turns 4 GPa, Fig. 5.6b for the 80 turns 4 GPa and Fig. 5.6c for the 20 turns 8 GPa deformation. The first data set (20 turns, 4 GPa) shows clearly a jump from slightly over 225 N m down to slightly over 175 N m, appearing at a time when a loud clicking sound could be heard from the machine. Also during the second deformation (cf. Fig. 5.6b) some clicks are heard, and the recorded torque curve shows extreme variations in magnitude. These clicks indicate that the anvils may have been touching and were welded together by the high pressure, releasing themselves again producing the clicking sound. Interesting is also the fact, that small variations in magnitude occur over nearly all the data set, showing a frequency corresponding to the number of revolutions per minute of the deformation. This indicates a misalignment of the anvils between each other. The third parameter set with 8 GPa (cf. Fig. 5.6c) on the other hand shows a quite smooth torque behavior as compared to the two previous one. The magnitude of torque rises from an initial value of about 275 N m up to over 325 N m after the 20 revolutions, indicating work hardening of the cold worked specimen. By looking at the deformation curves and taking in account the clicks, slipping of the sample can not be excluded and therefore not the full degree of shear strain may have been introduced. On the other hand, the deformation of the sample with the 8 GPa seemed to have gone very well, since the curve is very smooth and no clicking was heard. After the deformation the specimen are ferromagnetic, already indicating the disordering of the initially ordered structure.

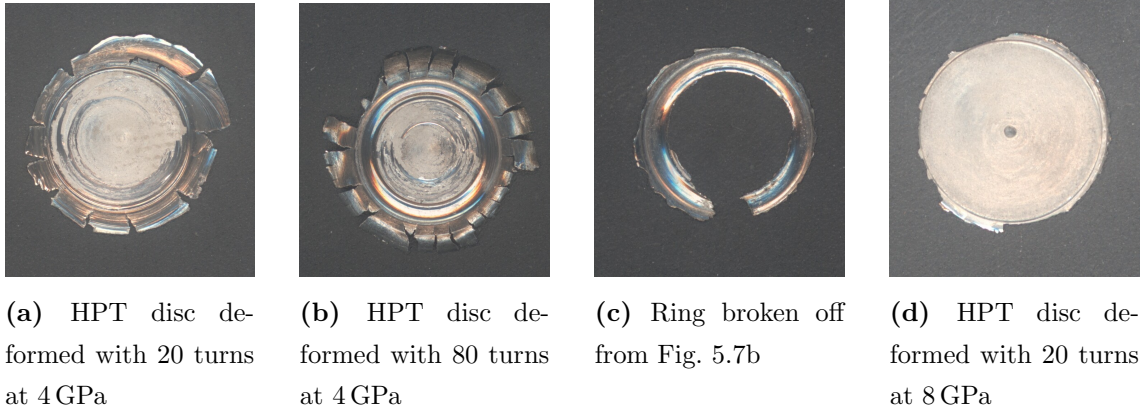


Figure 5.7: Scans of the as deformed HPT discs

In Fig. 5.7 the scans of the HPT discs deformed with 20 and 80 turns at 4 GPa and 20 turns at 8 GPa are presented. They show the unavoidable plastic material flow out of the region in-between the anvils during the deformation. The disc in Fig. 5.7d doesn't show this ring of flown material in the figure, because it broke off during the removal of the specimen from the anvils. Fig. 5.7b shows the specimen deformed with 80 turns at 4 GPa and if you look carefully, you might see that a ring piece of material is missing at the outer rim of the specimen. Exactly this missing piece is shown in Fig. 5.7c. This ring is broken off from the specimen during the unloading process, indicating the high inner stresses in the alloy after the deformation. It seems that this stresses have build up in a region with a high density of shear bands, as deduced from the contrasts in the corresponding SEM image (cf. Fig. 5.13).

In the following a SEM backscattered images of the cross-sections of all 4 specimen are presented. To each cross-section two images with interesting features are added.

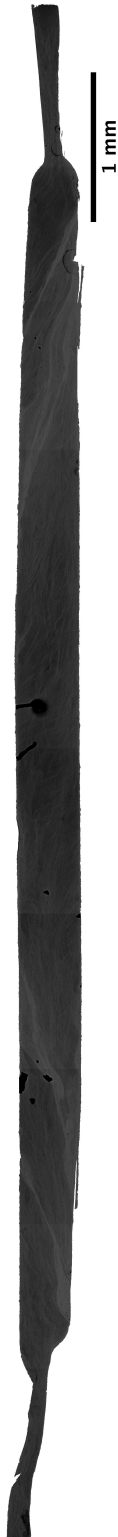


Figure 5.8: Disc deformed by 20 turns at 4 GPa at RT.

In Fig. 5.8 a cross section of the HPT disc deformed by 20 turns at 4 GPa is shown. The backscattered images shows the presence of a high number of shear bands, but still mostly crystalline volume. This is also seen in Fig. 5.9 where the bright lines correspond to the amorphous bands. Fig. 5.10 shows a region near the center, where the strain rate is lower and the amorphous bands in a earlier stage of deformation. They are much finer and show a preferred orientation.

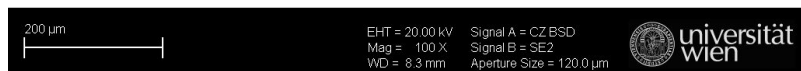
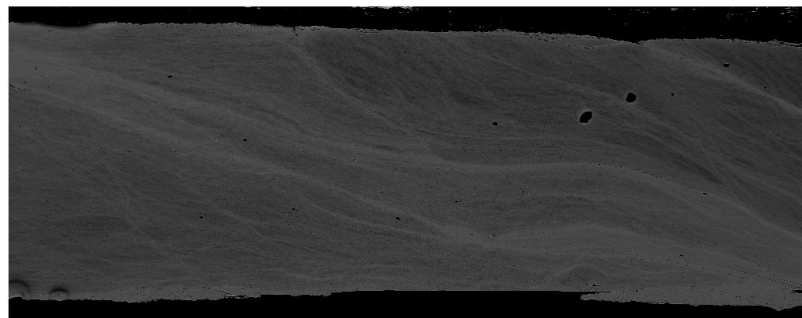


Figure 5.9: SEM backscattered image showing the retained crystalline phase intersected by broader and finer amorphous bands.

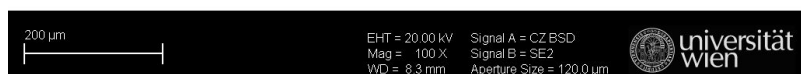
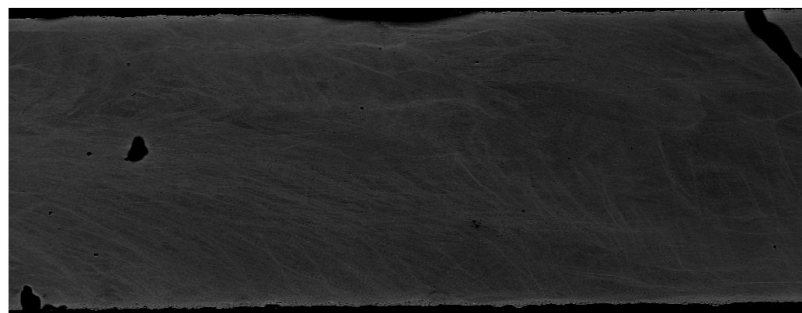


Figure 5.10: The position near the center of the disk shows many fine bands with a preferred orientation.



In Fig. 5.11 a cross section of the HPT disc deformed by 80 turns at 4 GPa is shown. In addition to the broader shear bands similar to Fig. 5.8, now also cracks running near the interface of amorphous bands and the crystalline phase can be found as indicated by the arrows in Fig. 5.12. This is an indication for the high inner tensions, leading to crack formation during the unloading after the deformation. In Fig. 5.13 the interface to the broken off ring is shown. The arrow points at a location where an extended rest of the accumulated shear bands can be seen.

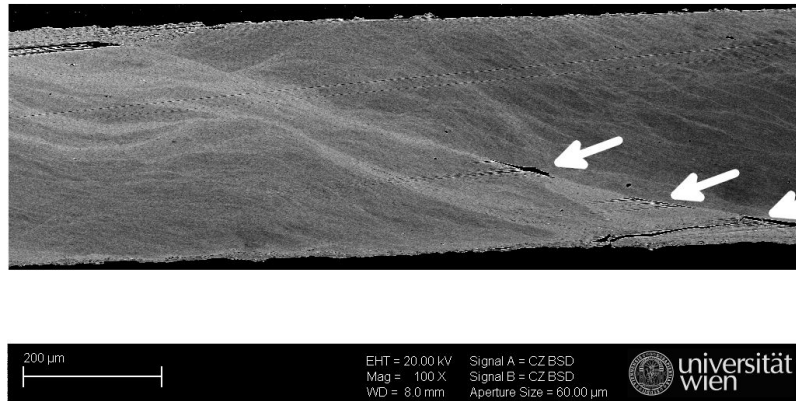


Figure 5.12: Cracks are forming near the interface of the broad amorphous band and the crystalline phase.

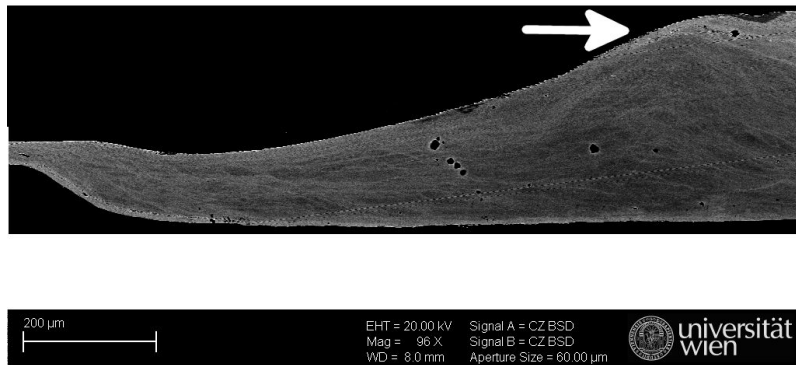


Figure 5.13: The interface region from which the ring broke of after unloading in detail. The arrow marks an amorphous part of a shear bands which might have caused the inner tensions leading to crack formation.

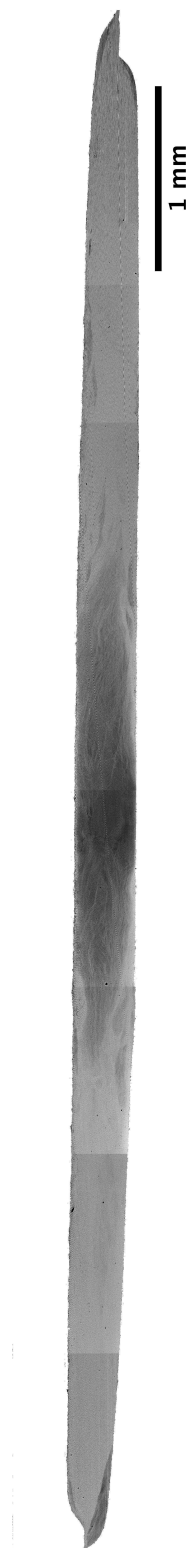


Figure 5.14:
Deformed by 20
turns at 8 GPa at RT.

The SEM cross-section shown in Fig. 5.14 was deformed by 20 turns at 8 GPa. In contrast to the previous discs, this one showed a large homogeneous amorphous region in the high strained specimen areas. This is also seen in Fig. 5.15 which is a backscattered electron image from such an amorphous region. Fig. 5.16 shows an area near the center of the disc and as expected the crystalline volume gets higher with decreasing distance from the center.

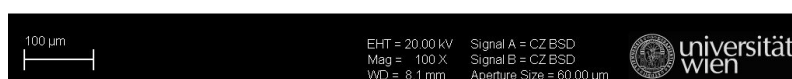
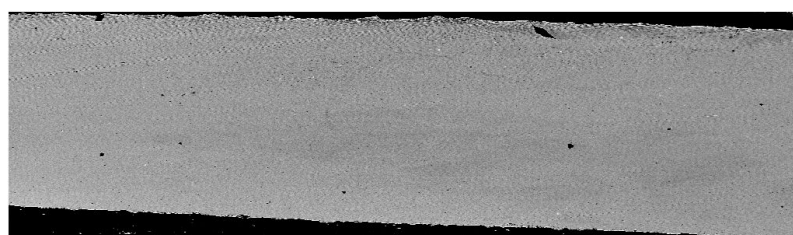


Figure 5.15: The outer regions of the specimen show a homogeneous amorphous area over the whole specimen thickness.

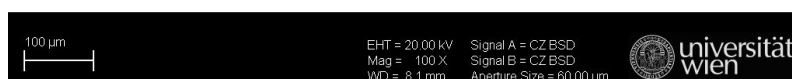
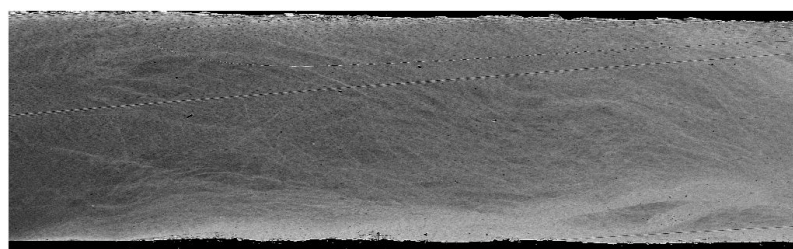


Figure 5.16: In the central region the volume of the crystalline phase increases as expected.

Finally in Fig. 5.17 the disc deformed by 20 turns at 8 GPa at N_2 temperature is shown. Fig. 5.18 shows that there is an extended amorphous band region marked by the arrows. But the amorphous band is limited to the top and the bottom surface. Between those layers there is still mostly the retained crystalline phase. Fig. 5.19 shows the central region of the disc cross-section. The contrasts reveal a fully crystalline material with many very fine lines intersecting the areas.



Figure 5.17:
Deformed by 20
turns at 8 GPa at N_2
temperature.

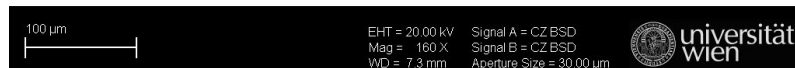
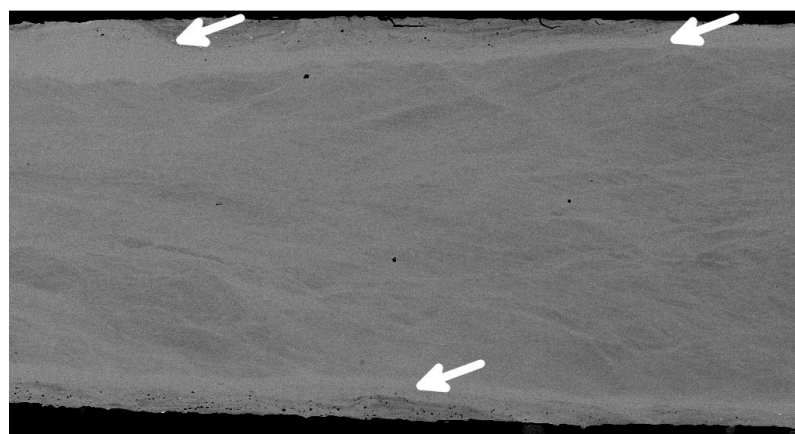


Figure 5.18: In the high strained regions the specimen deformed under N_2 temperature shows only at the top and bottom surface an extended amorphous band. Between them the specimen is still mostly crystalline.

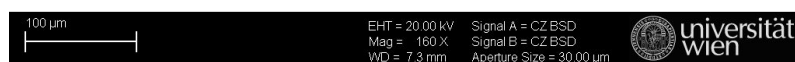
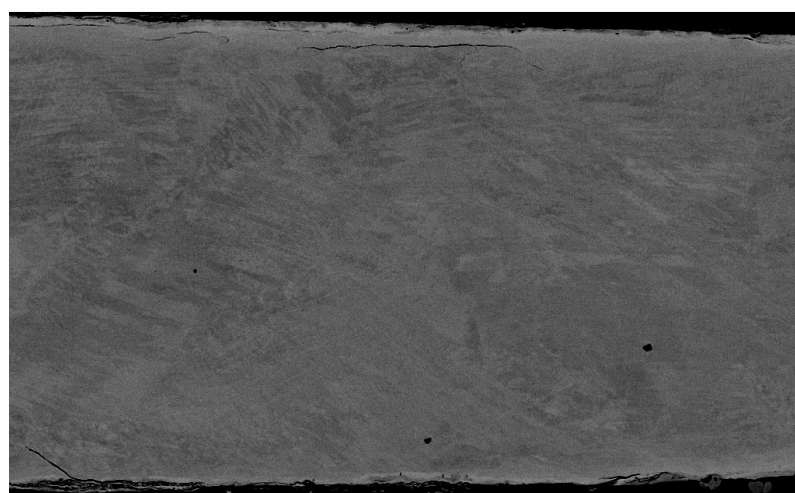


Figure 5.19: The central region of the specimen is still crystalline with many line lines intersection the retained phase.

5.3 TEM of the Specimen Deformed With 4 GPa

Already in the SEM images (cf. Fig. 5.8-Fig. 5.19) it could be seen that the specimen didn't deform homogeneously since bands of different contrast could be observed. The goal of the TEM investigations is to achieve information about the local structure of the different samples.

After TEM preparation the specimen are put into a holder and transferred into the microscope. After tuning the TEM to 200kV and heating of the filament, first adjustments to correct for aberrations and good quality imaging conditions are performed. The bright-field and dark-field diffraction contrast images are obtained by selecting the primary beam or a diffracted beam with the objective aperture.

5.3.1 20 Turns at 4 GPa

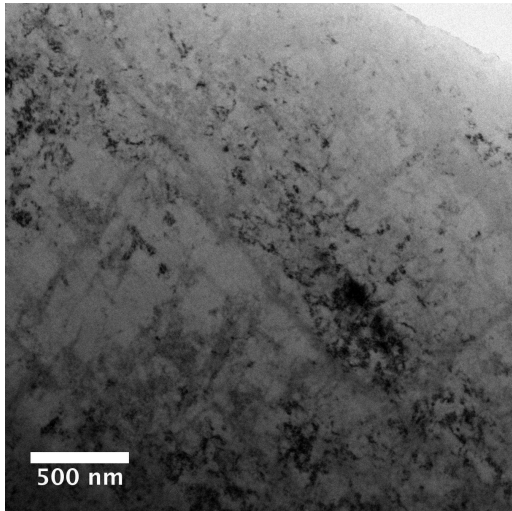
Fig. 5.20 shows TEM images of the specimen deformed with 20 turns at 4 GPa. Most of the areas are crystalline and are sometimes separated by bands of amorphous material. These can be revealed especially by dark-field images, using objective apertures at special positions in reciprocal space. Fig. 5.20c shows the corresponding diffraction pattern with intense ring segments caused by the crystalline regions and a faint broad ring due to some amorphous regions. The position of the objective aperture used for the dark-field image is indicated. The dark-field image (cf. Fig. 5.20d) shows some very bright crystals oriented in Bragg condition for the reflection selected to create the image and mainly gray bands. Due to the position of the objective aperture the latter are confirmed as amorphous and therefore are diffuse scattering areas. The amorphous bands have formed in parallel lines between the crystalline regions, which themselves are intersected by bands normal to them.

5.3.2 80 Turns at 4 GPa

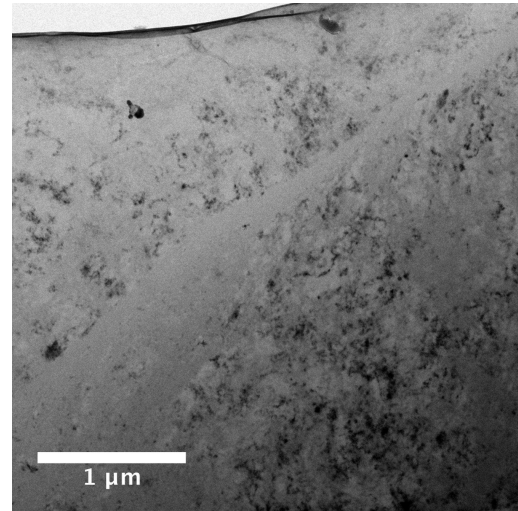
The specimen deformed with 80 turns at 4 GPa shows a similar state as the specimen deformed with 20 turns at 4 GPa. The specimen is crystalline over nearly all the investigated volume, only a few amorphous bands intersect the polycrystalline phase as it's seen in Fig. 5.21a. The diffraction pattern from the same area shows a few intense ring segments corresponding to the Co_3Ti phase. The absence of superlattice reflections in diffraction patterns of Co_3Ti cannot be used directly to clarify the state of chemical order, since their intensity is only below 5% even in the fully ordered state [34].

The diffraction spots tend to form rings around the primary beam, since the investigated material is polycrystalline. The rings are present in the form of segments because of deformation induced texture caused by similar orientations of individual grains.

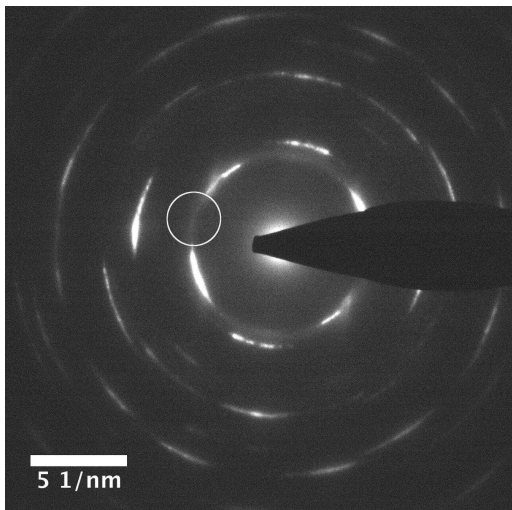
From the bright-field image no direct measurement of the grain size is possible, since the grain boundaries are not clearly defined and there are a lot of contrasts caused by strain in the image.



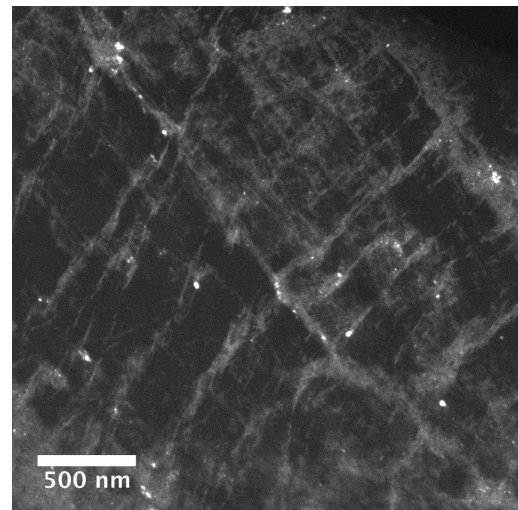
(a) Bright-field micrograph near the hole of the Co_3Ti TEM foil.



(b) Bright-field micrograph showing an amorphous band intersecting the crystalline region.

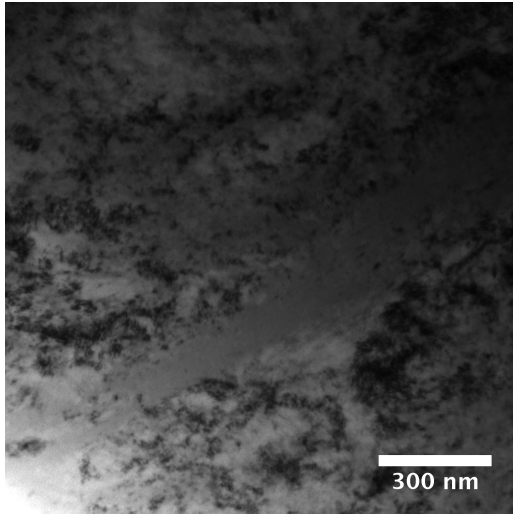


(c) Diffraction pattern of the region from Fig. 5.20a with a circle indicating the objective aperture position used for obtaining the dark-field image in Fig. 5.20d

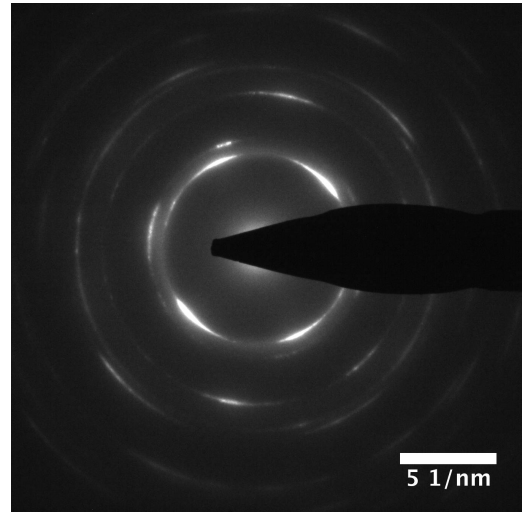


(d) Dark-field micrograph corresponding to Fig. 5.20a, obtained using the aperture in Fig. 5.20c.

Figure 5.20: TEM bright-field and dark-field micrographs of Co_3Ti deformed with 20 turns at 4 GPa. In the dark-field image high intensity with a bright contrast is observed from the few grains in Bragg condition, whereas the dark areas corresponds to grains which are not in Bragg condition. The medium contrast is produced by the diffuse scattering amorphous areas.



(a) Bright-field micrograph near the hole of the Co_3Ti sample shows the presence of an amorphous band.



(b) Diffraction pattern corresponding to the region shown in Fig. 5.21a

Figure 5.21: Co_3Ti alloy deformed with 80 turns at 4 GPa by the method of HPT.

Fig. 5.22 shows the radial integrated intensity profile of the diffraction pattern shown in Fig. 5.21b. A fit of the peaks using PASAD [37] only gave a good match when raising the background by a broad peak corresponding to the amorphous intensity ring.

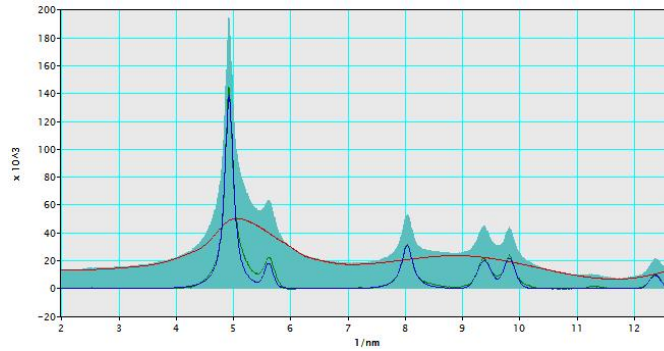


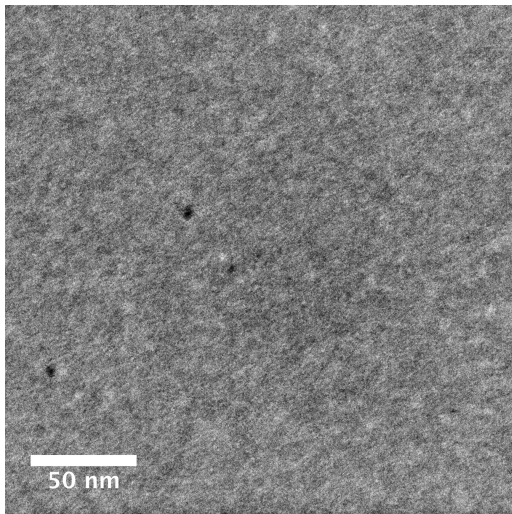
Figure 5.22: Radial integrated profile of the diffraction pattern shown in Fig. 5.21b. The peaks were fitted using Voigt functions. Only by raising the background to a level corresponding to the amorphous Co_3Ti intensity a good fit could be obtained.

5.4 TEM of the Specimen Deformed With 8 GPa

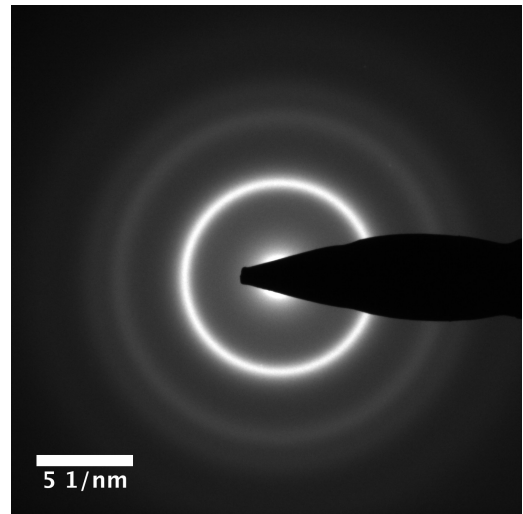
In contrast to the HPT deformation at the lower pressure of 4 GPa the deformation of the specimen with 8 GPa show clearly the amorphization of a larger volume of the alloy in the high strain regions at the radial outer ring of the HPT specimen. Since later investigations show that the amorphous phase has a lower hardness as the highly deformed crystalline one, it is interesting to see that a quite large volume fraction of the specimen has become amorphous, showing a homogeneous structure. By the accumulation and intersection of the shear bands the amorphous volume fraction gets higher until mostly all volume is amorphous. How the shear bands evolve and propagate is not fully understood yet.

5.4.1 20 Turns at 8 GPa

In Fig. 5.23 TEM micrographs of the specimen deformed with 20 turns at 8 GPa are shown. The TEM specimen are punched out of the outer region of the HPT disc shown in Fig. 5.14. The bright-field image (cf. Fig. 5.23a) of the sample taken at high magnification shows homogeneous contrast with only small intensity variations over the whole specimen area. Some regions of the specimen (cf. Fig. 5.30) show small crystals with sizes up to 50 nm. These crystals are TiO_2 particles formed during the sample preparation. The diffraction pattern of the sample (cf. Fig. 5.23b) shows broad rings characteristic for a structurally disordered (amorphous) material. The specimen is clearly ferromagnetic, directly seen in the microscope by the aberrations introduced by the additional magnetic field. The magnetic property indicates already the chemical disordering of the specimen, which is observed also in the other specimen.



(a) Bright-field micrograph of the as deformed state of the Co_3Ti processed by 20 turns at 8 GPa



(b) Diffraction pattern corresponding to the region shown in Fig. 5.23a showing only the rings corresponding to short range order.

Figure 5.23: Co_3Ti alloy deformed with 20 turns at 8 GPa by the method of HPT. Both, the bright-field image and the diffraction pattern show the amorphous structure of the specimen. In the diffraction pattern the rings corresponding to an amorphous short range order. Only a few very small crystals are present after deformation.

5.5 DSC Measurement Results

Having obtained an amorphous phase with a sufficient large volume fraction for investigation in the specimen as seen in Fig. 5.23 a DSC measurement is performed to investigate ex-situ the temperature of the devitrification process. For this a rest piece of the HPT disc deformed with 20 turns at 8 GPa after the punching out of the TEM samples is used. To avoid the influence of the crystalline central region on the heat flow signal, this part is punched away prior to the measurement. A heating rate of $20 \frac{\text{K}}{\text{min}}$ is used, heating the specimen from room temperature up to 590°C . In order to correct for the baseline a further full scan is recorded. The so obtained heat flow signal is shown in Fig. 5.24, showing a exothermic heat flow peak during the devitrification of the specimen at **517°C** . This is significantly lower than the value of about 607°C found in the literature [35] for samples amorphized by mechanical milling. The onset of the devitrification is found at about 509°C . The little spike in the signal at around 420°C is an artifact of the measurement, probably some instability in the electronics, and has no physical significance even if it shows up at a temperature which has been found to be the onset of devitrification during in-situ heating. As we will see later, the in-situ devitrification is affected by completely different mechanisms leading to a different result as compared to ex-situ heating.

To investigate the relaxation effects in the specimen, a two-step thermal treatment in the DSC is carried out (cf. Fig. 5.25). In the first step the temperature is increased at a rate of $20 \frac{\text{K}}{\text{min}}$ to 250°C and then held constant for 60 min. After cooling down to room temperature the specimen is heated up again to temperatures above the devitrification temperature using the same heating rate. The blue line in Fig. 5.25 corresponds to the signal obtained by the first heating step with the isothermal of 60 min. The slope of this signal is not the same as the slope of the curve from the second heating step, leading to an area between the two signal lines, corresponding to the heat flow by relaxation up to 250°C . The signal of the second heating cycle shows remarkable exothermal heat flow for temperatures between 300°C and 500°C , indicating that there is further relaxation going on before crystallization occurs. This is also true for the data in Fig. 5.24, not so pronounced in that case. The peak and the onset temperature are nearly the same as for the first dataset, confirming these values.

To compare the results of the in-situ experiment with specimen treated ex-situ, a disc shaped TEM specimen is thermally treated the same way as the in-situ specimen, following the temperature as logged in Fig. 5.26 during the DSC heating. In both cases the specimens are first heated up to 400°C and kept isothermal for 10 min. Then the temperature is raised stepwise by 10°C , with an isothermal time of 10 min in-between. Only at the 420°C step the temperature is held for 30 min, since at this temperature the onset of devitrification is observed during the in-situ experiment in the TEM.

CHAPTER 5. EXPERIMENTAL RESULTS AND DISCUSSION

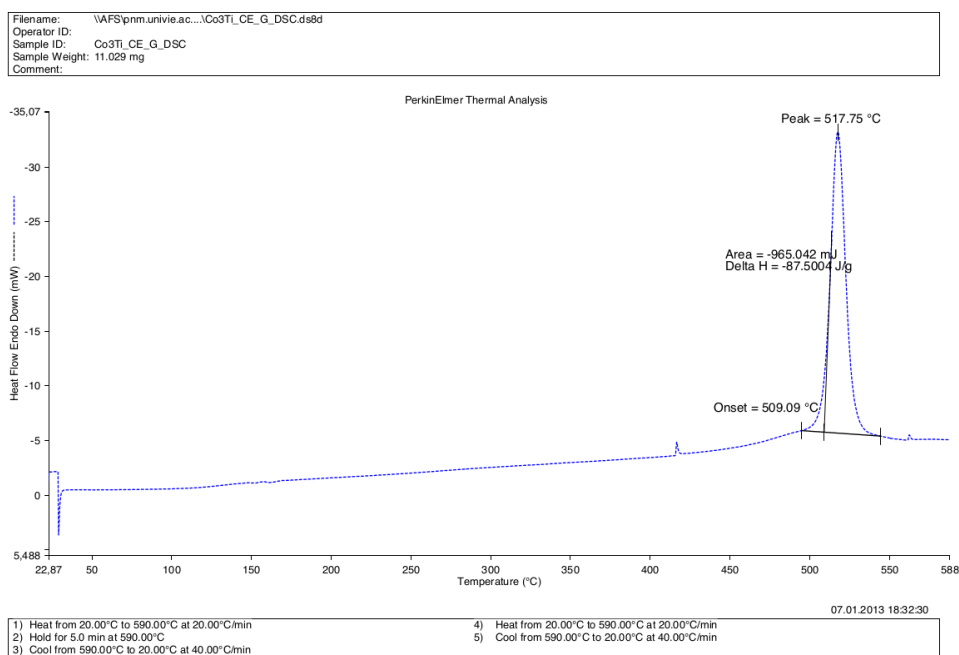


Figure 5.24: Heat flow (baseline corrected) from the specimen during heating from room temperature up to 590 °C.

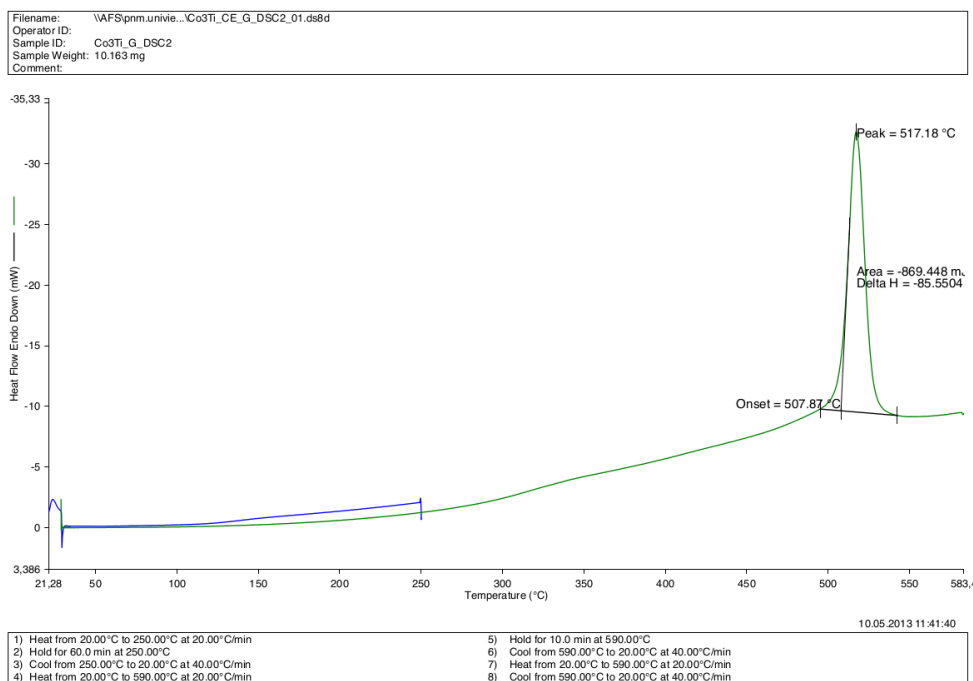


Figure 5.25: Heat flow (baseline corrected) from the specimen during relaxation investigation at 250 °C up to 590 °C.

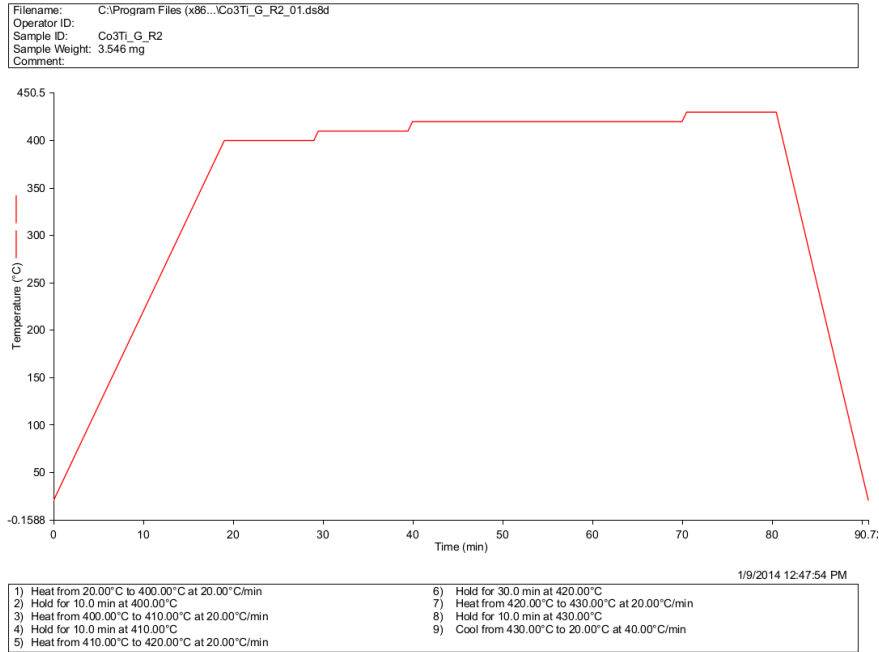


Figure 5.26: Temperature program of the bulk annealed specimen for comparison with the in-situ experiment.

5.6 Nanoindentation

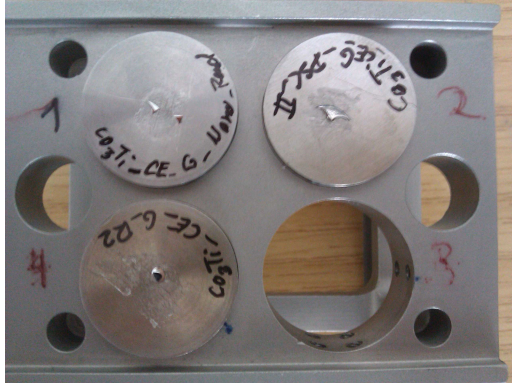
Nanoindentation is carried out at different stages of the specimen treatment to investigate the hardness H and Young's modulus E . All of the analysis is carried out with the specimen obtained out of the HPT disc deformed with 20 turns at 8 GPa and showing the amorphous phase. The three different states where the following:

- the as deformed amorphous alloy - 20 turns at 8 GPa
- a relaxed amorphous state obtained by step-annealing of a bulk sample in the DSC up to 430 °C as shown in Fig. 5.26.
- an in the DSC fully devitrified specimen: This specimen was first heated to 250 °C to investigate relaxation from the DSC signal (cf. Fig. 5.25), then it was heated up to 590 °C and held for 10 min, showing the full change to the crystalline phase as peak in the signal. This was later also confirmed by TEM investigation.

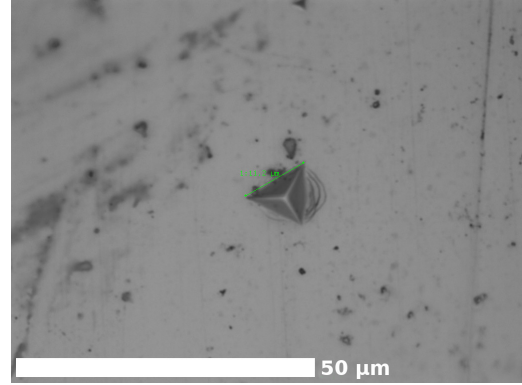
5.6.1 Experimental Setup

For the nanoindentation the surfaces of the specimens has to be quite smooth, which is achieved by mechanical polishing with grinding papers of decreasing grain size (P600-P2400). Finally the

surface is further polished with a $0.3\mu\text{m}$ polishing paste from Buehler. With this the desired smoothness of the surface could be achieved. Then the specimens are glued with an adhesive onto the cylindrical specimen holder, which themselves are fixed in the specimen stage of the nanoindenter by flipping the stage over on a smooth surface and inserting the cylinder from the bottom so that the surfaces are roughly aligned. Finally the stage is fixed in the instrument and a Berkovich tip is chosen for the measurement. Next the calibration file for the instrument is loaded.



(a) In the figure, the specimen glued onto the cylindric specimen holder are shown, which themselves are fixed in the stage with 6 little screws each, first aligning the surfaces by putting the stage upside down onto a smooth surface.



(b) Optical microscope image of the surface in a region of the amorphous phase. In the image the impression of the Berkovich tip is shown obtained with a load of 500 mN. On the right side of the impression one can clearly see some plastic material flow which has been observed to be pile-up by slightly changing the focus.

Figure 5.27: Initial setup for the nanoindentation measurements

As first step the stage is moved to the build in optical microscope with software control and focused so that an image of the surface is obtained. This is done by moving the stage in z-direction. The image is recorded by a digital camera on top of the microscope and displayed live on the screen. Now a good position of the specimen surface is chosen for measurements. First a tip approach point is set for a test approach, using a load threshold of $40\mu\text{N}$. This is carried out for all three specimens so that the approximative specimen surfaces could be found. Then a first test imprint was produced with a load of 500 mN to check the parameters and find the right load for the specimen.

In Fig. 5.27b the optical microscope image of the imprint of the Berkovich tip into the Co_3Ti is shown. From the image it is clear that the load has to be reduced since unwanted pile-up has been detected on two sites of the impression. The fact that it is indeed pile-up has been verified by slightly changing the focus and getting it in focus while the surface is out of focus. Also the imprint

is with $11.2\text{ }\mu\text{m}$ quite large for nanoindentation. Therefore the load for the actual measurements is reduced by a factor of 10 to 50 mN , which results in reasonable impression sizes with no indication of sink-in or pile-up.

As Poisson's ratio the value $\nu = 0.394$ (cf. [36]) is used for the quantification of the unloading curve.

5.6.2 Results of the Nanoindentation

The size of the imprints with a load of 50 mN is measured to be about $2\text{ }\mu\text{m}$ as side length of the triangle (cf. Fig. 5.28). This is a reasonable size for the measurements since the specimen surface affected by the imprint is homogeneous amorphous. So there are no limitations due to the size of different phases or grains. The same is true also for the relaxed and the fully recrystallized specimens.

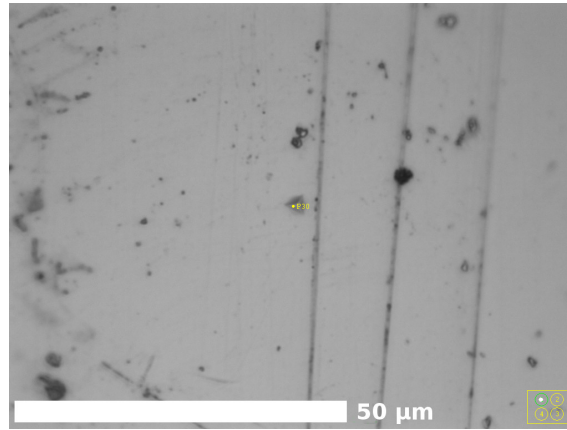


Figure 5.28: Imprint into the amorphous Co_3Ti surface with a load of 50 mN

In Fig. 5.29 the result of the nanoindentation measurement is presented. It is very interesting to notice that the Young's modulus as well as the hardness of the alloy increases as the temperature of the thermal treatment increases. The $20\text{ }^\circ\text{C}$ points in the graph corresponds to the as-deformed state, where no further heating was carried out. Its hardness is with $H = (6.48 \pm 0.15)\text{ GPa}$ the lowest off all three, the same is true for the young's modulus with $E = (131.1 \pm 3.8)\text{ GPa}$.

The second points correspond to the step annealed and relaxed specimen (cf. Fig. 5.26), which shows an increase in hardness to $H = (7.60 \pm 0.14)\text{ GPa}$ as well as in its Young's modulus $E = (141.1 \pm 2.6)\text{ GPa}$.

Finally, the fully crystalline specimen shows a further increase in hardness to a value of $H = (7.68 \pm 0.12)\text{ GPa}$ and a very drastic change in its Young's modulus to $E = (182.4 \pm 3.9)\text{ GPa}$ which is near the Young's modulus for the homogeneous single phase Co_3Ti with $E = 209\text{ GPa}$ [36].

So there is a trend towards higher Young's modulus and hardness values by relaxation and devitrification of the alloy. This indicates also the change of the deformation regime by changing from the amorphous structure to the nanocrystalline one. The change of the Young's modulus is correlated to changes of the structure, especially affected by the nearest neighbor binding configurations.

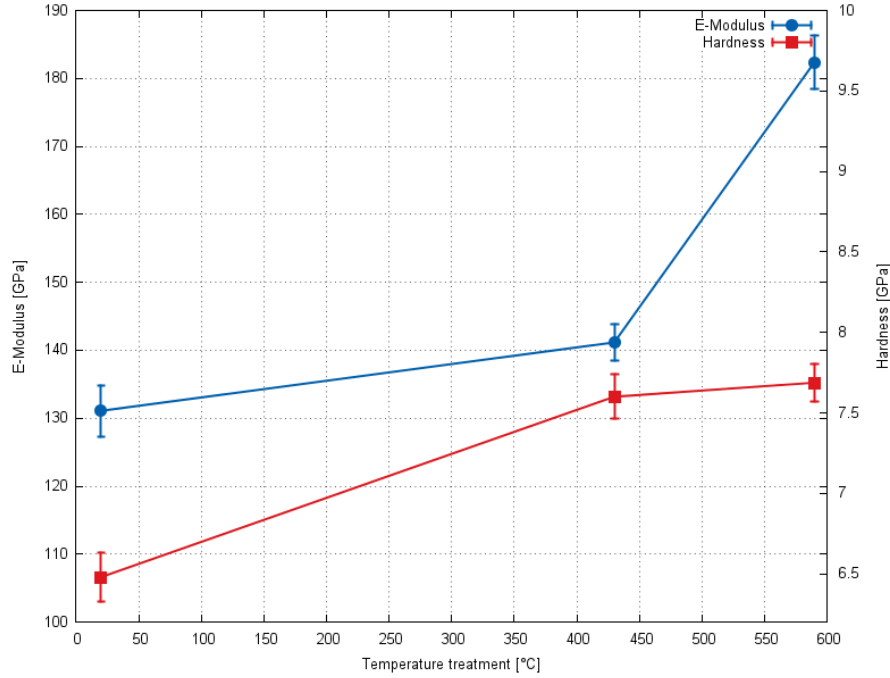


Figure 5.29: Young's modulus and hardness evolution of initially amorphous Co_3Ti by thermal treatment. The 20 °C point corresponds to the as-deformed state. All measurements are carried out at room temperature.

5.7 In-situ Heating Experiment

5.7.1 Setup and Preparation

For the in situ-experiment a TEM sample of the Co_3Ti HPT disc deformed with 20 turns at 8 GPa is punched out by spark erosion and electrochemically thinned as described in section 3.7. By this the sample thickness is reduced so that the thin regions can be penetrated by the 200 kV electron beam. The specimen is put into a special holder, allowing the heating via an external controller attached to the holder. This controller regulates the electric current through wires near the specimen, heating up the whole specimen surrounding. The temperature is measured by thermocouples attached to the holder.

5.7.2 Devitrification Observation During Heating

Prior to the heating experiment, a characterization of the initial state of the alloy is carried out, showing large areas of amorphous regions (cf. Fig. 5.30), which are confirmed to be amorphous by taking diffraction patterns (e.g. Fig. 5.23). The area shown in Fig. 5.30 is taken as the field of observation during the in-situ experiment. At this state there are a few particles present in the amorphous matrix. These particles with a size up to 100 nm are TiO_2 crystals formed during alloying and have a low volume fraction as compared to the amorphous regions of the Co_3Ti .

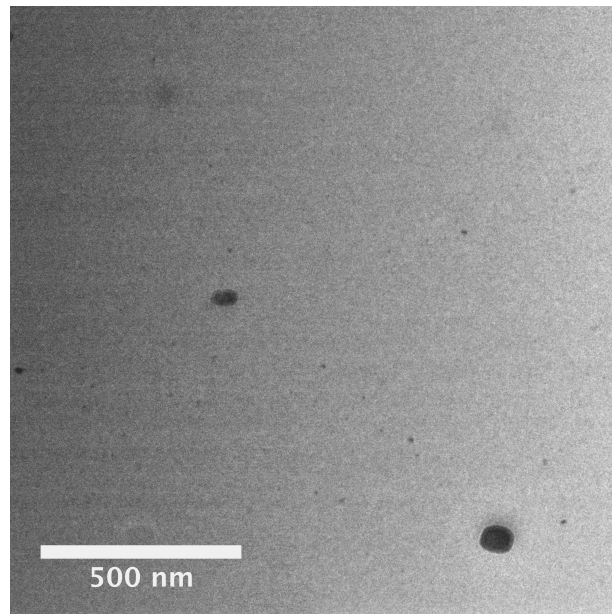


Figure 5.30: Bright-field image of Co_3Ti made amorphous by HPT (8 GPa, 20 turns) showing the field of observation before the in-situ heating experiment. There are some larger (~ 100 nm in size) particles present which are TiO_2 particles formed during the melting or the annealing process. Annotation: Under certain circumstances one sees a sharp vertical line in the center of the image. This is an artificial contrast arising from the camera readout and not a feature of the specimen.

The in-situ heating process is started following the temperature program as shown in Fig. 5.26, with the only difference that due to the controller of the heating holder the heating rate is not as constant as in the DSC. At each isothermal step bright-field images of the area of interest are taken, as shown in Fig. 5.31(a)-(d). The sequence of images reveals that the volume fraction of the crystalline phase increases with each 10°C step. The already present crystallites do not seem to act as nucleation centers, since (i) they do not grow and (ii) new crystallites arise independently all over the matrix. So the devitrification is not controlled by the initially present particles. This can be understood by the amorphous structure that has already some structural arrangements facilitating nucleation.

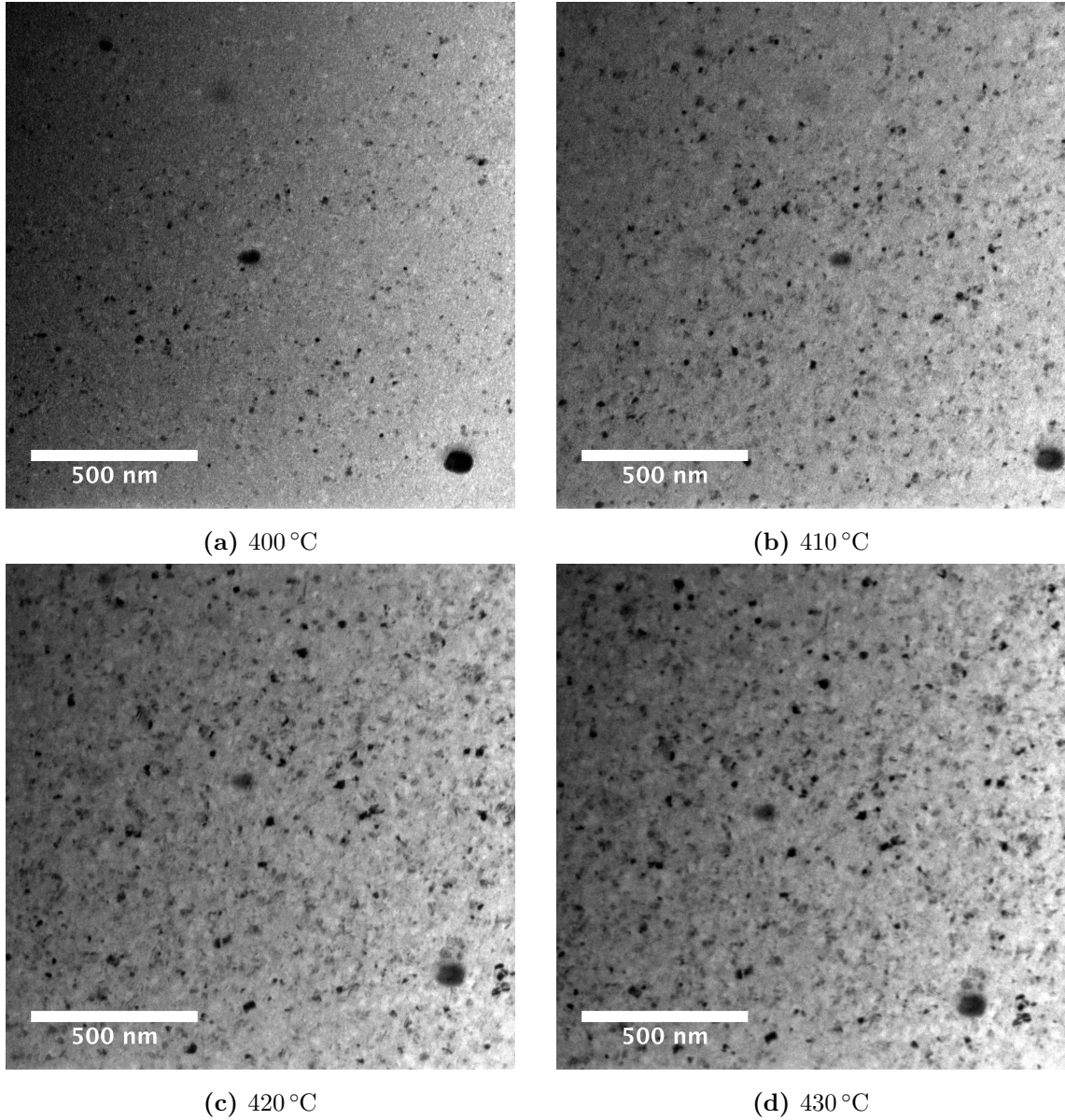


Figure 5.31: Devitrification of HPT deformed amorphous Co_3Ti during an in-situ heating TEM investigation. (a)-(d): Sequence of bright-field images taken at the indicated temperatures. The temperature step of 10 °C between each image leads to an increasing volume fraction of the crystalline phase.

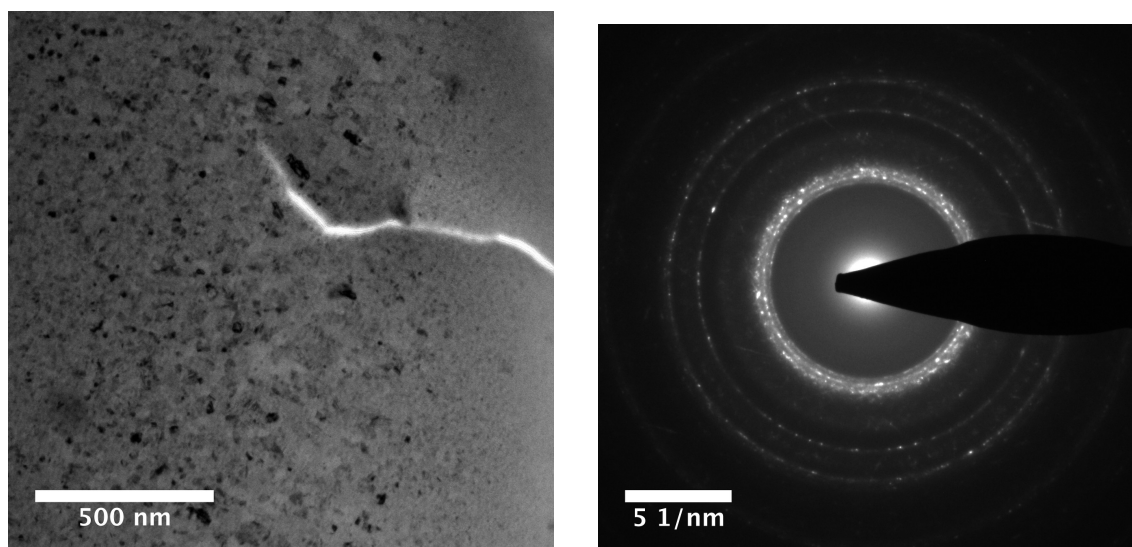
The contrast in Fig. 5.31(a)-(d) changes slightly because of bending of the specimen during the heating. The region of interest has to be centered again after each heating step as a result of the thermal expansion. The large particle seen in Fig. 5.30 is a good specimen feature to keep the field of interest. At 430 °C the devitrification is nearly completed as the crystalline phase has the largest volume fraction.

By comparing different regions it seems that devitrification starts first in the thinnest regions as seen in Fig. 5.32a, where the dominant phase after heating to 400 °C is clearly the crystalline one. The result is a volume fraction gradient of the crystalline phase, decreasing with increasing thickness. In this image the rim of the hole formed during electropolishing is on the right hand side, which can also be seen from the crack propagating from the rim into thicker regions.

The rim itself does not give strong contrast variations and it seems that the fraction of crystals is lower closer to the hole. The crystalline phase does not seem to form at all directly at the edge region. A possible explanation for this is an artifact created by surface effects.

The diffraction pattern in Fig. 5.32b corresponds to the region shown in Fig. 5.32a. The presence of diffraction rings confirms the already from the bright-field image seen fact of the polycrystalline nature of the devitrified phase. Also a lot of so called streaks, which are intensity lines across spots, are seen in the diffraction pattern. These streaks are formed by elastic scattering from defects, which are present in a high number in the small crystals.

It is very interesting that the observed ring pattern doesn't match the expected fcc ring pattern, since three very close inner rings are found in the diffraction pattern. The structure factor of the fcc lattice allows constructive interference and therefore intensity only to inner rings corresponding to [111] and [200] reflections. As we will see later, the hexagonal lattice shows the three rings with [100], [002] and [101] reflections. Therefore, it can be assumed that there is a chemical decomposition taking place during the in-situ devitrification, since the hexagonal phase must correspond to a Co-rich phase.



(a) Devitrification at 400 °C in a very thin region near the rim, showing already at this temperature the crystalline phase as strongly recovered. In the very thin regions the contrast variation vanishes.

(b) Diffraction pattern corresponding to the region in Fig. 5.32a, showing the polycrystalline reflections, indicating also the presence of a high defect density by the streaks and intensity of the rings.

Figure 5.32: Devitrification of HPT deformed amorphous Co_3Ti during an in-situ heating TEM investigation.

The nucleation rate of crystallization is high, since there arise a lot of new crystalline particles out of the amorphous matrix. In addition, they don't get to large because they impinge each other quite early during growth. Crystal coarsening is not taking place. Therefore the grain size lays in the range from **5 nm to 50 nm**, estimated by measuring a few crystal sizes manually. A try to perform an automated segmentation of dark-field images as shown in Fig. 5.33 unfortunately did not lead to useful results. The contrast variation in the crystals, caused by the planar defects, are disturbing the analysis to much, even with prior smoothing or blurring of the image. Therefore the segmentation and particle analysis is dependent on the used segmentation method and parameters and leads in general to a smaller particle size. Also the result of the segmentation changes when images of different magnification are analysed. A scientifically meaningful value could not be obtained by digital image processing because of this problems.

In Fig. 5.33 dark-field images are shown at which segmentation is performed. Fig. 5.33d shows the corresponding diffraction pattern with the circles where the objective aperture was placed over the spots for obtaining dark-field images. The aperture positions corresponding to the three example dark-field images are additionally marked by the arrows and the letters. The aperture is placed around spots showing high intensity and therefore correspond to lattice planes in good

Bragg condition, giving the crystals bright intensity in the dark-field image.

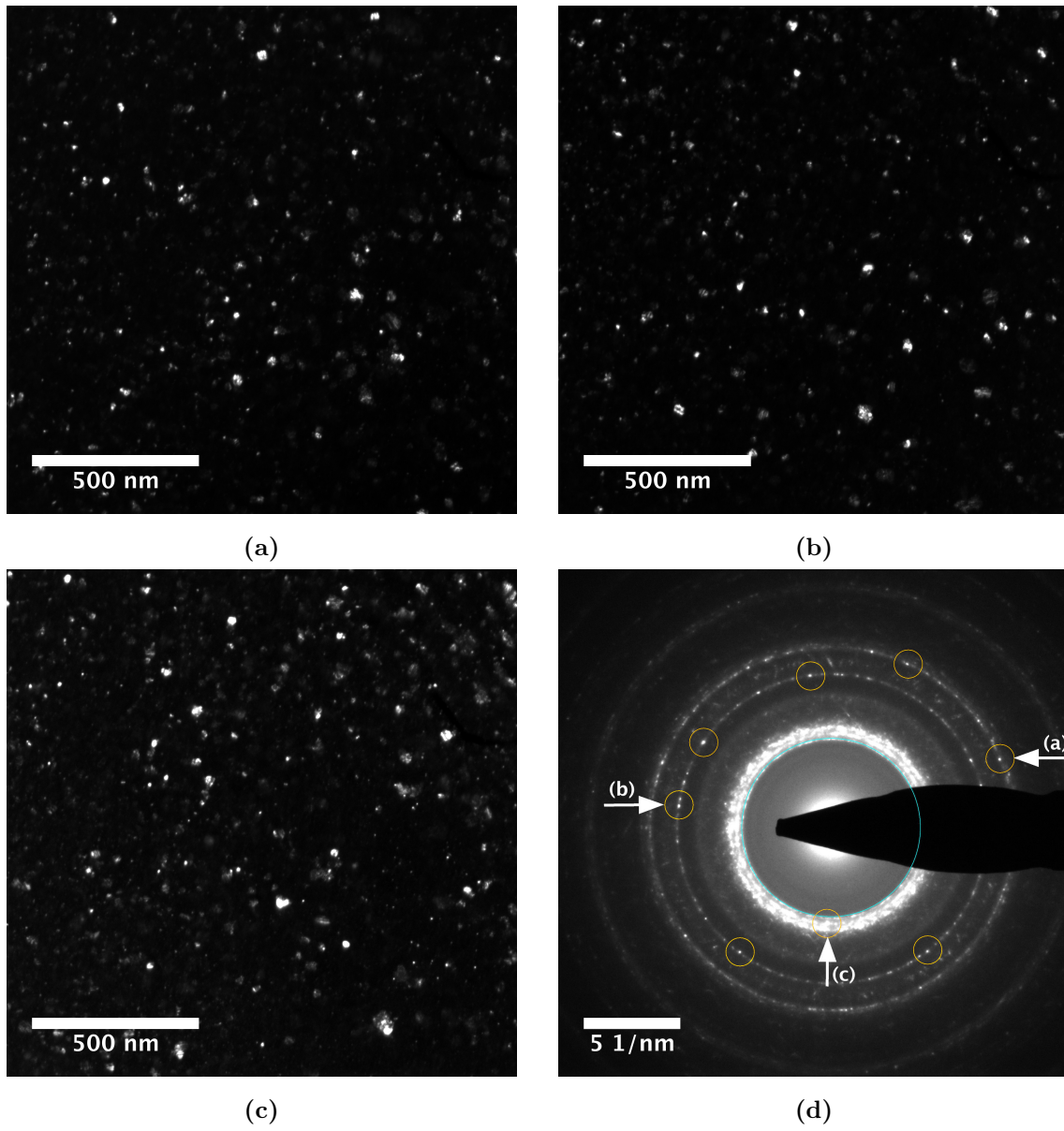


Figure 5.33: Example of dark-field images taken to analyze the particle size distribution. For the analysis always spots with high intensity are used, giving a better contrast in the images.

5.7.3 Structure Investigation

The appearance of the unexpected diffraction pattern lead to a closer investigation of the structure in terms of profile line analysis using the Digital Micrograph plugin written by Christoph Gammer called PASAD [37]. The software finds the center of a diffraction pattern and integrates the intensity with fixed radius for every radius, taking also into account a certain ellipticity. After this integration the tool allows to subtract the background and fit the peaks of the line profile by some desired fit functions. From this fit important information like the full width at half maximum or the position of the maximum can be obtained. By comparing the so obtained peaks with information from X-ray, the structure of the crystals is obtained. The resulting match to the **hexagonal Co-phase** is presented in Tab. 5.5.

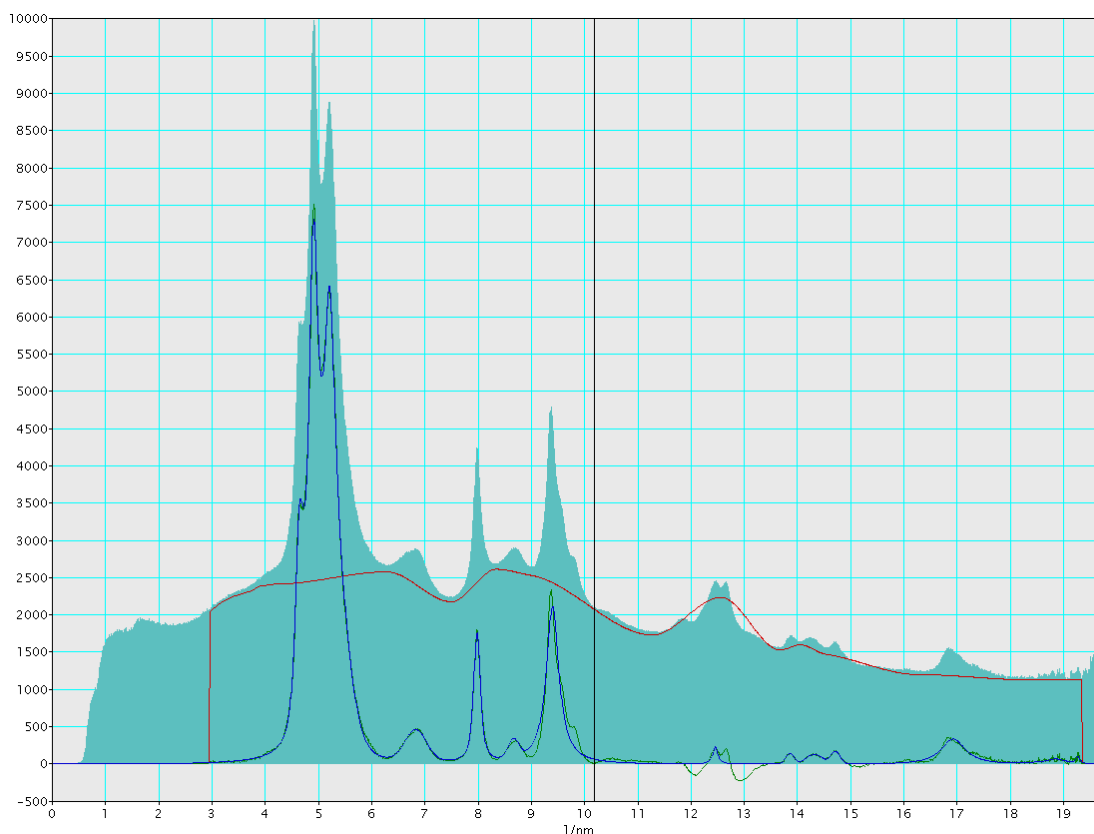
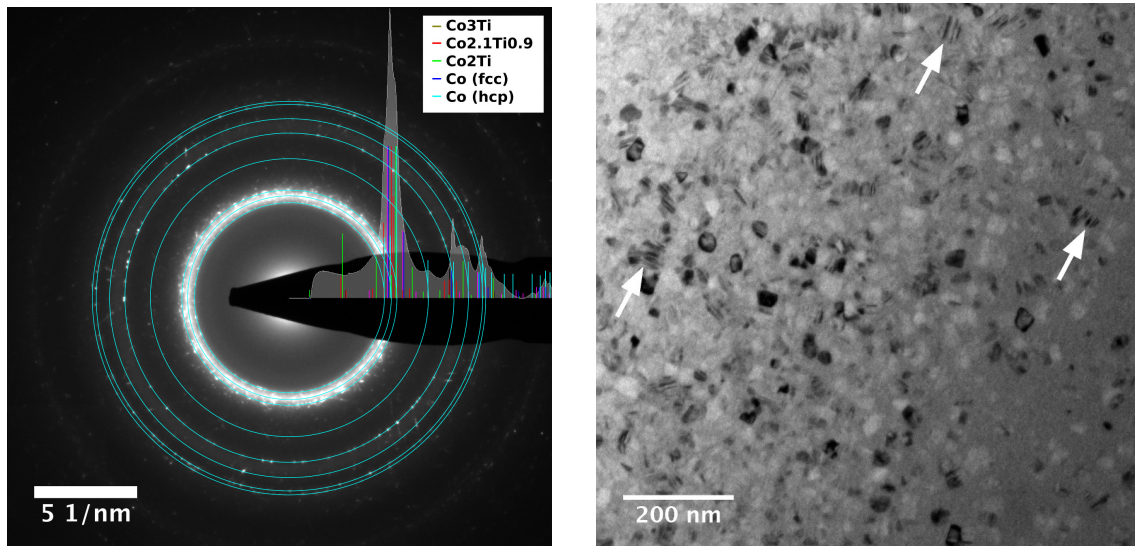


Figure 5.34: Line profile of a diffraction pattern as obtained by the radial integration of the PASAD [37] tool. In the figure also the background subtraction and the fit of the peaks by Voigt-functions optimized up to 10 nm^{-1} are illustrated.

In addition the ring radii of the diffraction pattern were measured and manually their relative fractions were compared to the other values. Following both methods the crystalline structure from the diffraction pattern is confirmed (cf. Fig. 5.35a) to be a hexagonal structure corresponding to a

Co-rich phase, as seen in the phase diagram Fig. 3.2. The following lattice parameters correspond to this structure: $a = 2.507 \text{ \AA}$, $c = 4.070 \text{ \AA}$. In general, Co exists in two allotropic phases which are a high temperature fcc phase and at temperatures below 422°C the mentioned hcp phase, as found in the literature [38]. In the bright-field image in Fig. 5.35b a high density of planar defects in the nanocrystals is observed as some of them indicated by the arrows. These contrasts of the planar defects are interpreted as stacking faults which could be confirmed later by HRTEM imaging of one of the particles.

The presence of a hcp phase is unexpected since the nominal concentration of the specimen as confirmed by EDX measurements in the TEM is the one of Co_3Ti . Consequently, in addition to the Co-rich phase a Ti-rich phase has to be present. But no Ti-rich phases are observed in the diffraction pattern.



(a) The PASAD analysis of the diffraction pattern indicates the presence of the hcp Co phase in the in-situ specimen after heating up to 430°C . The blue rings are experimental X-ray diffraction rings corresponding to this structure.

(b) The bright-field image corresponds to the region from which the diffraction pattern Fig. 5.35a is obtained. There are many particles showing planar defects present as indicated by the arrows.

Figure 5.35: Structural analysis of the in-situ specimen by comparison with experimental values obtained by X-ray diffraction.

To shortly summarize the observations from this section: An initially amorphous Co_3Ti alloy is electrochemically thinned to electron beam transparency and heated stepwise up to 430°C in the TEM. At around 400°C in the thin regions around the rim of the hole, nanocrystals nucleate in a high number from the matrix, the already present crystals do not act as nucleation centers.

Their size remains the same during devitrification. The structure analysis of the particles by the diffraction patterns recorded after cooling down to room temperature indicate the presence of the hcp Co-rich phase. Bright-field images show a high defect density in many particles, which can be interpreted as a first hint for an incomplete polymorphic phase transformation taking place during the cooling down of the specimen from the high-temperature phase to the low temperature one.

Co (hex)	XRD		PASAD		manual
hkl	1/d [nm ⁻¹]	XRD-int	1/d [nm ⁻¹]	PASAD-int	1/d [nm ⁻¹]
100	4.606	40	4.624	30	4.618
002	4.914	41	4.886	100	4.916
101	5.219	100	5.188	96	5.206
102	6.734	25	6.812	12	-
110	7.974	24	7.961	21	7.998
103	8.688	24	8.647	3	-
200	9.208	17	-	-	-
112	9.372	23	9.380	53	9.379
201	9.532	20	-	-	-
004	9.823	17	-	-	-

Table 5.5: Structural investigation of the in-situ formed crystals from the diffraction patterns. The table presents the matching diffraction ring pattern from X-ray diffraction (XRD) data. The rings with weak intensity in XRD are not found in the electron diffraction patterns.

5.8 High Resolution Imaging of the In-situ Devitrified Specimen

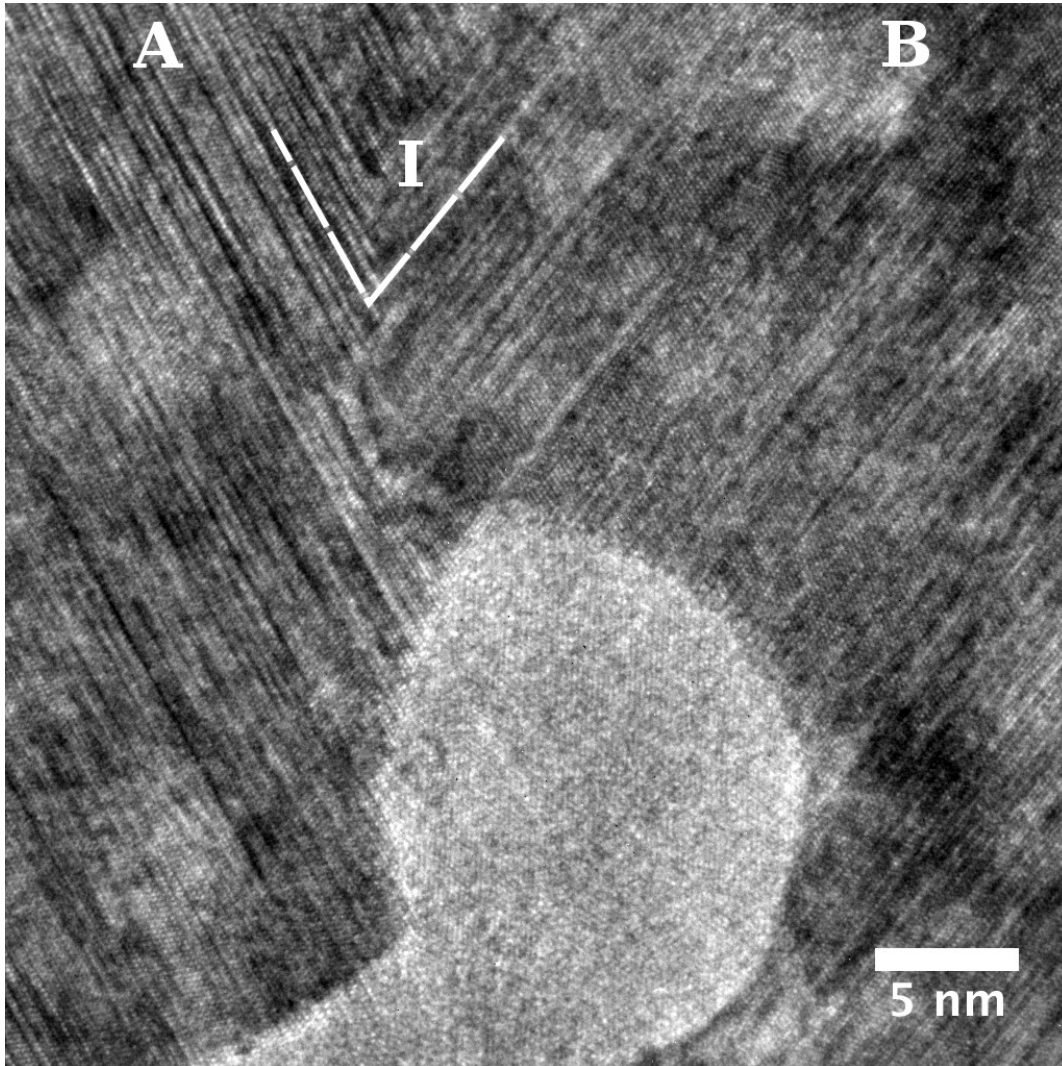


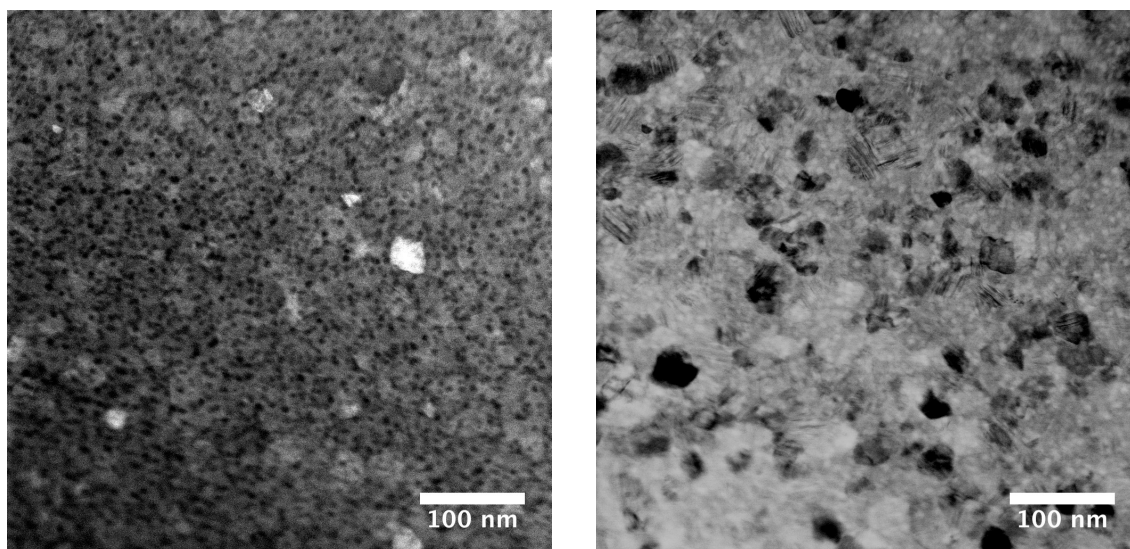
Figure 5.36: Devitrified Co_3Ti after in-situ heating. Unprocessed HRTEM image showing two orientation variants of the low temperature (hcp) phase with a high number of planar defects. The atomic resolution structure of some areas reveals still the presence of the fcc stacking sequence of the high temperature phase.

To obtain atomic resolution of the specimen, a CM30 TEM with an acceleration voltage of 290 kV is used. To reduce the aberrations fine adjustments of the imaging system are performed, especially to reduce the objective lens astigmatism and optimize the beam alignment relative to the optical axis of the objective lens. The best imaging contrast is then obtained by slightly underfocus the image (Scherzer defocus) by this resolving the atomic planes using interference contrast. Since tilting of the specimen is not easy at high magnification, resulting in an immediate lost of position,

the best way to obtain a good zone axis orientation is by just searching particles which are oriented well. This is possible since there are a lot of particles with statistically independent orientations present in the specimen. For the image calibration the (111) reflections of the power spectrum of a high resolution image of the 'as annealed' Co_3Ti specimen using the same microscope parameters is used.

Fig. 5.36 shows a HRTEM image of a particle exhibiting atomic lattice fringes and in some regions even atomic columns. A bright particle down in the center also shows some contrasts on an atomic scale, but they are very diffuse and not good enough for interpretation. The large particle shows an interface, (near I) where some of the linear contrast (dashed lines) seen in area A seem to propagate into area B. The angle between the corresponding atomic planes of the two areas is in the range of 67° to 70° , depending on where the angle is measured. The interplanar distance $d = (0.20 \pm 0.01) \text{ nm}$ as measured normal to the planes corresponds quite good to the distance of the $\{111\}$ planes ($d_{111} = 0.2059 \text{ nm}$ [39]) in the high temperature fcc structured Co. This seems reasonable since the $\{111\}$ planes are planes of largest spacing. Also the angle of $(72 \pm 1)^\circ$ as measured from the image corresponds to an angle between $\{111\}$ planes of the fcc structure which is $\alpha = \arccos\left(\frac{(111) \cdot (\bar{1}\bar{1}\bar{1})}{|(111)||(\bar{1}\bar{1}\bar{1})|}\right) \approx 70.5^\circ$. The stacking sequence of the columns is mostly an ABCABC stacking corresponding to an fcc structure. But the high stacking fault density leads to strong variations. In other regions the stacking sequence shows a variation from the ABCABC sequence to the ABAB stacking sequence of hcp. From this it is deduced that the fcc structure found in this particle is retained from the high temperature Co phase, formed during the in-situ heating experiment. On the other hand during cooling most of the particle volume undergoes the polymorphic, diffusion less phase transformation and is therefore present in the form of hcp structured, Co rich crystallites as found in the diffraction pattern Fig. 5.34.

5.9 Chemical Analysis in the STEM



(a) HAADF image of the in-situ devitrified specimen showing a large number of nm-sized particles which could be identified to be TiO_2 crystals. Other crystals show a bright contrast as they have a higher Co concentration relative to the matrix.

(b) Bright-field image corresponding to Fig. 5.37a showing the diffraction contrasts as seen in the TEM before. In the background however also the TiO_2 particles can be seen.

Figure 5.37: STEM images showing clearly the formation of nm-sized TiO_2 particles which are formed by the in-situ heating and lead to a phase separation resulting in a Co rich matrix.

Since structural investigations of the diffraction patterns didn't reveal a Ti-rich phase, needed to obtain the nominal composition and because the EDX measurements in the TEM showed still the nominal stoichiometry, for clarification a STEM analysis using a Titan microscope with 4 X-ray detectors for better signal to noise ratio for EDX and analysis by EELS are carried out.

In Fig. 5.37 a STEM high angle annular dark field (HAADF) and a bright-field image are shown, which reveal the presence of many nm-sized particles with dark contrast in the HAADF image Fig. 5.37a. In the bright-field they show as to expect a bright contrast. This indicates that these particles have a lower mean Z-value as compared to the matrix and therefore don't scatter the narrow beam as much as the other regions. These contrasts could not be seen in this clear form by the diffraction contrasts in the conventional TEM. Despite the many small particles, there are also some larger grains scattering many of the electrons to high angles, indicating a higher mean Z-value as compared to their surrounding and therefore containing more Co. Unfortunately local EDX measurements do not reveal any significant concentration variations. Therefore an analysis

using the EELS system of the Titan microscope is carried out for better spacial resolution, not obtained by EDX.

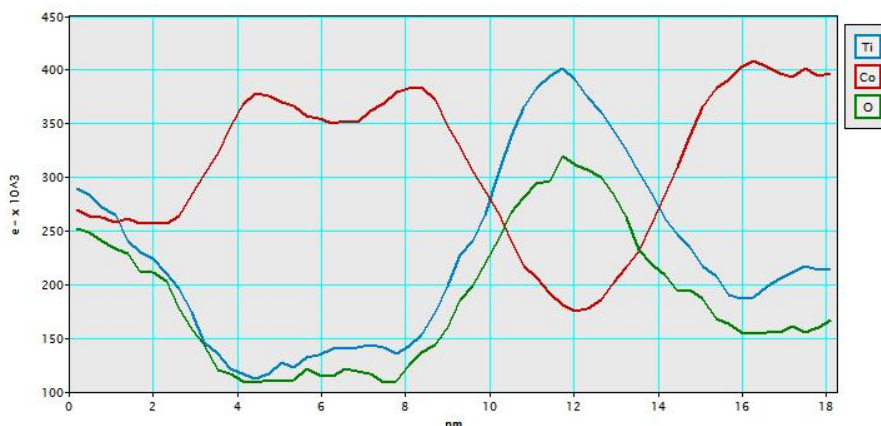


Figure 5.38: Integrated EELS signal using three different integration windows around the characteristic edges of Co, Ti and O as a function of position on the specimen. The scanned line is shown in Fig. 5.40.

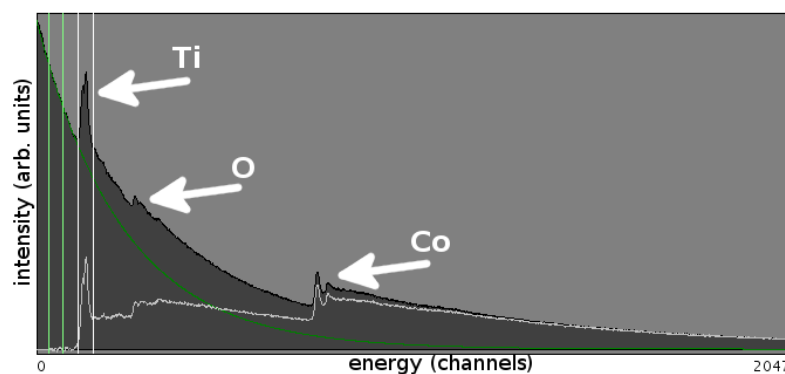


Figure 5.39: EELS spectrum image recorded for a point on the specimen. The characteristic edges for the elements are marked with arrows. The energy scale is given in relative values. The green curve is an example fit for the background and has to be set for each edge individually. The white lines correspond to the integration window.

The EELS spectra are recorded for a line over particles showing bright and dark contrast in the HAADF signal. From the so obtained spectra the characteristic edges of the signal were integrated by subtracting the background and using a well chosen integration window around the edge (cf. Fig. 5.39). This gives an intensity value in the form of number of counts which is affected by the local element concentration. By selecting the characteristic edges for Co, Ti and O for integration and plotting the integrated values as a function of position a relative concentration measurement can be carried out.

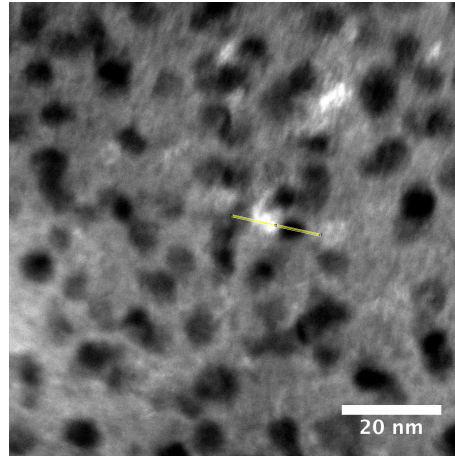


Figure 5.40: HAADF image showing particles with bright and dark contrast according to their mean Z-value. The line indicates the positions over which the EELS spectra are recorded leading to the curve in Fig. 5.38

The plot of the processed EELS spectra as in Fig. 5.38 clearly revealed the presence of TiO_2 particles, corresponding to the dark crystallites in the HAADF images. This is deduced since the relative concentration of Ti and O show a strong correlation in the relative concentration. Also a Co-rich particle is found as expected, showing the bright contrasts in the HAADF images.

This finally also explains the PASAD results of Fig. 5.35a, since the oxidation of the specimen during in-situ heating is carried mostly by the oxygen getter material Ti, leading to a Co richer matrix which itself therefore recrystallizes in a Co high temperature fcc structure and undergoes the polymorphic phase transformation to the hcp structure during cooling down of the specimen. Due to the small size this transformation might not be complete since the size stabilizes the high temperature phase, leading to a high stacking fault density and areas with the retained high temperature phase as seen in Fig. 5.36.

5.10 Ex-situ Bulk Heated Specimens

A first ex-situ annealing of a specimen is performed to compare the results with the in-situ heated specimen. The temperature program followed by the DSC is shown in Fig. 5.26. The program is chosen to be as similar to the in-situ heating as possible to get comparable results. As seen in Fig. 5.41, in contrast to the in-situ specimen the ex-situ specimen shows nearly no devitrification at temperatures up to 430°C . This is to expect since the results of the in-situ experiment clearly shows that the large surface to volume ratio and the oxidation of Ti on this surface leads to a decomposition which doesn't take place in the bulk specimen. The TEM micrographs are comparable to the state of the as deformed Co_3Ti specimen. The corresponding diffraction pattern as

well shows only amorphous rings and no crystalline spots. This is also expected since the heat flow signal in the DSC measurement doesn't show the peak corresponding to the devitrification at this temperatures. But there are some structural changes in the amorphous phase as already shown by the nanoindentation experiments carried out on this specimen, leading to a increase in hardness and Young's modulus (cf. Fig. 5.29). The increasing hardness might indicate a relaxation towards a more stable configuration.

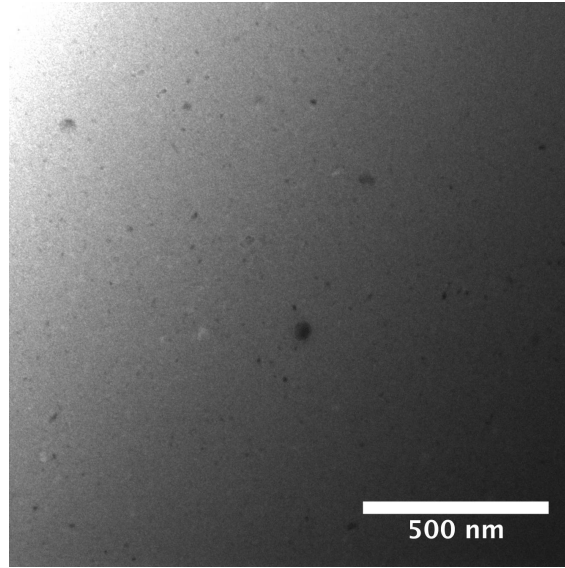
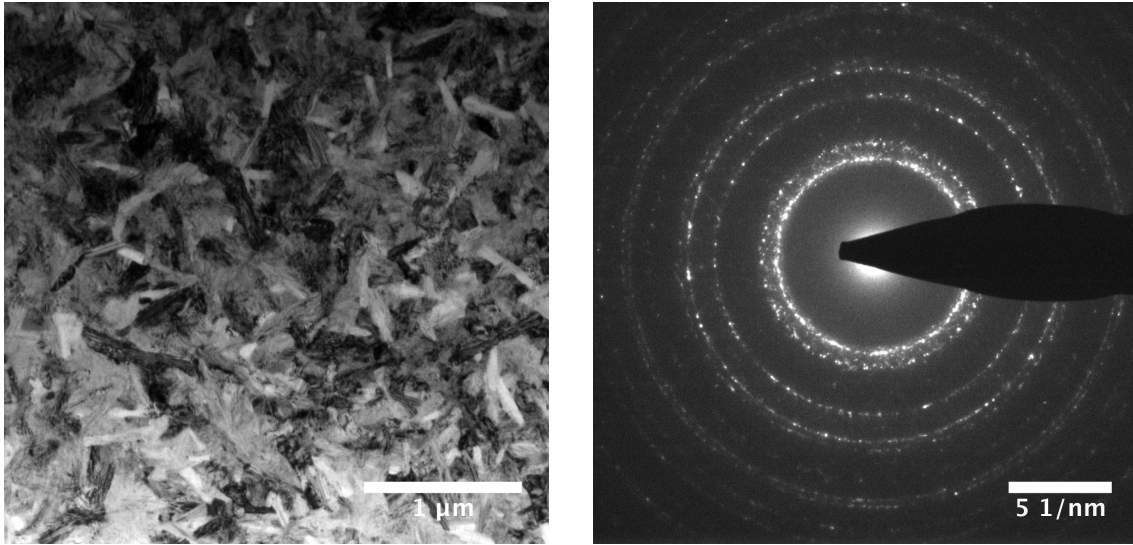


Figure 5.41: TEM bright-field image of the ex-situ heated specimen for comparison with the in-situ experiment. The temperature program followed by the DSC is chosen to be as similar to the in-situ temperatures as possible.

Since this first attempt doesn't show the devitrification, other end-temperatures for the DSC runs are set. Since the experimental results from the previous DSC runs (cf. Fig. 5.24 and Fig. 5.25) showed an onset of about 510°C when using a heating rate of $20 \frac{\text{K}}{\text{min}}$, a run with the same heating rate and an isothermal of 10 min at 480°C is performed. The goal is to see the formation of crystallites at the onset of devitrification. The TEM images of the so obtained specimen are represented by Fig. 5.42.

The TEM micrograph shows that the specimen is already fully recrystallized, since the isothermal of 480°C for 10 min is long enough for the diffusion to fully recover from the amorphous state. Selected area diffraction patterns of the crystals showed an fcc structure, demonstrating that the devitrification is polymorphous. The plate like shape of the crystals is obtained because of anisotropy of growth. This can be explained because in fcc the $\{111\}$ planes in $\langle 110 \rangle$ directions (the closed packed planes in the closed packed direction) are energetically more stable then other planes and directions and therefore grow faster than others. The crystallites show many planar



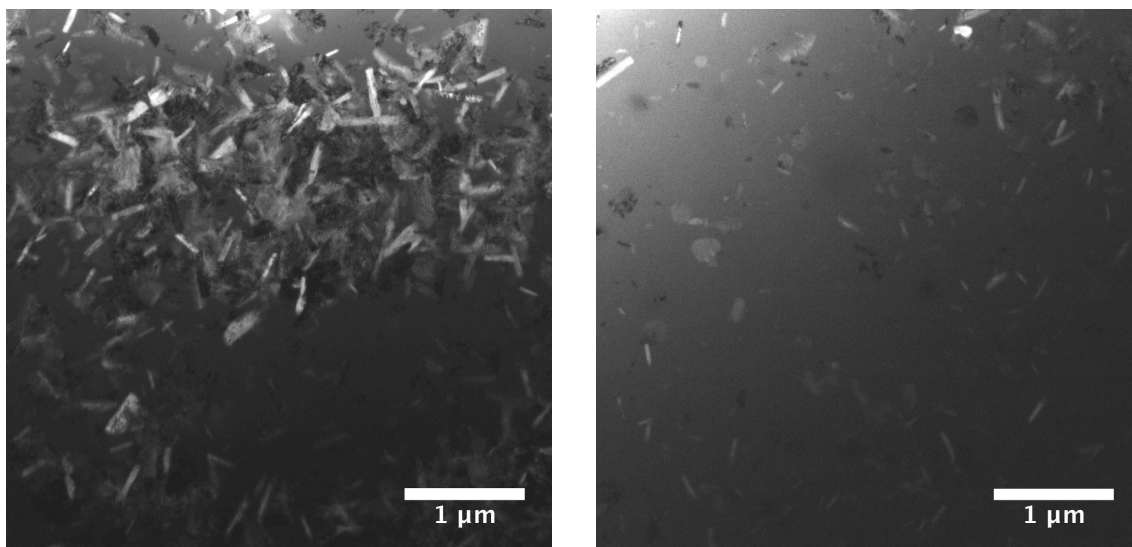
(a) The bright-field image shows large plate shaped crystallites, which indicated the anisotropy of growth.

(b) The diffraction pattern from Fig. 5.42 shows the expected fcc structure of the crystals. The specimen seems not to be long range ordered, since the superlattice reflections are not visible.

Figure 5.42: State of the ex-situ heated specimen using a heating rate of $20 \frac{\text{K}}{\text{min}}$. After the thermal treatment for 10 min at 480°C the specimen is fully crystalline.

defects which seem to be stacking faults and twin boundaries.

To obtain a lower crystalline fraction in the amorphous volume, the annealing temperature was further reduced and at 465 °C found to be good for getting the desired results, leaving all the other parameters the same. In Fig. 5.43 bright-field images of two different regions of the specimen treated with this parameters are shown. In Fig. 5.43b a region with a low crystalline volume fraction is shown whereas in Fig. 5.43a a higher volume fraction can be seen. I would like to emphasize that both images are obtained from the same sample in neighboring regions of the specimen. This means the devitrification is inhomogeneous with respect to different sample positions.



(a) TEM bright-field image of a region of the Co_3Ti specimen with a relative high density of crystalline area.

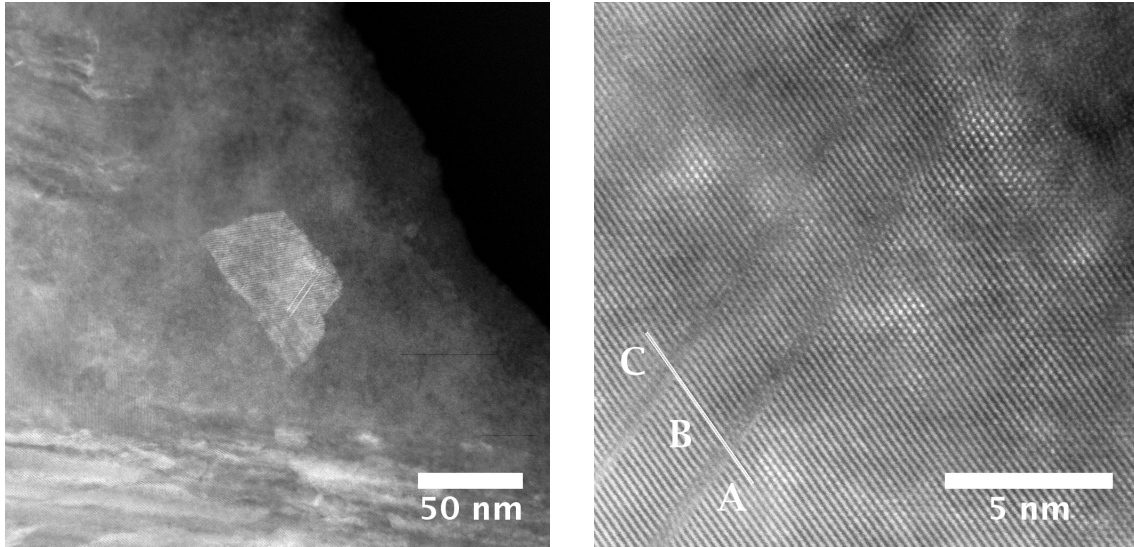
(b) TEM bright-field image of a region with a low number of crystallites present in the amorphous matrix.

Figure 5.43: Bulk annealed specimen treated with 465 °C for 10 min after heating with 20 $\frac{\text{K}}{\text{min}}$. The specimen shows an inhomogeneous distributed number of the plate shaped crystallites emerging from the matrix.

5.10.1 STEM of the Ex-situ Bulk Heated Specimen

Atomic resolution STEM images of the bulk devitrified specimen are obtained by using a Nion UltraSTEM 100 operating at 100 kV. Fig. 5.44a shows a medium angle annular dark-field (MAADF) overview of a particle near the rim of the hole. The particle is oriented near a zone axis, allowing atomic resolution imaging. The ABCABC stacking sequence of the atomic columns confirms the fcc structure found in the diffraction patterns (cf. Fig. 5.42b). Fig. 5.44b is a HAADF image recorded from a region near the two bright lines seen in Fig. 5.44a. These lines are found to be multiple stacking faults of the $\{111\}$ planes in the fcc structure. The line in the image shows that

the atomic column positions between the region marked with A and the one marked with B are aligned. Between region B and C this is not the case. Here the stacking faults lead to a relative displacement of the columns. This means the number of stacking faults has to be different to the one between A and B.



(a) MAADF image of a Co_3Ti particle from the bulk devitrified specimen. The crystal shows two bright lines which are stacking faults.

(b) HAADF atomic resolution image of the defects found in the crystal (cf. Fig. 5.44a). The defects are multiple stacking faults of the resolved $\{111\}$ crystal planes

Figure 5.44: STEM images of a crystal of the bulk heated specimen. The crystal is near the rim of the hole and oriented near a zone axis allowing atomic resolution imaging.

6 Summary and Conclusions

6.1 High Pressure Torsion Deformation and SEM

Intermetallic Co_3Ti is casted from high purity elements and molten into a rod form for further processing. The so obtained specimen initially consists of two phases as measured by EDX in the SEM. The two phases are dissolved into the single phase Co_3Ti with a nominal concentration of 23at.%Ti-77at.%Co by annealing for 100 h at 950 °C.

Disc shaped specimens are cut and punched out by spark erosion. The samples, 8 mm in diameter and 0.55 mm high, are deformed by HPT. Deformations to different nominal shear strains are carried out under different conditions:

- 20 rotations at 4 GPa
- 80 rotations at 4 GPa
- 20 turns at 8 GPa

SEM investigations of the cross-section show that both deformations at 4 GPa result in a mostly retained crystalline specimen with a huge number of intersecting amorphous bands. By 20 turns at 8 GPa the specimen can be rendered homogeneously amorphous in the outer high strained regions. From this specimen TEM samples are prepared for in- and ex-situ experiments.

6.2 In-situ Heating Experiment in the TEM

The in-situ devitrification of the specimen in the TEM results in a phase decomposition triggered by a surface effect. This strong dependency is unexpected and reveals one possible difficulty with in-situ studies in the TEM. In the present case the devitrification follows completely different routes and kinetics as compared to devitrification in the bulk and therefore different information is obtained by the in-situ experiment.

The in-situ phase separation is found to be initiated by the oxidation of Ti, caused by its high oxygen affinity and the TEM specimen geometry, which allows the small amounts of O_2 present in the high vacuum of the microscope (pressure $\sim 10^{-5}$ Pa) to react with the Ti on its large surface. This reaction is found to be accelerated at temperatures around 400 °C. The formation of probably TiO_2 leads to a local reduction of the Ti concentration in the matrix near the oxide particles. This

results in a destabilization of the amorphous matrix in these regions, leading to the formation of Co-rich nanocrystals, trying to be in their thermodynamical equilibrium state. At the temperatures of 430 °C this is an fcc structure. Since in the thin TEM foil nearly all areas are affected by oxidation, the Co-rich fcc nanocrystals grow everywhere, but the formation is seen first in the very thin regions, resulting in a decreasing volume fraction towards thicker areas.

The hcp structure of the Co-rich nanocrystals observed in diffraction patterns (cf. Fig. 5.35a) taken at room temperature is explained by a polymorphic phase change during cooling in agreement with the phase diagram. Nevertheless, in HRTEM images the presence of an fcc structure with ABCABC stacking sequence containing a high stacking fault density is found. This fcc structure is a remnant of the initially formed crystal structure at the higher temperature, stabilized by the small particle size (5 nm to 50 nm) at lower temperatures. The small size is a consequence of the frequent impingement of particles due to the high nucleation rate and low growth rate.

The oxide formation and phase separation is finally also confirmed by EELS measurements, showing a strong correlation between Ti and O, as well as Co-rich particles with low Ti and O concentration (cf. Fig. 5.38).

6.3 Ex-situ Heating Experiment

In contrast to the in-situ experiment, the ex-situ annealed specimen showed simply the occurrence of fcc structured crystals as revealed by both, electron diffraction and atomic resolution STEM. There is no decomposition taking place as the alloy drifts towards the thermodynamical equilibrium, according to a polymorphous crystallization. The crystals interestingly grow into a plate like form, which can be explained by preferential growth of the energetically more stable planes and directions. The onset of devitrification is dependent on the heating rate and annealing time since atomic rearrangement is needed to reach energetically more stable configurations. For a heating rate of $20 \frac{\text{K}}{\text{min}}$ followed by isothermal annealing for 10 min the temperature of devitrification was found to be in between 450 °C and 465 °C. Heating with constant heating rate of $20 \frac{\text{K}}{\text{min}}$ without isothermal treatment resulted in a devitrification onset of 509 °C and a peak of 517 °C. This value is considerably lower to Co_3Ti samples amorphized by mechanical alloying (peak at 607 °C) [35]. By controlling the annealing temperature and time, the crystalline volume fraction in the specimen can be controlled. The partially crystallized sample shows a quite inhomogeneous distribution of crystals over the specimen volume, sometimes containing many, sometimes less crystal plates.

6.4 Nanoindentation

For the nanoindenter measurement three different states of Co_3Ti are prepared by heating of the amorphous phase (for details see Sec. 5.6):

- as prepared
- relaxed
- fully recrystallized

The nanoindenter measurements of the three specimens show significant differences in hardness and Young's modulus. The results presented in Fig. 5.29 show an increase in hardness by about 18.5% from $H = (6.48 \pm 0.15)$ GPa to $H = (7.68 \pm 0.12)$ GPa from the deformed to the fully recrystallized state as well as an increase of the Young's modulus by about 39% from $E = (131.1 \pm 3.8)$ GPa up to $E = (182.4 \pm 3.9)$ GPa. This interesting experimental result needs further investigations.

List of Tables

3.1	Mass of material needed for the production of a rod (6 mm diameter, 50 mm long)	11
3.2	Mass of the 3 sets used for the inductive melting	11
5.1	EDX results of the 6 different regions corresponding to the rectangular areas marked in Fig. 5.2a.	31
5.2	EDX results of the 5 different regions corresponding to the rectangular areas marked in Fig. 5.2b.	31
5.3	EDX Concentration measurements of the as cast specimen showing the atomic percent of elements found by the software.	34
5.4	Concentration measurements of the as annealed specimen show a single phase with the desired composition. The spectra correspond to the marked regions in Fig. 5.5b.	36
5.5	Structural investigation of the in-situ formed crystals from the diffraction patterns. The table presents the matching diffraction ring pattern from X-ray diffraction (XRD) data. The rings with weak intensity in XRD are not found in the electron diffraction patterns.	61

List of Figures

2.1	Schematic illustration of the scattering of a plane wave on parallel lattice planes with spacing d . [14]	5
2.2	Schematic representation of the interference as described by Laue. [15]	5
3.1	In the face centered cubic unit cell all lattice points are equivalent, as shown in (a). In (b) we see the $L1_2$ unit cell corresponding to an intermetallic Co_3Ti alloy, where the atoms sit in an ordered way on the lattice points. On the corners there sit the Ti-atoms (blue) and in the face centers there sit the Co-atoms (red).	9
3.2	Phase diagram for Co-Ti alloys with a line showing the desired concentration and the corresponding phase. [17]	10
3.3	The figure shows three different geometries used for HPT deformation of specimen. (a) unconstrained geometry (b,c) constrained geometry. [22]	13
3.4	The figure shows a schematic representation of the specimen geometry. The torsional strain is not the same over the whole specimen, but has a radial dependency. [22] .	14
3.5	The pictures show the twin-jet electropolishing equipment used for the TEM-specimen preparation.	16
4.1	In the figure a schematic representation of a typical transmission electron microscope setup is shown. [26]	18
4.2	In the figure a schematic representation of a scanning electron microscope setup is shown. [27]	21
4.3	Schematic representation of different signals obtained by electron-specimen interactions in different operation modes of an electron microscope.	22
4.4	Schematic representation of the nanoindentation process	25
4.5	The pictures show the Perkin Elmer DSC 8500 used for the thermal treatment of the specimen.	28

List of Figures

5.1	SEM images of the “as molten” specimen cross-section taking with the backscattered detector. The images reveal that there are two phases present, one formed by dendritic growth out of the melt, which indicates low nucleation and therefore a undercooling of the melt.	30
5.2	EDX measurements of the alloyed Co_3Ti in the cross-section of a slug.	31
5.3	Phases present in the alloy after the rod production as seen on the surface of a cut normal to the cylinder axis.	33
5.4	SEM image of Co_3Ti - Phases in the material before the annealing are characterized by EDX. The quantitative results are given in Tab. 5.3.	34
5.5	SEM image of Co_3Ti - After annealing only one phase is present in the alloy. . . .	35
5.6	The graphs show torque curves as a function of turns recorded during HPT deformation of the specimen with different settings. During the deformations with the smaller pressure of 4 GPa, the torque curve shows many instabilities which indicate possible slip and cracking of the sample. The green curves overlayed over the red ones are smoothed data sets to better see the trends.	37
5.7	Scans of the as deformed HPT discs	38
5.8	Disc deformed by 20 turns at 4 GPa at RT.	39
5.9	SEM backscattered image showing the retained crystalline phase intersected by broader and finer amorphous bands.	39
5.10	The position near the center of the disk shows many fine bands with a preferred orientation.	39
5.11	Deformed by 80 turns at 4 GPa at RT.	40
5.12	Cracks are forming near the interface of the broad amorphous band and the crystalline phase.	40
5.13	The interface region from which the ring broke of after unloading in detail. The arrow marks an amorphous part of a shear bands which might have caused the inner tensions leading to crack formation.	40
5.14	Deformed by 20 turns at 8 GPa at RT.	41
5.15	The outer regions of the specimen show a homogeneous amorphous area over the whole specimen thickness.	41
5.16	In the central region the volume of the crystalline phase increases as expected. . .	41
5.17	Deformed by 20 turns at 8 GPa at N_2 temperature.	42
5.18	In the high strained regions the specimen deformed under N_2 temperature shows only at the top and bottom surface an extended amorphous band. Between them the specimen is still mostly crystalline.	42

5.19	The central region of the specimen is still crystalline with many line lines intersection the retained phase.	42
5.20	TEM bright-field and dark-field micrographs of Co_3Ti deformed with 20 turns at 4 GPa. In the dark-field image high intensity with a bright contrast is observed from the few grains in Bragg condition, whereas the dark areas corresponds to grains which are not in Bragg condition. The medium contrast is produced by the diffuse scattering amorphous areas.	44
5.21	Co_3Ti alloy deformed with 80 turns at 4 GPa by the method of HPT.	45
5.22	Radial integrated profile of the diffraction pattern shown in Fig. 5.21b. The peaks were fitted using Voigt functions. Only by raising the background to a level corresponding to the amorphous Co_3Ti intensity a good fit could be obtained.	45
5.23	Co_3Ti alloy deformed with 20 turns at 8 GPa by the method of HPT. Both, the bright-field image and the diffraction pattern show the amorphous structure of the specimen. In the diffraction pattern the rings corresponding to an amorphous short range order. Only a few very small crystals are present after deformation.	47
5.24	Heat flow (baseline corrected) from the specimen during heating from room temperature up to 590 °C.	49
5.25	Heat flow (baseline corrected) from the specimen during relaxation investigation at 250 °C up to 590 °C.	49
5.26	Temperature program of the bulk annealed specimen for comparison with the in-situ experiment.	50
5.27	Initial setup for the nanoindentation measurements	51
5.28	Imprint into the amorphous Co_3Ti surface with a load of 50 mN	52
5.29	Young's modulus and hardness evolution of initially amorphous Co_3Ti by thermal treatment. The 20 °C point corresponds to the as-deformed state. All measurements are carried out at room temperature.	53
5.30	Bright-field image of Co_3Ti made amorphous by HPT (8 GPa, 20 turns) showing the field of observation before the in-situ heating experiment. There are some larger (~ 100 nm in size) particles present which are TiO_2 particles formed during the melting or the annealing process. Annotation: Under certain circumstances one sees a sharp vertical line in the center of the image. This is an artificial contrast arising from the camera readout and not a feature of the specimen.	54
5.31	Devitrification of HPT deformed amorphous Co_3Ti during an in-situ heating TEM investigation. (a)-(d): Sequence of bright-field images taken at the indicated temperatures. The temperature step of 10 °C between each image leads to an increasing volume fraction of the crystalline phase.	55

List of Figures

5.32	Devitrification of HPT deformed amorphous Co_3Ti during an in-situ heating TEM investigation.	57
5.33	Example of dark-field images taken to analyze the particle size distribution. For the analysis always spots with high intensity are used, giving a better contrast in the images.	58
5.34	Line profile of a diffraction pattern as obtained by the radial integration of the PASAD [37] tool. In the figure also the background subtraction and the fit of the peaks by Voigt-functions optimized up to 10 nm^{-1} are illustrated.	59
5.35	Structural analysis of the in-situ specimen by comparison with experimental values obtained by X-ray diffraction.	60
5.36	Devitrified Co_3Ti after in-situ heating. Unprocessed HRTEM image showing two orientation variants of the low temperature (hcp) phase with a high number of planar defects. The atomic resolution structure of some areas reveals still the presence of the fcc stacking sequence of the high temperature phase.	62
5.37	STEM images showing clearly the formation of nm-sized TiO_2 particles which are formed by the in-situ heating and lead to a phase separation resulting in a Co rich matrix.	64
5.38	Integrated EELS signal using three different integration windows around the characteristic edges of Co, Ti and O as a function of position on the specimen. The scanned line is shown in Fig. 5.40.	65
5.39	EELS spectrum image recorded for a point on the specimen. The characteristic edges for the elements are marked with arrows. The energy scale is given in relative values. The green curve is an example fit for the background and has to be set for each edge individually. The white lines correspond to the integration window. . . .	65
5.40	HAADF image showing particles with bright and dark contrast according to their mean Z-value. The line indicates the positions over which the EELS spectra are recorded leading to the curve in Fig. 5.38	66
5.41	TEM bright-field image of the ex-situ heated specimen for comparison with the in-situ experiment. The temperature program followed by the DSC is chosen to be as similar to the in-situ temperatures as possible.	67
5.42	State of the ex-situ heated specimen using a heating rate of $20\frac{\text{K}}{\text{min}}$. After the thermal treatment for 10 min at 480°C the specimen is fully crystalline.	68
5.43	Bulk annealed specimen treated with 465°C for 10 min after heating with $20\frac{\text{K}}{\text{min}}$. The specimen shows a inhomogeneous distributed number of the plate shaped crystallites emerging from the matrix.	69

List of Figures

5.44 STEM images of a crystal of the bulk heated specimen. The crystal is near the rim of the hole and oriented near a zone axis allowing atomic resolution inaging. . . .	70
---	----

Bibliography

- [1] K.H.J. Buschow, N.M. Beekmans, “Thermal stability and electronic properties of amorphous Zr-Co and Zr-Ni alloys”, *Physical Review B* 19 (1979), 3843-3849, doi: <http://dx.doi.org/10.1103/PhysRevB.19.3843>
- [2] A. Inoue, “Bulk amorphous alloys with soft and hard magnetic properties”, *Materials Science and Engineering: A*, Volumes 226-228 (1997), 357-363, doi: [http://dx.doi.org/10.1016/S0921-5093\(97\)80049-4](http://dx.doi.org/10.1016/S0921-5093(97)80049-4)
- [3] A. Inoue, “Stabilization of metallic supercooled liquid and bulk amorphous alloys”, *Acta Materialia*, Volume 48, Issue 1 (2000), 279-306, doi: [http://dx.doi.org/10.1016/S1359-6454\(99\)00300-6](http://dx.doi.org/10.1016/S1359-6454(99)00300-6)
- [4] A. Inoue, K. Ohtera, K. Kita, T. Masumoto, “New Amorphous Mg-Ce-Ni Alloys with High Strength and Good Ductility”, *Japanese Journal of Applied Physics* 27 (1988), 2248-2251, doi: <http://dx.doi.org/10.1143/JJAP.27.L2248>
- [5] M.F. Ashby, A.L. Greer, “Metallic glasses as structural materials”, *Scripta Materialia* 54 (2006), 321-326, doi: <http://dx.doi.org/10.1016/j.scriptamat.2005.09.051>
- [6] A. Inoue, H. Tomioka, T. Masumoto, “Mechanical properties of ductile Fe-Ni-Zr and Fe-Ni-Zr (Nb or Ta) amorphous alloys containing fine crystalline particles”, *Journal of Materials Science*, Volume 18, Issue 1 (1983), 153-160, doi: <http://dx.doi.org/10.1007/BF00543821>
- [7] C.A. Schuh, T.C. Hufnagel, U. Ramamurty, “Mechanical behavior of amorphous alloys”, *Acta Materialia* 55 (2007), 4067-4109, doi:<http://dx.doi.org/10.1016/j.actamat.2007.01.052>
- [8] C. Rentenberger, T. Waitz, H.P. Karnthaler, “HRTEM analysis of nanostructured alloys processed by severe plastic deformation”, *Scripta Materialia*, Volume 51, Issue 8 (2004), 789-794, doi: <http://dx.doi.org/10.1016/j.scriptamat.2004.05.008>
- [9] H.P. Karnthaler, T. Waitz, C. Rentenberger, B. Mingler, “TEM of nanostructured metals and alloys”, *Materials Science and Engineering: A*, Volumes 387-389 (2004), 777-782, doi: <http://dx.doi.org/10.1016/j.msea.2004.01.125>
- [10] N.S. Stoloff, “Toughening mechanisms in intermetallics”, *Metallurgical Transactions A*, Volume 24, Issue 3 (1993), 561-567, doi: <http://dx.doi.org/10.1007/BF02656626>

- [11] D.B. Williams, C.B. Carter, “The Transmission Electron Microscopy”, Springer, (1996), http://dx.doi.org/10.1007/978-1-4757-2519-3_1
- [12] M. De Graef, “Introduction to Conventional Transmission Electron Microscopy”, Cambridge University Press (2003), isbn: 9780521620062
- [13] R. Gross, A. Marx, “Festkörperphysik”, Oldenburg Verlag (2012), isbn-13: 978-3486712940
- [14] <http://de.wikipedia.org/wiki/Datei:Bragg.svg>, date: 20.01.2014, This figure was released into the public domain by the author. Feel free to use and share it.
- [15] <http://de.wikipedia.org/wiki/Datei:Laue-Bedingung.png>, date: 20.01.2014, This figure was released into the public domain by the author. Feel free to use and share it.
- [16] https://en.wikipedia.org/w/index.php?title=Structure_factor&oldid=578475395, date: 20.01.2014
- [17] J.L. Murray, “Co-Ti (Cobalt-Titanium), Binary Alloy Phase Diagrams”, ASM International, 2nd edition, Ed. T.B. Massalski 2 (1990), 1250-1252
- [18] G. Audi, A.H. Wapstra, C. Thibault, “The Ame2003 atomic mass evaluation (II)”, Nuclear Physics A729 (2003), 337-676, <http://www.nndc.bnl.gov/masses/mass.mas03>
- [19] K.H.J. Buschow, P.G. van Engen, R. Jongebreur, “Magneto-optical properties of metallic ferromagnetic materials”, Journal of Magnetism and Magnetic Materials, Volume 38, Issue 1, (1983), 1-22, doi: [http://dx.doi.org/10.1016/0304-8853\(83\)90097-5](http://dx.doi.org/10.1016/0304-8853(83)90097-5)
- [20] Ruslan Z. Valiev, Yuri Estrin, Zenji Horita, Terence G. Langdon, Michael J. Zechetbauer, Yuntian T. Zhu, “Producing bulk ultrafine-grained materials by severe plastic deformation”, JOM, Volume 58, Issue 4 (2006), 33-39, doi: <http://dx.doi.org/10.1007/s11837-006-0213-7>
- [21] R.Z. Valiev, R.K. Islamgaliev, I.V. Alexandrov, “Bulk nanostructured materials from severe plastic deformation”, Progress in Materials Science 45 (2000), 103-189
- [22] Alexander P. Zhilyaev, Terence G. Langdon, “Using high-pressure torsion for metal processing: Fundamentals and applications”, Progress in Materials Science 53 (2008), 893-979, doi: <http://dx.doi.org/10.1016/j.pmatsci.2008.03.002>
- [23] M.V. Degtyarev, T.I. Chashchukhina, L.M. Voronova, A.M. Patselov, V.P. Pilyugin, “Influence of the relaxation processes on the structure formation in pure metals and alloys under high-pressure torsion”, Acta Materialia 55 (2007), 6039-6050, doi: <http://dx.doi.org/10.1016/j.actamat.2007.04.017>
- [24] D. Geist, C. Rentenberger, H.P. Karnthaler, “Extreme structural inhomogeneities in high-pressure torsion samples along the axial direction”, Acta Materialia 59 (2011), 4578-4586, doi: <http://dx.doi.org/10.1016/j.actamat.2011.04.003>

- [25] P.J. Goodhew, “Specimen Preparation in Materials Science”, North-Holland/American Elsevier (1972)
- [26] http://en.wikipedia.org/wiki/File:Scheme_TEM_en.svg, date: 20.01.2014, License: This file is licensed under the Creative Commons Attribution-Share Alike 3.0 Unported license.
- [27] https://en.wikipedia.org/wiki/File:Schema_MEB_%28en%29.svg, date: 20.01.2014, License: This file is licensed under the Creative Commons Attribution-Share Alike 1.0 Generic license.
- [28] https://en.wikipedia.org/wiki/Brinell_scale, date: 17.12.2013
- [29] R.L. Smith & G.E. Sandland, “An Accurate Method of Determining the Hardness of Metals, with Particular Reference to Those of a High Degree of Hardness”, Proceedings of the Institution of Mechanical Engineers, Volume I (1922), 623-641, doi: http://dx.doi.org/10.1243/PIME_PROC_1922_102_033_02
- [30] E.S. Berkovich, “Three-Faceted Diamond Pyramid for Studying Microhardness by Indentation”, Zavodskaya Laboratoria, Volume 13 (1950), 345-347
- [31] W.C. Oliver, G.M. Pharr, “Improved technique for determining hardness and elastic modulus using load and displacement sensing indentation experiments”, Journal of materials research, Volume 7, Issue 6 (1992), 1564-1583, doi: <http://dx.doi.org/10.1557/JMR.1992.1564>
- [32] W.C. Oliver, G.M. Pharr, “Measurement of hardness and elastic modulus by instrumented indentation: Advances in understanding and refinements to methodology”, Journal of Materials Research 19 (2004), 3-20, doi: <http://dx.doi.org/10.1557/jmr.2004.19.1.3>
- [33] G. Höhne, W. Hemminger, H.-J. Flammersheim, “Differential Scanning Calorimetry”, Springer (1996)
- [34] National Institute for Materials Science (NIMS) AtomWork <http://crystdb.nims.go.jp/> (Accessed: 05.05.2014)
- [35] M. Sherif El-Eskandarany, K. Aoki, K. Sumiyama, K. Suzuki, “Cyclic phase transformations of mechanically alloyed Co₇₅Ti₂₅ powders”, Acta Materialia 50 (2002), 1113, doi: [http://dx.doi.org/10.1016/S1359-6454\(01\)00412-8](http://dx.doi.org/10.1016/S1359-6454(01)00412-8)
- [36] H. Yasuda, T. Takasugi, M. Koiwa, “Elastic constants of Co₃Ti and CoTi intermetallic compounds”, Materials Transactions, JIM, Volume 32, No.1 (1991), 48-51
- [37] C. Gammer, C. Mangler, C. Rentenberger, H.P. Karnthaler, “Quantitative local profile analysis of nanomaterials by electron diffraction”, Scripta Materialia 63 (2010), 312-315, doi: <http://dx.doi.org/10.1016/j.scriptamat.2010.04.019>

- [38] J. Sort, J. Nogués, S. Suriñach, J.S. Muñoz, M.D. Baró, “Correlation between stacking fault formation, allotropic phase transformations and magnetic properties of ball-milled cobalt”, *Materials Science and Engineering A*, Volumes 375-377 (2004), 869-873, doi: <http://dx.doi.org/10.1016/j.msea.2003.10.186>
- [39] M. Singh, M. Barkei, G. Inden, S. Bhan, “High-temperature X-ray diffraction study on Co₇₅Sn₂₅ alloy”, *Physica Status Solidi A* Volume 87, Issue 1 (1985), 165-168, doi: <http://dx.doi.org/10.1002/pssa.2210870115>

Acknowledgments

I especially thank Univ.-Prof. Dr. Christian Rentenberger for the support and the supervision of the thesis. Without his efforts and guidance it wouldn't have been possible to realize this work. On this occasion I also would like to thank Univ.-Prof. i.R. Dr. Hans-Peter Karnthaler for his motivation and the helpful discussions.

Another thank you goes to Dr. Christoph Gammer, Dr. David Geist and Ing. Andreas Berger for their help and tips with the technical equipment, the sample preparation and the fruitful discussions. Thank you also to Dr. Clemens Mangler for his help with the Nion UltraSTEM 100. Furthermore I would also like to thank Univ.-Prof. Dr. Ferdinand Hofer for the possibility and Dr. Christian Gspan for the help in using the Titan microscope at the FELMI-ZFE in Graz, Austria.

I would like to thank also Ass.-Prof. Sassik Herbert and Ing. Vladimira Piwetz for their help with the melting of the alloy at the TU Wien, Austria.

Last but not least, I would also thank my friends and family for their support and help with all the little problems in the last years.

EUROPEAN CURRICULUM VITAE

PERSONAL INFORMATION

Name	Christian Ebner
E-mail	christian.ebner@univie.ac.at christian.ebner@outlook.com
Nationality	Italian

EDUCATION AND TRAINING

March 2012 - until now	Studies for the “Master of Science” degree in physics at the University of Vienna, thesis: “Devitrification of Co_3Ti Studied by Electron Microscopy Methods”
October 2008 - March 2012	“Bachelor of Science” degree in physics at the University of Vienna, thesis: “Contrast Formation and Dislocation Imaging in the Transmission Electron Microscope”
September 2002 - June 2008	High school graduation at “Gewerbeoberschule Max Valier” in Bolzano (IT) with specialization in industrial computer science

WORK EXPERIENCE

March 2012 - until now	Internship for the Master’s degree at the electron microscopy group at the University of Vienna under the supervision of Ao. Univ.-Prof. Mag. Dr. Christian Rentenberger Main activities: Sample alloying and preparation, specimen analysis using the (scanning) transmission electron microscope, scanning electron microscope, differential scanning calorimetry and nanoindentation
February 2011 - April 2011	Internship for the Bachelor’s degree at the electron microscopy group at the University of Vienna under the supervision of Ao. Univ.-Prof. Mag. Dr. Christian Rentenberger Main activities: Sample preparation, specimen analysis using the transmission electron microscope

**CONFERENCE
ATTENDANCES**

May 2014	4 th ASEM Workshop in Vienna, Austria oral presentation: “Fluctuation TEM of an amorphous-crystalline composite material”
April 2014	European Workshop on Spatially-Resolved Electron Spectroscopy in Graz, Austria Poster presentation: “EELS of Nanocrystals Embedded in Co ₃ Ti Made Amorphous by Severe Plastic Deformation”
August 2013	Microscopy Conference MC 2013 in Regensburg, Germany Poster presentation: “Devitrification of Co ₃ Ti Studied by In-situ Heating in the TEM”
June 2013	EMAT Workshop on Transmission Electron Microscopy - Summer Workshop 2013 in Antwerp, Belgium completion of the “High Resolution Module”
April 2013	3 rd ASEM Workshop in Vienna, Austria Oral presentation: “Devitrification of Co ₃ Ti Studied by In-situ Heating in the TEM”

**PERSONAL SKILLS
AND COMPETENCE**

Mother tongue	German
Other languages	Italian - Good spoken and written English - Good spoken and written
Social skills	Good sharing capabilities and good relational skills

COMPUTER SKILLS

Programming languages	C/C++, Java, basic knowledge of SQL
Special interest	Linux and open source software, electronics and microcontroller programming (ATMEL)